Durham E-Theses

Secondary-Side Control in Dynamic Wireless Power Transfer Systems for Double-Sided Inductor-Capacitor-Capacitor and Series-Series Compensation Topologies

ALVAREZ-PADILLA, JUAN,RODOLFO

How to cite:

Use policy

Abstract

Secondary-Side Control in Dynamic Wireless Power Transfer Systems for Double-Sided Inductor-Capacitor-Capacitor and Series-Series Compensation Topologies

by

Juan Rodolfo Alvarez Padilla, Master by Research

Durham University, 2017

Supervised by: Dr Hongjian Sun

Department: Engineering

Electric Vehicles (EVs) are fast becoming a great alternative as future mode of transportation, due to their promise of low emissions. Nevertheless, EVs suffer from battery related problems such as large size, heavy weight, high price, long charging times and a short driving range. Dynamic wireless power transfer systems (DWPTSs) address the battery issue by providing power to the vehicle while in motion, and eliminate the need of plugging. However, unavoidable load and coupling coefficient variations cause degradation of power delivery and efficiency. Hence, a controller must be added to the dynamic charger for power conditioning and efficiency enhancement. This project is focused on the control stage of the DWPTS adopting a post-regulation scheme as control strategy. It proposes the integration of a secondary-side-only control under double-sided inductor-capacitor-capacitor (LCC) and series-series compensation topologies. A synchronous buck converter is used to step down the voltage to the maximum power transfer efficiency (MPTE) conditions and control the direct current (DC) link by adjusting the duty cycle of the control pulse. Averaged alternating current (AC) modelling is applied for designing the controller to smooth and speed the response of both systems. An estimation equation for coupling coefficient and a controller for the double-sided LCC compensation topology are introduced. A comparison study between these two topologies comprised of their characteristics and response to the controller is carried out.

SECONDARY-SIDE CONTROL IN DYNAMIC WIRELESS POWER TRANSFER SYSTEMS FOR DOUBLE-SIDED INDUCTOR-CAPACITOR-CAPACITOR AND SERIES-SERIES COMPENSATION TOPOLOGIES

by

Juan Rodolfo Alvarez Padilla

A thesis submitted to the Engineering Department

in conformity with the requirements for

the degree of Master by Research

Durham University

School of Engineering
and Computing Sciences

Durham, United Kingdom

(September, 2017)

Contents

Table of Figures

Acronyms

CO_2	Carbon Dioxide
UK	United Kingdom
VCA	Vehicle Certification Agency
EV	Electric Vehicles
IEA	International Energy Agency
DWPTS	Dynamic Wireless Power Transfer System
BEV	Battery Electric Vehicle
ICE	Internal Combustion Engine
WPTS	Wireless Power Transfer System
EMF	Electromagnetic Field
CT	Compensation Topology
PATH	Partners for Advance Transit and Highways
KAIST	Korea Advanced Institute of Science and Technology
OLEV	Online Electric Vehicle
IPT	Inductive Power Transfer
CMR	Coupled Magnetic Resonance
CPT	Capacitive Power Transfer
WCPT	Wireless Energy Harvesting System
MPT	Microwave Power Transfer
LPT	Laser Power Transfer
SCEV	Stationary Charging Electric Vehicle
RPEV	Roadway Powered Electric Vehicle
PTE	Power Transferred Efficiency
ORNL	Oak Ridge National Laboratory
AC	Alternating Current
DC	Direct Current
FEA	Finite Element Analysis
ICNIRP	International Commission on Non-Ionizing Radiation Protection
SS	Series-Series
LCC	Inductor-Capacitor-Capacitor

RMS   Root Mean Square

MOSFET   Metal-Oxide-Semiconductor Field-Effect-Transistor

IGBT   Insulated-Gate Bipolar Transistor

MPTE   Maximum Power Transfer Efficiency

PID   Proportional-Integral-Differential

MATLAB   Matrix Lab

RMSD   Root-mean-square deviation

Nomenclature

r	Distance from the radiative source
H	Magnetic field strength
J	Electric current density
B	External magnetic field
E	Electric field
∇	Gradient
j	Imaginary number
ω	Angular frequency
V	Volts
A	Amperes
v_1	Alternating voltage of AC source / input voltage
V_1	Input voltage magnitude
$\boldsymbol{V}_1$	Input voltage phasor
v_2	Output voltage
V_2	Output voltage magnitude
$\boldsymbol{V}_2$	Output voltage phasor
v_{2_ss}	Series-series output voltage
$V_{2_{ss}}$	Series-series output voltage magnitude
$\boldsymbol{V}_{2_{ss}}$	Series-series output voltage phasor
v_{2_lcc}	Double-sided LCC output voltage
$V_{2_{lcc}}$	Double-sided LCC output voltage magnitude
$\boldsymbol{V}_{2_{lcc}}$	Double-sided LCC output voltage phasor
$V_{2\_ss\eta MAX\_RMS}$	Root mean square series-series output voltage for maximum efficiency
$V_{2\_lcc\eta MAX\_RMS}$	Root mean square double-sided LCC output voltage for maximum efficiency
v_{DC}	DC link voltage / Average DC output voltage of the rectifier
v_{DC1}	DC link voltage in mode 1 of the buck converter
v_{DC2}	DC link voltage in mode 2 of the buck converter
V_{DC}	Rectifier DC output voltage
V_{DC_ss}	Series-series DC link voltage magnitude/ DC output voltage magnitude of the rectifier
V_{DC_lcc}	Double-sided LCC DC link voltage magnitude/ DC output voltage magnitude of the rectifier
$\hat{v}_{DC}$	Average DC link voltage
$\hat{v}_{DC\_ss}$	Series-Series average DC output voltage of the rectifier
$\hat{v}_{DC\_lcc}$	Double-sided LCC average DC output voltage of the rectifier
$V_{DC\_ss}^*$	Series-series DC link voltage reference
$V_{DC\_lcc}^*$	Double-sided LCC DC link voltage reference
V_{out}	Output voltage magnitude of the buck converter
i_1	Alternating current of AC source / Transmitter current
I_1	Transmitter current magnitude
$\boldsymbol{I}_1$	Transmitter current phasor
i_2	Receiver current
I_2	Receiver current magnitude
$\boldsymbol{I}_2$	Receiver current phasor
i_t	Double-sided LCC transmitter current
I_t	Double-sided LCC transmitter current magnitude

I_t	Double-sided LCC transmitter current phasor
i_r	Double-sided LCC receiver current
I_r	Double-sided LCC receiver current magnitude
I_r	Double-sided LCC receiver current phasor
i_{1_ss}	Series-series transmitter current
I_{1_ss}	Series-series transmitter current phasor
i_{2_ss}	Series-series receiver current
I_{2_lcc}	Series-series receiver current phasor
i_{1_lcc}	Double-sided LCC input current
I_{2_lcc}	Double-sided LCC input current phasor
i_{2_lcc}	Double-sided LCC output current
I_{2_lcc}	Double-sided LCC output current phasor
i_L	Load current
I_L	Load current magnitude
I_{L_ss}	Series-series quiescent point load current
I_{L_lcc}	Double-sided LCC quiescent point load current
i_{L1}	Load current in mode 1 of the buck converter
i_{L2}	Load current in mode 2 of the buck converter
$\hat{\imath}_L$	Average load current
$\hat{\imath}_{L\_ss}$	Series-series average load current
$\hat{\imath}_{L\_lcc}$	Double-sided LCC average load current
i_{DC}	Average DC output current of the rectifier
I_{DC}	Rectifier DC output current
i_{DC_ss}	Series-Series DC output current of the rectifier
i_{DC_lcc}	Double-sided LCC DC output current of the rectifier
$\hat{\imath}_{DC}$	Average DC output current of the rectifier
$\hat{\imath}_{DC\_ss}$	Series-Series average DC output current of the rectifier
$\hat{\imath}_{DC\_lcc}$	Double-sided LCC average DC output current of the rectifier
v_i	Inverter output voltage/Compensation network input voltage
V_s	Inverter voltage source
V_{1_RMS}	First harmonic root mean square voltage / root mean square input voltage
V_{2_RMS}	Root mean square output voltage
I_{1_RMS}	First harmonic root mean square current / root mean square input current
I_{2_RMS}	Root mean square output current
$v_{2\_ss\_RMS}$	Root mean square series-series output voltage
$v_{2\_lcc\_RMS}$	Root mean square double-sided LCC output voltage
$I_{2\_ss\_RMS}$	Root mean square output current of the series-series system
$I_{2\_lcc\_RMS}$	Root mean square output current of the double-sided LCC system
T_0	Inverter period
n	Inverter harmonic number
$Q_{1,2,3,4}$	The nth transistor of the full bridge inverter
M	Mutual inductance
k	Coupling coefficient
k_{est_lcc}	Series-series estimated coupling coefficient
k_{est_lcc}	Double-sided LCC estimated coupling coefficient
L_1	Transmitter inductance
L_2	Receiver inductance
R_1	Transmitter equivalent resistance

R_2	Receiver equivalent resistance
C_1	Series- series transmitter compensation capacitance
C_2	Series- series receiver compensation capacitance
L_{s1}	Double-sided LCC series inductance of the transmitter
C_{p1}	Double-sided LCC parallel capacitance of the transmitter
C_{s1}	Double-sided LCC series capacitance of the transmitter
L_{s2}	Double-sided LCC series inductance of the receiver
C_{p2}	Double-sided LCC parallel capacitance of the receiver
C_{s2}	Double-sided LCC series capacitance of the receiver
R_{eq}	Load equivalent resistance
R_{2_eq}	Rectifier equivalent resistance
R_{L_eq}	DC-DC converter equivalent resistance
$R_{eq\_ss\eta MAX}$	Series-series equivalent resistance for maximum efficiency
$R_{eq\_lcc\eta MAX}$	Double-sided LCC equivalent resistance for maximum efficiency
η	Efficiency
ω_0	Operating angular frequency
f_s	Switching frequency
f_0	Operating frequency
$A_{V_{ss}}$	Series-series voltage gain
$A_{I_{ss}}$	Series-series current gain
η_{ss}	Series-series efficiency
$A_{P_{ss}}$	Series-series power gain
$P_{1_{ss}}$	Series-series input power
$P_{2_{ss}}$	Series-series output power
$A_{V_{lcc}}$	Double-sided LCC voltage gain
$A_{I_{lcc}}$	Double-sided LCC current gain
η_{lcc}	Double-sided LCC efficiency
$A_{P_{lcc}}$	Double-sided LCC power gain
$P_{1_{lcc}}$	Double-sided LCC power input
$P_{2_{lcc}}$	Double-sided LCC power output
T_t	Time that the EV spends on each transmitter
l_t	Transmitter length
S_{EV}	Electric vehicle speed
$k_{rt\,i}$	Coupling coefficient of an individual transmitter of a set and the receiver
k_{rt}	Total coupling coefficient of a set of transmitters and the receiver
N	Number of transmitters
T_p	Time of the simulation pulse
$S_{1,2}$	The nth transistor of the buck converter
f_c	Switching frequency of the buck converter
C_0	Capacitance of the buck converter
L_0	Inductance of the buck converter
R_0	Inductance equivalent resistance of the buck converter
V_b	Battery voltage
r_b	Battery equivalent series resistance
R_{out}	Total output resistance
D	Constant duty cycle
d	Duty cycle function

T_a	Average period
f, g	Arbitrary functions
t, τ	Arbitrary times
$\hat{d}$	Average duty cycle function
K	Gain matrix
$\hat{x}$	Average state vector
$\hat{y}$	Average output
$\hat{u}$	Average input vector
$\hat{A}$	Average system matrix
$\hat{B}$	Average input matrix
$\hat{C}$	Average output matrix
K_{ff}	Feed-forward gain
D_{ss}	Series-series quiescent point duty cycle
$\hat{d}_{ss}$	Series-series duty cycle function
K_{ss}	Series-series gain matrix
$\hat{x}_{ss}$	Series-series state vector
$\hat{y}_{ss}$	Series-series output
$\hat{u}_{ss}$	Series-series input vector
$\hat{A}_{ss}$	Series-series system matrix
$\hat{B}_{ss}$	Series-series input matrix
$\hat{C}_{ss}$	Series-series output matrix
D_{lcc}	Double-sided LCC quiescent point duty cycle
$\hat{d}_{lcc}$	Double-sided LCC duty cycle function
K_{lcc}	Double-sided LCC gain matrix
$\hat{x}_{lcc}$	Double-sided LCC state vector
$\hat{y}_{lcc}$	Double-sided LCC output
$\hat{u}_{lcc}$	Double-sided LCC input vector
$\hat{A}_{lcc}$	Double-sided LCC system matrix
$\hat{B}_{lcc}$	Double-sided LCC input matrix
$\hat{C}_{lcc}$	Double-sided LCC output matrix
I	Identity matrix
$G(s)$	Transfer function
$G_c(s)$	Controller transfer function
$G_{Buck_{ss}}$	Series-series buck converter transfer function
$b_{1\_ss}, b_{0\_ss}, a_{1\_ss}, a_{0\_ss}$	Coefficients of the transfer function of the series-series system
$G_{Buck_{lcc}}$	Double-sided LCC buck converter transfer function
$b_{1\_lcc}, b_{0\_lcc}, a_{1\_lcc}, a_{0\_lcc}$	Coefficients of the transfer function of the double-sided LCC system
V_{ci}	Input voltage of the buck converter
V_{co}	Output voltage of the buck converter
ΔI_{co}	Output current ripple
ΔV_{DC}	DC link voltage ripple
$\mathcal{L}$	Laplace transform
$c(t)$	Time response of the system
$c_{ss}(t)$	Time response of the series-series system
$c_{lcc}(t)$	Time response of the double-sided LCC system
T_s	Settling time

$OS\%$	Overshoot percentage
$e(\infty)$	Steady-state error
ζ	Damping ratio
ω_n	Natural frequency
$T_{s_{ss}}$	Settling time of the series-series system
$T_{s_{lcc}}$	Settling time of the double-sided LCC system
$OS\%_{ss}$	Overshoot percentage of the series-series system
$OS\%_{lcc}$	Overshoot percentage of the double-sided LCC system
$e_{ss}(\infty)$	Steady-state error of the series-series system
$e_{lcc}(\infty)$	Steady-state error
K_P	Proportional gain
K_I	Integral gain
K_D	Differential gain
τ_D	Differential filter constant
K_{P_ss}	Proportional gain of the series-series system
K_{I_ss}	Integral gain of the series-series system
K_{D_ss}	Differential gain of the series-series system
τ_{D_ss}	Differential filter constant of the series-series system
K_{P_lcc}	Proportional gain of the double-sided LCC system
K_{I_lcc}	Integral gain of the double-sided LCC system
K_{D_lcc}	Differential gain of the double-sided LCC system
τ_{D_lcc}	Differential filter constant of the double-sided LCC system
$RMSD$	Root Mean Square Deviation

Acknowledgments

I would like to express my deepest gratitude to my supervisor Dr Hongjian Sun, whose advice and encouragement helped to guide my research. I am very grateful to my office colleagues Ahmad Asrul and Javier Renedo, whose tolerance and support were invaluable to finish my project. I want to thank my parents, who have inspired me through the years to dream big, and that once it is done, to work strong to make it happen. I am especially grateful to my brothers Francisco Jr and Cristian. I want to thank them not only for their technical support and help every time I needed, but also for being precious friends. I want to thank my dear girlfriend Rossio González as well, who has been patient, understanding and supportive with me at all times. I am also thankful to my former Control System professor, Dr Marco Pérez, who during my undergraduate studies motivated me to study abroad and become a researcher. Thanks to the Universidad de Guadalajara for giving me my first job in Academia, where I realised my passion for teaching. Similarly, I am grateful to Durham University to give me the great opportunity of studying in the UK for one year. I would also like to thank the Mexican Council for Science and Technology, CONACyT, for providing financial support during my studies.

Finally, I would like to thank Ustinov College for being my second home during this time. I learnt many things and met many people from all over the world. I found real friendship. I had a great environment for academic development. Simply, I made the best choice by living at Ustinov. For these reasons, I will always say that: I am a believer! I am Ustinovian!

I have been lucky to have many people looking after me during my life.

To my beloved parents:

Francisco and Sandra

&

To my dear grandmother and aunt:

Maria Luisa and Melly

&

To my treasured brothers:

Francisco Jr and Cristian

&

To my dear girlfriend:

Rossio

Chapter 1

1. Introduction

1.1. Overview of EV

The world is facing serious environmental issues as a result of high CO_2 emissions. In 2013, the UK Vehicle Certification Agency (VCA) reported that domestic and international transport accounted for 26% of UK greenhouse gas emissions [1]. In 2015, the Mexican Secretary of Environment informed that automobiles produced 26.2% of CO_2 emissions in Mexico [2]. For this reason, electric vehicles (EVs) are fast becoming a great alternative as future mode of transportation, due to their promise of low emissions. The International Energy Agency (IEA) reports that the current world stock of hybrid and pure electric cars is more than one million. This represents 0.1% of the vehicle fleet. However, in countries like the Netherlands and Norway EVs account for 11% and 29% of the total number of cars. Moreover, the IEA estimates that 40% of the worldwide car stock, approximately nine hundred million cars, will be electric by 2050 [3]. Although this is a promising outlook, EVs today have several limitations that have hampered their spread.

EVs suffer from battery related problems such as large size, heavy weight, high price, long charging times and a short driving range [4]. For example, suppose a person wants to travel from Durham to London, a 438-km trip, by car. The current EV driving range is approximately 124 km (average). This would require recharging the battery at least four times, before and during the journey. Furthermore, the driver will wait approximately 30 minutes, in the case of a fast charger, or seven hours with a conventional charger per each charge.

In order to solve the drawbacks presented above, several research groups have recently carried out work on the development of wireless technologies to power vehicles in motion, dynamic wireless power transfer systems (DWPTSs), particularly for vehicles which perform in a fixed route. The solution proposed addresses the battery issue by providing power to the vehicle while in motion, and eliminates the need of plugging. This removes the need for charging downtime. Moreover, it extends cruising range, allows for downsizing the battery, and decreases both the weight and cost of an EV [5]. If one considered a DWPTS with more power capacity than the power consumption of the EV, then the EV would have unlimited range. In addition, the battery's life extension is achieved by the constant charging process, reducing the depth of discharge [6].

An additional reason for the adoption of wireless charging is user comfort, by eliminating the use of cables. Furthermore, it reduces safety concerns around the handling of electrical connectors. Thus, because of DWPTSs, battery only electric vehicles (BEVs) now represent good competition to internal combustion engine (ICE) vehicles.

Despite the innovative ideas above, the feasible adoption of EVs is limited by cost. BEVs are cleaner, more efficient but much more expensive. High initial investment for either EV or infrastructure has hampered the deployment of roadway powered electric vehicles (RPEVs). In addition, there are several safety concerns around high power radiation.

Regarding existing research, current work in wireless power transfer systems is primarily concerned in three subject areas [7]:

     a) Coil design and electromagnetic field (EMF) cancellation
     b) Compensation topologies (CTs)
     c) Power electronic converters and control

1.2. Wireless Power Transfer Systems

1.2.1. History

Transferring power wirelessly is not a novel idea. Wireless power transfer systems can be tracked back to James Maxell, Heinrich Hertz, Guglielmo Marconi and Nikola Tesla. Hertz and Marconi validated the concept of energy transportation through vacuum via electromagnetic waves, without the need of conductors, as introduced by Maxwell in the late nineteenth century [8]. Tesla's 1891 patent, "Systems of Electric Lighting", acknowledged the transference of energy through the free space [9]. In 1901, Tesla started to build the Wardenclyffe Tower. It was a prototype to prove his principle of wireless transmission of energy, transporting electricity via radio waves as a convenient alternative to wires. Tesla attempted to create a "World Wireless System", which would be able to give free energy access to everyone [10]. However, this project failed due to financial troubles. Prior to Tesla's tower, Hutin and Le-blanc had coined the term roadway powered electric vehicles [4] in their first patent. This referenced the use of a wireless track to power a railway in motion (Figure 1). It included an AC generator of 3 kHz [11]. Figure 1 (b) shows the cross-sectional view of the Huntin's RPEV, where the rail and wireless transmitter of the vehicle are illustrated in more detail. This was followed by a period of absence of development, which has been attributed to a lack of technology [7].
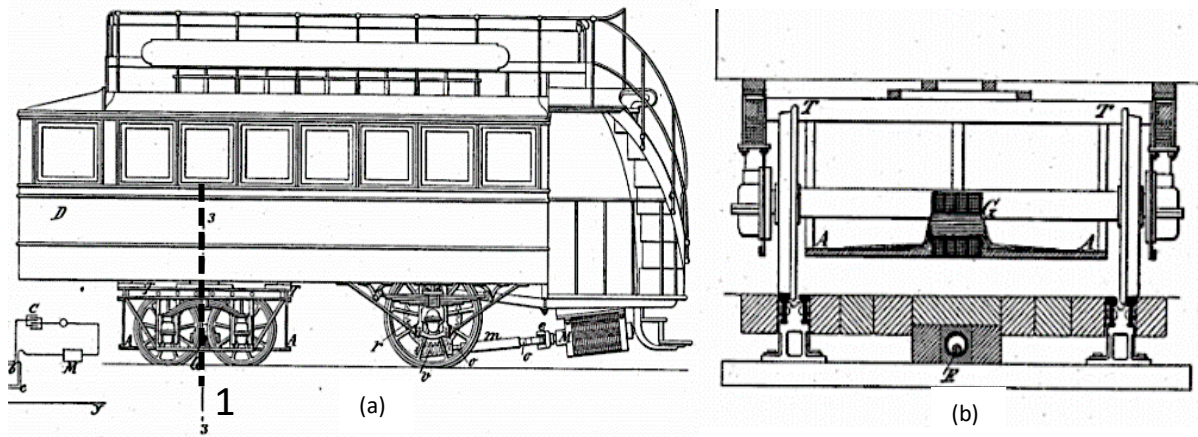
Figure 1. Hutin & Leblanc first patent of a REPV [11]: (a) side view of the vehicle and rail (b) cross-sectional view at line 1 of (a)

After the innovation in power electronics, there was a "boom" in WPTS that marked the beginning of a new era on this matter. The first designs were based on induction systems employed in factory automation to power restricted movement vehicles [12].

By the end of the 1970s, the University of California Berkeley ran the Partners for Advance Transit and Highways (PATH) program, which included the implementation of a roadway powered 35-passenger bus. It consisted of a 213-long track divided in two sections able to provide 60 kW (120 A, 60 Hz) across a variable air gap of 50-200 mm. However, it suffered from poor efficiency (60%) and excessive acoustic noise issues [12-14].

Researchers at Auckland University have been working on WPTS since the turn of the current century. They have primarily focussed on Coil Design [15-22], control methods [23-25] and DWPTSs [26]. In 2007, the Massachusetts Institute of Technology (MIT) presented a publication that captured the interest of the research community [13]. In this work, a light bulb was illuminated over a distance of 2.5 m, at 60 W power with 40% efficiency. This experiment exhibited that distance was no longer a barrier for power delivery. The WiT3300 kit, from WiTricity Corporation (an MIT spin-off), was capable of transferring 3.3 kW through an air gap of 180 mm at 90% efficiency.

In 2009, scientists from the Korea Advanced Institute of Science and Technology (KAIST) demonstrated a series of buses, a golf cart and a tram that operate using dynamic wireless charging [4, 14, 27]. This lead to the commercialisation of wireless EV chargers – up to 100 kW – aptly named online electric vehicle (OLEV) [4, 13, 28]. Six generations of OLEV have

3

since been developed with efficiencies from 70% to 83%. The main achievement of OLEV systems is efficient magnetic field shaping through coil design [27].

The society of automotive engineers (SAE) established a new standard in 2010, in reaction to the increase in wireless systems at that time and the lack of interoperability among prototypes [28]. SAE TIR J2954 is a guideline that "defines acceptable criteria for interoperability, electromagnetic compatibility, minimum performance, safety and testing for wireless charging of light duty electric and plug-in electric vehicles" [29]. In 2015, Utah State University built an advanced test facility for dynamic wireless charging [7].

1.2.2. Classification

WPTSs (seen as electromagnetic waves systems) can be classified in two main categories, near and far field. Moreover, these categories are subdivided into several subcategories:

- Near field WPTS
    1. Inductive Power Transfer (IPT)
    2. Coupled Magnetic Resonance (CMR)
    3. Capacitive Power Transfer (CPT)

- Far field WPTS
    4. Wireless Energy Harvesting System (WCPT)
    5. Microwave Power Transfer (MPT)
    6. Laser Power Transfer (LPT)

Near field refers to a distance, from the radiative source, within one wavelength. An advantage for high power applications in this region relies on the existence of the electric and magnetic field created from only one source, without the need of other sources. In this region, electromagnetic field decays very fast at a ratio of $\sim 1/r^3$ [8], where r is the distance from the radiative source. Thus, the range for transmission is short. Inductive power transfer exploits magnetic fields to accomplish power transference. Coupled magnetic resonance is a particular case of inductive systems with several resonant repeaters for distance extension and a higher quality factor [4]. However, CMRSs are not adopted for DWPTS because of the small areas, on the roadway and at the bottom of cars, available for placing bulky transmitters and receivers. Capacitive power transfer employs electric fields to transfer power [28]. CPTS has far less field leakage than IPT. Nevertheless, it is constrained to small air gaps. That is to say that it is not a

convenient method for WPTS for EV applications because of its large bottom clearance. A typical air gap for EVs ranges from 100 mm to 300 mm [12].

The far field constitutes the region inside two wavelengths. In this region field strength drops at a ratio of ~$1/r^2$ [8]. This is more suitable for transmission of signals (information) rather than power due to its low directivity. Some methods can be used to enhance this parameter, particularly the use of high frequency signals in the microwave range, MPT, or by designing phase-coherent sources that amplify electromagnetic waves for precisely transmitting power over long distances, LPT [30]. The region between these zones is known as the transition zone, wherein the combined effects of both near and far field can occur.

The operational state of a wireless system can be classified as either static or dynamic charging. A static or stationary charged electric vehicle (SCEV) includes the charge of parked vehicles. Meanwhile, dynamic charging considers moving vehicles along roadways that powers them wirelessly [7]. A roadway powered electric vehicle (RPEV) consists of an inductive power transfer system (IPTS) that considers a vehicle in motion.

1.2.3. Fundamentals

A RPEV adopting a DWPTS is the subject of study in this research and therefore it is further described. This kind of technology draws power through resonant coupling between the electromagnetic field of an array of transmitter coils embedded in pathways and a receiver coil under a vehicle. Basically, electromagnetic waves make possible the transference of energy wirelessly. Hence, this phenomenon can be described by Maxwell's equations. A time varying-magnetic flux is generated from an AC current power supply pad in accordance with Ampere's law (1.1). H represents the magnetic field strength and J is the electric current density; then, voltage is induced from the receiver coil, which interacts with the transmitter pad, in terms of the Faraday's law (1.2). E is the electric field and B comes for the external magnetic field; subsequently, power is wirelessly delivered due to the magnetic coupling established between the transmitter and receiver. The quality of this interaction determines the resulting power transfer efficiency (PTE).

$$\nabla \times H = J \text{ (Ampere's law)} \tag{1.1}$$

$$\nabla \times E = -j\omega B \text{ (Faraday's law)} \tag{1.2}$$

In IPTSs, the electromagnetic field is the medium of synergy between transmitter and receiver. Inductive systems include traditional transformers where power delivery, from primary to secondary, is achieved across a narrow air gap at low frequencies (50 Hz, 60 Hz). This is called a strongly coupled system.

Alternatively, when the air gap is large (around tens of centimetres or greater) and the frequency is increased to get higher efficiency, this is known as a loosely coupled system. In comparison with wired chargers, a wireless charger replaces the transformer in a loosely coupled system.
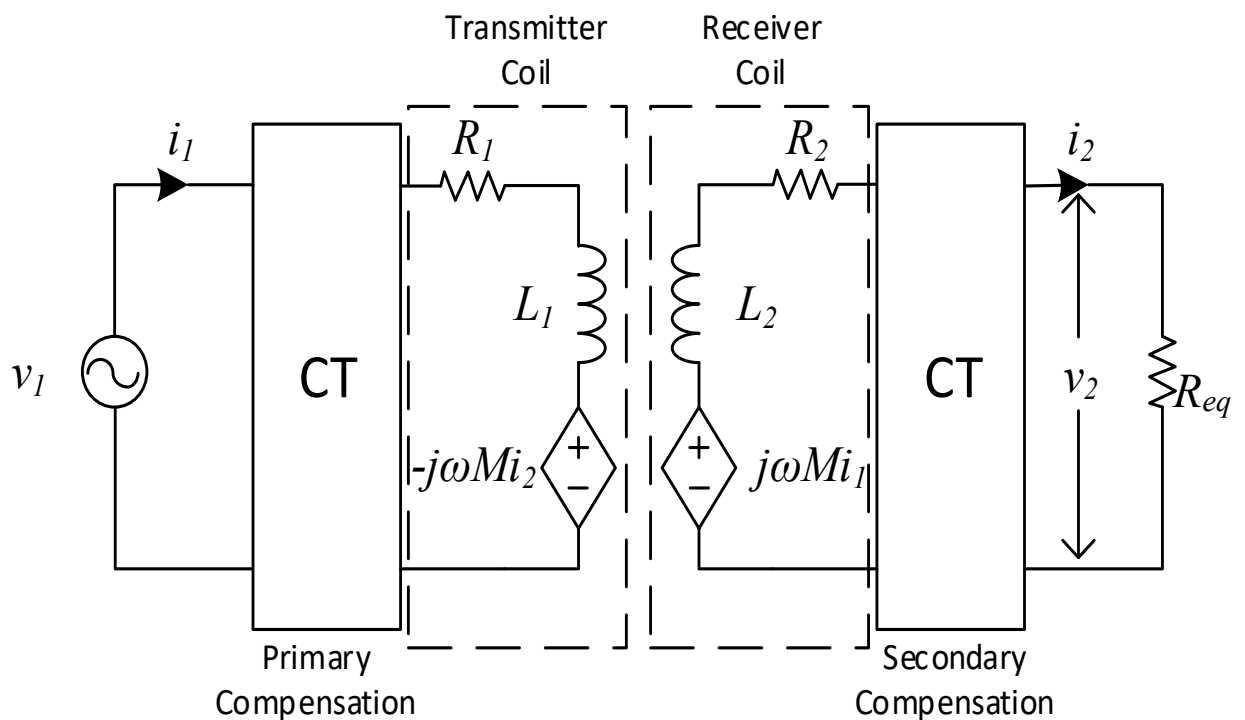
Figure 2. Circuit theory representation

The WPTS principle can be represented by circuit theory (Figure 2). Subscripts 1 and 2 refer to the primary and secondary, transmitter and receiver, components' values. Looking at the power supply side, v_1 and i_1 are the alternating voltage and current of the AC source. A single-phase full bridge inverter (detailed in the next chapter) will be used to produce alternating current at a certain switching frequency (f_s). The coils are characterised by their AC resistance and inductance, R and L. Moreover, due to the transmitter-receiver magnetic interaction, a voltage is induced from primary to secondary coil. Then, a voltage is reflected to the primary

side. These voltages are described with reference to the mutual inductance (M) primary and secondary currents, and the operational frequency (ω).

$$v_1(t) = V_1 \sin(\omega t) \qquad (1.3)$$

Rewriting (1.3) as a phasor and defining the input voltage as the reference results in

$$\boldsymbol{V}_1 = V_1 \angle 0^0 \qquad (1.4)$$

Applying Kirchhoff's law to the circuit shown in Figure 2, voltage equations can be derived as follows

$$\boldsymbol{V}_1 = (R_1 + j\omega L_1)\boldsymbol{I}_1 - j\omega M \boldsymbol{I}_2 \qquad (1.5)$$

$$0 = -j\omega M \boldsymbol{I}_1 + (R_2 + j\omega L_2 + R_{eq})\boldsymbol{I}_2 \qquad (1.6)$$

$$\boldsymbol{V}_2 = R_{eq}\boldsymbol{I}_2 \qquad (1.7)$$

In equations (1.5)-(1.7), the signals $\boldsymbol{V}_1$ and $\boldsymbol{V}_2$ state the input and output voltage phasors. $\boldsymbol{I}_1$ and $\boldsymbol{I}_2$ represent the input and output current phasors. R_1 and R_2 are the AC resistances of the transmitter and receiver. R_{eq} describes the equivalent load resistance reflected to the WPTS. Mutual inductance (M) generally is calculated using finite element analysis (FEA).

Equation (1.8) gives the relationship among inductances in the system. The coupling coefficient (k) is directly proportional to the mutual inductance (M) from the coils interaction. L_1 and L_2 are the inductances of the coils. In equation (1.9), operating angular frequency, ω, is given by the switching frequency (f_s) of the inverter.

$$k = \frac{M}{\sqrt{L_1 L_2}} \qquad (1.8)$$

$$\omega = 2\pi f_s \qquad (1.9)$$

1.3. Current Research

As mentioned in the previous sections, RPEVs have attracted attention from research teams worldwide. A summary of these groups is presented in TABLE 1.

TABLE 1. RESEARCH TEAMS AROUND THE WORLD WORKING IN DYNAMIC WIRELESS POWER TRANSFER SYSTEMS

RESEARCH TEAM	LOCATION
Auckland University Research Team	Auckland, New Zealand
Bombardier Research Team PRIMOVE	Germany and Belgium
Oak Ridge National Laboratory (ORNL) Team	East Tennessee, USA
KAIST Research Team OLEV	Daejeon, Korea
INTIS	Munich, Germany
WiTricity	Boston, USA
Qualcomm Halo	San Diego, USA

A review of WPT prototypes has been carried out in this project. Either static or dynamic systems have been considered. A summary of the literature reviewed is displayed in TABLE 2. This highlights relevant parameters, including output power, air gap, operating frequency, size and shape of coils and the compensation topology of the system.

Highly efficient wireless power transfer systems have promised great potential, with some designs achieving over 90% efficiency. The system designed by the University of Michigan-Dearborn can transfer 3.3 kW with 95% efficiency, this is impressive as it indicates that wireless chargers may now be compared with wired ones [5].

In the United States, another wireless charging system prototype for EV has been developed at Oak Ridge National Laboratory (ORNL). Its efficiency reaches 90% for 3 kW of power [31].

TABLE 2. CURRENT WIRELESS POWER TRANSFER SYSTEMS DEVELOPED BY RESEARCH GROUPS

GROUP	POWER OUTPUT kW	η %	AIR GAP cm	f_s kHz	SIZE cm^2	GEOMETRY OF COIL	CT	REF.
Utah University	5	90[1]	20	17.5-26.5	Tx 5178 Rx 5178	Round - Round	LCC-LCC	[32]
University of Auckland	2	-	20	20	Tx 3848 Rx 3848	Round - Round	LCL-LCL	[16]
	2-7	-	10-25	20	Tx 3100 Rx 3100	DD-DDQ - Rectangular	Parallel - Parallel	[22]
	1	91[2]	10	85	Tx 1385 Rx 1385	Round - Round	Series - Series, Parallel - Parallel	[20]
University of Michigan-Dearborn	3.3	95[3]	15	1000	Tx 1024 Rx 1024	Rectangular - Rectangular	LCC	[33]
	6	95[2]	15	95	Tx 3600 Rx 3600	Rectangular - Rectangular	LCC	[34]
	7.7	96[3]	20	79	Tx 4800 Rx 4800	Rectangular - Rectangular	-	[35]
ETH Zurich	5	95[2]	5.2	100	Tx 346 Rx 346	Round-Round	Series - Parallel	[36]
Nissan Research Centre	3	80[2]	5	20	Tx 7750 Rx 7750	Round-Round	Parallel - Series, Parallel - Parallel	[37]
	1	90[2]	10	100	Tx 4800 Rx 1256	Rectangular - Round	Parallel - Series, Parallel - Parallel	[38]
TUM Technische Universitat Munchen	20[4]	83 - 95	30	20	Tx 22500 Rx 22500	Rectangular - Rectangular	Series - Series	[39]

[1] Grid to Battery Efficiency
[2] AC-AC Efficiency
[3] DC-DC Efficiency
[4] Theoretical design

Institution	Power (kW)	Frequency		Efficiency	Dimensions	Coil Type	Compensation	Ref.
KAIST *Korea Advanced Institute of Science and Technology*	3	80^3	1	20	Tx width 20 cm (rail) Rx 990	E-type - DD	Series - Series	1G (Golf Car) [4]
	6	72^3	17	20	Tx width 140 cm (rail) Rx 9600	U-type - DD	Series - Series	2G (Bus) [4]
	15	71^3	17	20	Tx width 80 cm (rail) Rx 1385	W-type - DD	Series - Series	3G (SUV) [4]
	15	83^3	20	20	Tx width 80 cm (rail) Rx 13600	W-type - DD	Series - Series	3+G (Bus) [4]
	15	74^3	12	20	Tx width 80 cm (rail) Rx 13600	W-type - DD	Series - Series	3+G (Train) [4]
	25	80^3	20	20	Tx width 10 cm (rail) Rx 8000	I-type - DD	Series - Series	4G (Bus) [4]
	22	71^3	20	20	Tx width 72 cm (rail) Rx 9800	S-type - DD	Series - Series	5G [4]
	100 (5 x 20 kW)	80^3	26	20	Tx width 4 cm (rail) Rx 8000	E-type - DDQ	Series - Series	[40]
	3.3	83^3	10-30	85	Tx 14000 Rx 2500	Rectangular - Rectangular	Series - Series	[41]

University of Michigan-Dearborn	1.4	89[3]	15	85	Tx 1552 Rx 1940	Rectangular-Rectangular	LCC-LCC	[5]
University of Seoul	180 (3 x 60 kW)	85[1]	7	60	Tx width 48 cm (rail) Rx 5520	E-Type - DDQ	Series - Series	[42]
ORNL	1.5	75[3]	100	23	Tx 33 Rx 855	Round - Round	Series - Series	[43]
Oak Ridge National Laboratory	3	90[1]	-	24	-	Round - Round	Series - Parallel	[31]
NCSU *North Carolina State University*	.3	78	170	100	Tx 35 Rx 1225	Round - Round	Series Parallel - LCC	[44]

1.4. Thesis Statement

The aim of this Masters project is the integration of a secondary-side-only control into an existent dynamic wireless power system under two different compensation topologies, *i.e.* double-sided LCC and series-series CTs. An estimation equation for coupling coefficient and a controller for the double-sided LCC compensation topology are introduced. A comparison study between these two topologies comprised of their characteristics and response to the controller has been carried out.

Chapter 2

2. Dynamic Wireless Power Systems Design

As discussed in the previous chapter, RPEVs are ideal candidates for future means of transportation. This includes passenger cars, fleet vehicles, trucks, trains and tramways. Previously wires were used as an alternative to implementing RPEVs. These wires were connected to the grid via pantographs, which are current collecting devices mounted on the roof of EVs. Nevertheless, pantographs are not widely used at present as a result of maintenance problems and safety concerns in urban areas [4].

A DWPTS for RPEV applications comprises of two subsystems. First, the road that powers the car, known as the power supplier. Second, the pad placed at the bottom of an EV and all the components for power conditioning, known as the power receiver. These subsystems are constituted by the stages displayed in Figure 3.
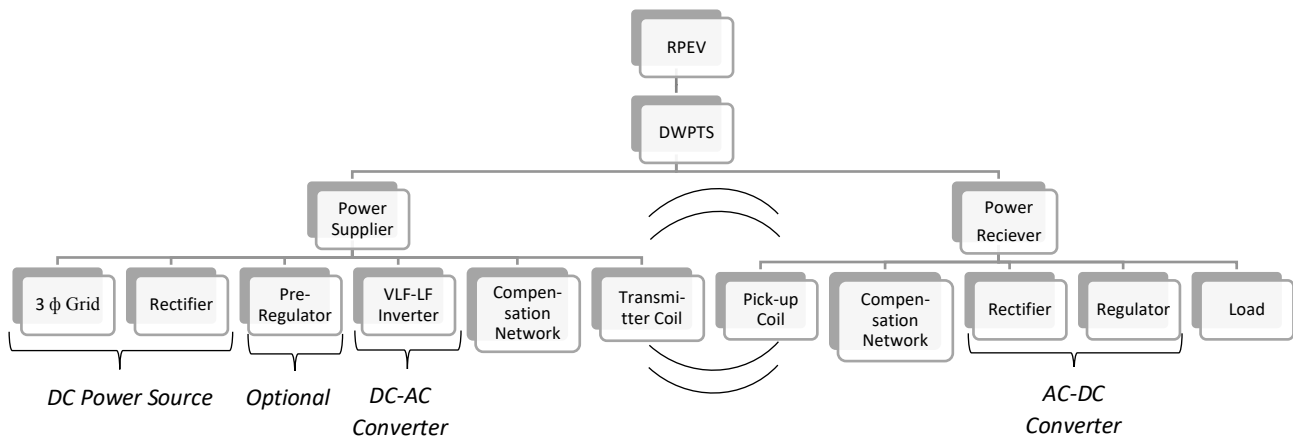
Figure 3. Configuration of a dynamic wireless power transfer system

As previously discussed, a dynamic charger is configured by different stages. The first is the power source. Existing utility power is converted to an appropriate higher frequency current source employing an inverter. If the utility power is an AC source, a previous rectification stage must be carried out. Once the alternating current meets the suitable frequency and amplitude levels, power flows to the transmitter track through a compensation network. A magnetic field is established in the primary side and the pick-up coil captures the generated magnetic flux. As a result, a voltage is induced on the receiver side. A reactive compensation network is similarly

used on this side. Compensation networks, from both secondary and primary subsystems, improve the power transfer by reducing reactive power.

In general, DC power at a certain level is demanded. For this reason, the next stage is an AC-DC conversion for power conditioning. This is routinely achieved by rectifying the output of a secondary compensation network and then regulated, to suitable levels, using a switch mode DC-DC converter.

It can be inferred from the preceding description that the DWPTS configuration does not differ from the static configuration. The stages remain the same, however, design considerations for the elements at each stage change for a dynamic system. The main design considerations for wireless charging systems are [28]

- o Both Static and Dynamic
    - Magnetic design (increase coupling coefficient through shape and size)
    - Tolerance to large air gaps
    - Power efficiency
    - Power transfer capacity
    - Cancelation EMF
- o Only Dynamic
    - Tolerance to unavoidable varying lateral misalignment
    - Cost per kilometre
    - Resistance to road conditions and installation

In comparison to stationary chargers, several parameters are considered constant while charging, dynamic systems represent a greater challenge in regards to load and coupling coefficient variations to maintain high efficiency and power delivery. Therefore, a good strategy of control should be chosen depending on the configuration of the system.

The power consumption test for a Mitsubishi i-MiEV is used as reference to demonstrate a varying load [45]. In this test the power consumption on a highway is 8.7 kW at a speed of 73 km/h. At 112 km/h, this increases to 25.3 kW. Thus, the power supplied should be significantly higher than 26 kW, in order for charging of the vehicle battery at a speed of 112 km/h. Moreover, load variations result from the speed of the car, the slope of the road and DC load of electronic devices in the EV.

Alternatively, coupling coefficient variations are related to lateral misalignment and the ground clearance of the EV. As previously mentioned, the coupling coefficient describes the quality of interaction of two coils across a magnetic field. This means that a larger overlapping area and closer gap between coils, results in a higher the coupling coefficient. However, the air gap varies depending on the on-board load, and can be as low as 100 mm [46]. Moreover, the air gap varies due to horizontal misalignment, which is an unavoidable variable of driving patterns.

In terms of deployment of the system on roads, DWPTS design should consider practical integration techniques such as compact pre-built modules, isolation methods and cooling systems [39].

TABLE 3. SPECIFICATIONS OF I-MIEV

i-MiEV SPECIFICATION	DESCRIPTION
Battery Type	Lithium Ion
Battery Voltage (V)	330
Battery Resistance (Ω)	0.09
Battery energy (kWh)	16
Dimensions length x width x height (mm)	3475 x 1475 x 1610
Gross Vehicle Weight (kg)	1450
Ground clearance (Air Gap) (mm)	150
Range (Japan Driving Cycle) (km)	160
*Electric energy consumption (NEDC) *2 (Wh/km)*	125
Maximum speed (km/h)	130
Motor Maximum Power (kW)	47
Regular charging (AC 230V 1 phase) "16A"	Approx. 6 hrs
Regular charging (AC 230V 1 phase) "10A"	Approx. 8 hrs
Regular charging (AC 230V 1 phase) "8A"	Approx. 10 hrs
Quick-charging "125A, 400 V"	Approx. 30 mints

The components at each stage of a DWPTS (listed below) are detailed in this chapter with consideration given to the design criteria explained above.

- Coil Structure (Transmitter & Receiver coils)
- DC-AC Conversion (Inverter)
- Compensation Networks
- AC-DC Conversion (Rectifier & Regulator)

The AC-DC conversion stage is addressed in chapter 3 as the subject of this research. Moreover, it is important to highlight that the charging objective of this project is the electric vehicle Mitsubishi i-MiEV (specifications shown in TABLE 3). This is because Durham Energy Institute owns one and this research can be further developed for future implementation purposes.

2.1. Coil Structure

Coil design involves driving the magnetic field from the transmitter to the receiver, reducing leakage flux. As a consequence, large induced voltage and low EMF levels are reached. The geometry of the coil plays an important role. Geometry determines important parameters, including tolerance to misalignment and coupling coefficient. Circular [16, 20, 32, 36, 37], rectangular [33, 34, 39, 41], D, double D [22], I and S [28] are examples of possible geometries. The geometries are named after their shape. For example, D refer to a coil whose shape looks like a letter 'D'. The double D refers to a coil that looks like two 'D' together (DD). In the same way, I, S, and E shapes are named after the appearance of the coils. A DDQ pick-up is a particular case of a double D geometry which has a Q shape coil on it overlapping the two D coils. Moreover, the receiver and transmitter may or may not have the same geometry and dimensions. Thus, the relationship between coils can be symmetric or asymmetric. Circular planar type is extensively used for static charging and was first developed [41] with a symmetric relationship. However, rectangular type geometries have been shown to exhibit better performance in a dynamic scenario [4, 13]. This is because of its misalignment tolerance and magnetic coupling. OLEVs use I, E and S-type supply rails with multiple DDQ pickups, in an asymmetric relationship.

2.1.1. Receiver and Transmitter Track

In terms of design parameters, the size of the receiver is limited by the chassis width and length. In the case of a transmitter track, there is more freedom and two different design methodologies (segmented and elongated) can be adopted [5, 47]. An elongated track considers a transmitter track much larger than the receiver. It supplies continuous power to the moving vehicle over the pad. In addition, a larger pad allows a reduction in the number of system components and serves multiple vehicles simultaneously. The main disadvantage of this system is the substantial AC resistance and inductance of the pad, resulting in low efficiency of 70% to 80% [5]. In a segmented track, the transmitter and receiver are approximately the same size. Hence, several short transmitters are placed, one next to the other, along the road track. The major drawback of this design methodology is the number of components employed for each pad, which significantly increases costs. In addition, a detection strategy must be implemented to switch the pads on only in the presence of an EV, in order to achieve high efficiency and low EMF emissions [44]. In this project, a segmented track is adopted. It is assumed that the transmitter tracks are turned on only when an EV is detected and there are no power losses during this process. Its disadvantage, which was mentioned above, is addressed by reducing the number of components in the control stage.
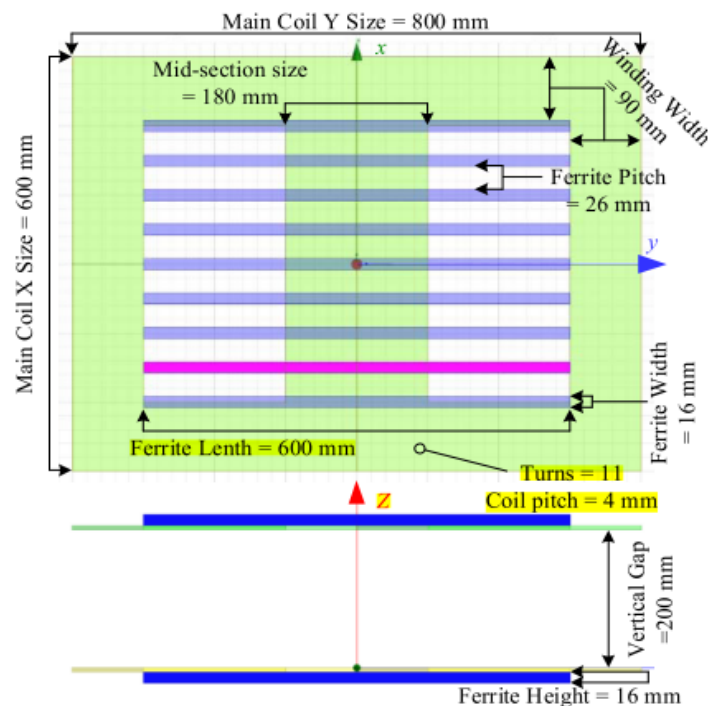

Figure 4. Coils dimensions of WPTS [48]

The coil system presented in Figure 4 was selected based on the literature review [48]. The objective of the project is to maximise transference efficiency rather than design the coils. It shows a WPTS with a power capacity of 7.7 kW, coupling coefficient from 0.18 to 0.32 at 79 kHz and an AC-AC efficiency of approximately 96%. Moreover, the transmitter and receiver coils are symmetric and have a DD geometry, therefore, the configuration adopted for the transmitter is segmented track. It is noted that the range of k is given by the designers of the system, and it is determined by the best and worst scenario of the alignment of the receiver and transmitter. In this case, when the system is perfectly aligned, k equals 0.32. On the other hand, when there is a lateral misalignment of 30 cm, the value of k drops to 0.18.

2.1.2. Electro Magnetic Field

The security of living beings within the surrounding area of the system is an important issue that requires addressing. The total EMF from both transmitter and receiver should be lower than guidelines from the International Commission on Non-Ionizing Radiation Protection (ICNIRP) [49]. This states that the radiated flux density should be lower than 6.25 µT [42]. There are three measurement positions that must meet this requirement: 200 mm horizontally from the external surface of the vehicle and at vertical heights of 500, 1000 and 1500 mm.

2.2. Inverter

Technology advances in the field of power electronics have boosted contactless power supply [18]. It has resulted in the development of solid-state DC-AC converters or, more commonly known, inverters. As the name implies, inverters make the 'inversion' from DC to AC. The switching frequency of the inverter plays an important role in the overall performance and design of the system. In WPTSs, it is usually set in in the range from 20 kHz and 100 kHz due to the fact that acoustic noise may represent an issue for switching frequencies lower than 20 kHz [14]. In addition, switching and component losses become considerably higher at frequencies above 100 kHz [18]. The frequency range is also limited by the standard guidelines of each country. Switching frequency, f_s, sets the operating frequency, f_0, of the system as shown in equation (1.9).

In addition, there is a trade-off between switching frequency and the size of the system's components. If f_s increases, then the coil and capacitor size decrease. Nevertheless, the skin effect in the wires leads to switching and core losses [4]. The skin effect denotes the non-

uniform distribution of the current across the conductor at high frequencies. The current tends to flow on the "skin" of the wire raising its AC resistance. Litz wire is commonly used to solve the problem [50].
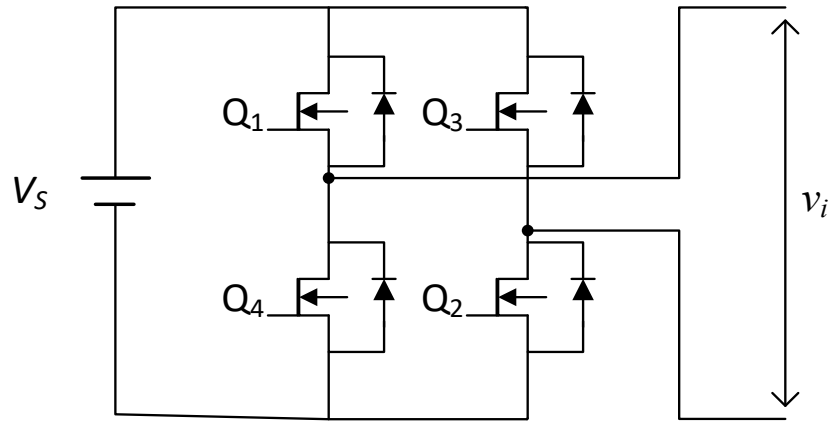
Figure 5. Single-phase inverter in full bridge topology

A single-phase full bridge inverter has been used in this project. It consists of four transistors. When transistor Q_1 and Q_2 are switched on at the same time, the inverter voltage, v_i, equals V_s (voltage amplitude of DC source). Then, if Q_1 and Q_2 are switched off, v_i equals 0 when an ideal scenario is considered at no reactive load. When transistor Q_3 and Q_4 are switched on while Q_1 and Q_2 remain switched off, v_i equals $-V_s$ as shown in Figure 6 (a).
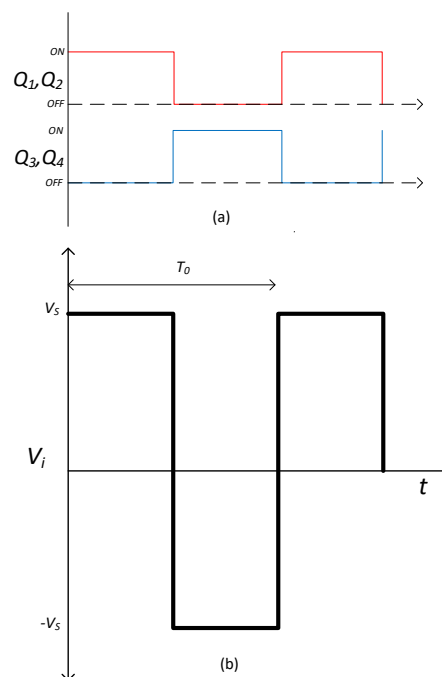
Figure 6. a) Gating signals b) Resulting ideal square wave voltage

Equations from (2.1) to (2.3) were taken from [51]. Equation (2.1) indicates the magnitude of the root mean square voltage of the inverter in the period T_0, which is V_s.

$$V_i = \left(\frac{2}{T_0} \int_0^{T_0/2} V_S{}^2 dt \right)^{1/2} = V_s \tag{2.1}$$

The first harmonic analysis (FHA) is used to study the circuit in equations (2.2) and (2.3). It is a basic analysis method that considers only the fundamental component of the output voltage of the inverter. In equation (2.2), v_i is the AC output voltage of the inverter, which is the summation of all its harmonics.

$$v_i = \sum_{n=1,3,5\ldots}^{\infty} \frac{4V_s}{n\pi} \sin(n\omega t) \tag{2.2}$$

The parameter n refers to the harmonic number. For $n = 1$, the root mean square (RMS) value of the voltage of the first harmonic of the inverter voltage (V_{1_RMS}) is

$$V_{1\_RMS} = \frac{4V_s}{\sqrt{2}\pi} = 0.9V_s \tag{2.3}$$

2.3. Compensation Network

Resonating compensation circuits are required to reduce inductive reactance and mitigate voltage drop in leakage inductances of coils, thus minimising the VA rating. The reduction of reactance is achieved by adding reactive elements, such as inductors and capacitors. Moreover, the compensation network can be designed for realising a zero phase angle (ZPA), zero voltage switching (ZVS) and zero current switching (ZCS) operation. ZPA means that voltage and current of the pads are in phase. The angular frequency that results in a ZPA is called resonance angular frequency (ω_0). In designing a ZPA compensation network, first, an operating angular frequency is selected. Second, this operating angular frequency is set to the resonance angular frequency of the system.

$$\omega = \omega_0 = 2\pi f_s \tag{2.4}$$

Finally, elements values from the chosen compensation topology are calculated with respect to the system parameters. For a pure sine wave input voltage, ZVS and ZCS are ensured by the ZPA operation. However, if the input voltage is a square wave, high-order harmonics have

relevant effects on the inverter at switching. Therefore, ZPA does not guarantee ZVS and ZCS. For this scenario, the load must be inductive to accomplish ZVS [52]. Consequently, a secondary series capacitor is usually varied to have an inductive load.

Depending on the source and load types, different compensation topologies can be adopted as presented in Figure 7. In this research, a comparison between series-series (SS) and double-sided inductor-capacitor-capacitor (LCC) topologies is carried out. Moreover, ZPA operation is achieved neglecting the effect of high-order harmonics.

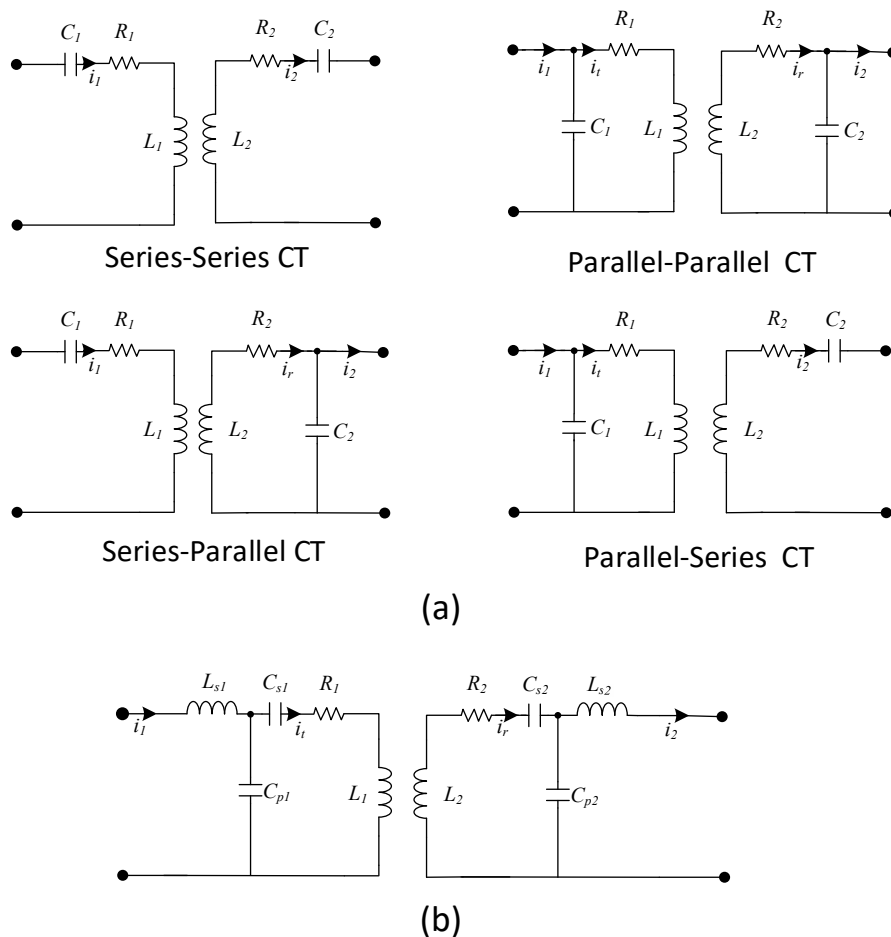Figure 7. (a) Basic compensation topologies (b) Double-sided Inductor-Capacitor-Capacitor compensation topology

2.3.1. Series-series Compensation Topology

Of the four basic topologies for compensation in resonant circuits (Figure 7(a)), SS compensation topology is widely adopted for dynamic applications [20, 36, 39-42, 53, 54]. This regards the dynamic nature of roadway-powered systems. Resonating capacitors values

do not depend on coupling coefficient nor load impedance [55] under a dynamic scenario. Thus, resonance frequency can be fixed. An SS topology is illustrated in Figure 8. Series capacitors, C_1 and C_2, are connected to the corresponding transmitter and receiver. Due to the series topology on the transmitter and receiver side in SS compensated systems, transmitter and input currents refer to the same one, i_{1_ss} . Likewise, receiver and output currents denote the same current, i_{2_ss}.
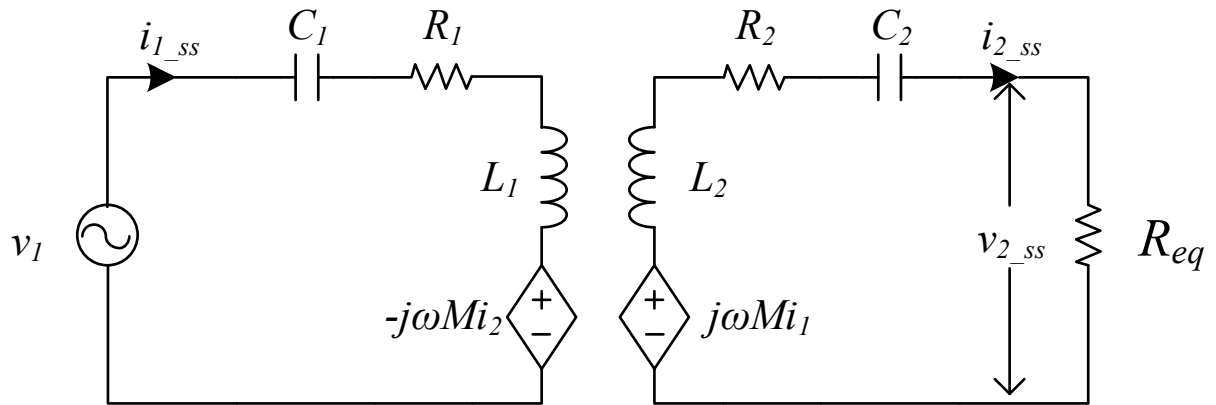
Figure 8. Series-series compensation topology equivalent circuit

The circuit in Figure 8 is defined by Kirchhoff's law as follows

$$\boldsymbol{V}_1 = \left(R_1 + j\left(\omega L_1 - \frac{1}{\omega C_1} \right) \right) \boldsymbol{I}_{1\_ss} - j\omega M \boldsymbol{I}_{2\_ss} \tag{2.5}$$

$$0 = -j\omega M \boldsymbol{I}_{1\_ss} + \left(R_2 + j\left(\omega L_2 - \frac{1}{\omega C_2} \right) + R_{eq} \right) \boldsymbol{I}_{2\_ss} \tag{2.6}$$

$$\boldsymbol{V}_{2\_ss} = R_{eq} \boldsymbol{I}_{2\_ss} \tag{2.7}$$

Using equations (2.5) and (2.6), one can set the conditions for achieving zero reactance by applying equation (2.4). Thus, in equation (2.9) capacitance values can be calculated from equation (2.8).

$$0 = \omega_0 L_1 - \frac{1}{\omega_0 C_1} = \omega_0 L_2 - \frac{1}{\omega_0 C_2} \tag{2.8}$$

$$C_1 = \frac{1}{L_1\omega_0{}^2}$$
$$C_2 = \frac{1}{L_2\omega_0{}^2}$$

(2.9)

Once the compensation has been determined, the equations that follow describe the behaviour of the system [56]. A_{V_ss}, A_{I_ss} and A_{P_ss} represent the voltage, current and power gains. A gain is the ratio between the output and input of a system. The power gain is also known as the efficiency, $\eta_{\_ss}$, of the system.

$$A_{V\_ss} = \frac{\boldsymbol{V}_{2\_ss}}{\boldsymbol{V}_1} = j\frac{\omega_0 k\sqrt{L_1 L_2}R_{eq}}{R_1\big(R_2 + R_{eq}\big) + (\omega_0 M)^2}$$

(2.10)

$$A_{I\_ss} = \frac{\boldsymbol{I}_{2\_ss}}{\boldsymbol{I}_{1\_ss}} = j\frac{\omega_0 k\sqrt{L_1 L_2}}{R_2 + R_{eq}}$$

(2.11)

$$\eta_{\_ss} = A_{P\_ss} = \frac{P_{2\_ss}}{P_{1\_ss}} = \frac{\boldsymbol{V}_{2\_ss}\overline{\boldsymbol{I}}_{2\_ss}}{\boldsymbol{V}_1\overline{\boldsymbol{I}}_{1\_ss}} = A_{V\_ss}\overline{A}_{I\_ss}$$

$$= \frac{(\omega_0 k)^2 L_1 L_2 R_{eq}}{\big(R_2 + R_{eq}\big)\big[R_1\big(R_2 + R_{eq}\big) + (\omega_0 k)^2 L_1 L_2\big]}$$

(2.12)

The output power, $P_{2\_ss\_RMS}$, is determine as follows

$$P_{2\_ss\_RMS} = \frac{(\omega_0 k)^2 L_1 L_2 R_{eq}}{\big[R_1\big(R_2 + R_{eq}\big) + (\omega_0 M)^2\big]^2}V_{1\_RMS}^2$$

(2.13)

2.3.2. Double-sided LCC Compensation Topology

The LCC compensation topology is a series network with an additional inductor, L_s, in series and a parallel capacitor, C_p. When LCC topology is applied to both sides, transmitter and receiver, the compensation topology is known as double-sided LCC topology. This topology is represented as a mutual inductance model in Figure 9. Due to the double mesh at the transmitter and receiver, it should be noted that there are four different currents in the circuit. The input current, i_{1_lcc}, is the current that flows from the inverter to the input of the compensation circuit in the mesh one. The transmitter current, i_t, is the current that flows through the transmitter pad on the second mesh. The receiver current, i_r, denotes the current

22

that flows through the receiver pad in the third mesh. And the output current, i_{2_lcc}, refers to the current that flows from the receiver mesh to the equivalent resistance of the load connected to the output of the circuit in the mesh four.
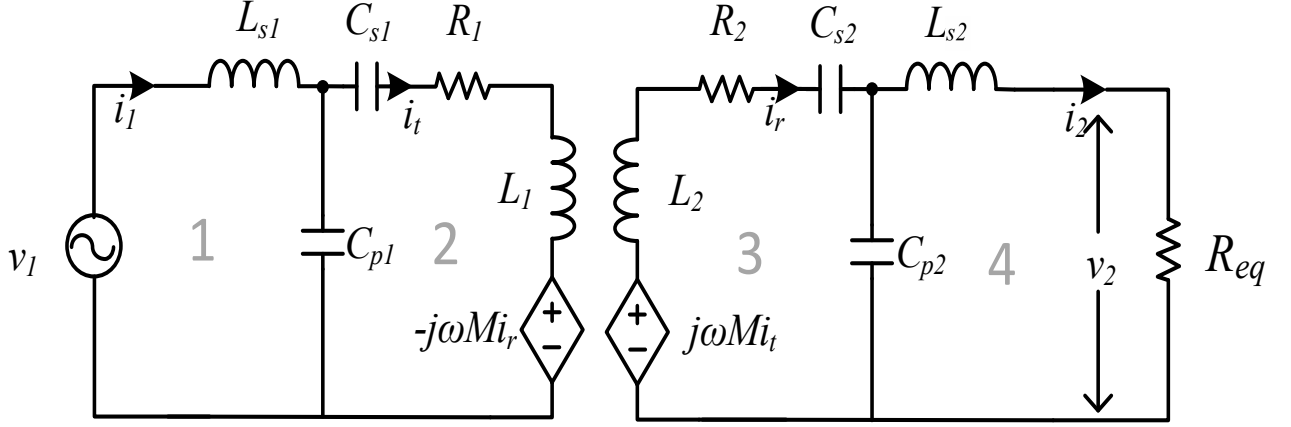
Figure 9. Doubled-sided LCC compensation topology representation through a mutual inductance circuit

Similarly to the series-series network, a double-sided LCC network can be defined by circuit theory. Using Kirchhoff's voltage law, one can derive an equation for each of the four loops.

Loop 1:

$$V_1 = j\left(\omega L_{s1} - \frac{1}{\omega C_{p1}}\right)I_{1\_lcc} - \frac{1}{j\omega C_{p1}}I_t \tag{2.14}$$

Loop 2:

$$0 = \frac{1}{j\omega C_{p1}}I_{1\_lcc} - \left(\frac{1}{j\omega C_{p1}} + \frac{1}{j\omega C_{s1}} + j\omega L_1 + R_1\right)I_t - j\omega M I_r \tag{2.15}$$

Loop 3:

$$0 = j\omega M I_t + \frac{1}{j\omega C_{p2}}I_{2\_lcc} - \left(\frac{1}{j\omega C_{p2}} + \frac{1}{j\omega C_{s2}} + j\omega L_2 + R_2\right)I_r \tag{2.16}$$

Loop 4:

$$V_{2\_lcc} = -j\left(\omega L_{s2} - \frac{1}{\omega C_{p2}}\right)I_{2\_lcc} + \frac{1}{j\omega C_{p2}}I_r \tag{2.17}$$

$$V_{2\_lcc} = I_{2\_lcc}R_{eq} \tag{2.18}$$

From (2.14) to (2.17), the resonance conditions can be defined as

$$0 = \omega_0 L_{s1} - \frac{1}{\omega_0 C_{p1}} \tag{2.19}$$

23

$$0 = \omega_0 L_1 - \frac{1}{\omega_0 C_{p1}} - \frac{1}{\omega_0 C_{s1}} \tag{2.20}$$

$$0 = \omega_0 L_2 - \frac{1}{\omega_0 C_{p2}} - \frac{1}{j\omega_0 C_{s2}} \tag{2.21}$$

$$0 = \omega_0 L_{s2} - \frac{1}{\omega_0 C_{p2}} \tag{2.22}$$

Thus, capacitance and inductor values to meet these conditions are calculated as follows

$$C_{p1} = \frac{I_t}{\omega_0 V_1} \tag{2.23}$$

$$L_{s1} = \frac{1}{\omega_0{}^2 C_{p1}} \tag{2.24}$$

$$C_{s1} = \frac{C_{p1}}{\omega_0{}^2 C_{p1} L_1 - 1} = \frac{C_{p1}}{\frac{L_1}{L_{s1}} - 1} \tag{2.25}$$

$$C_{p2} = \frac{I_r}{\omega_0 V_{2\_lcc}} \tag{2.26}$$

$$L_{s2} = \frac{1}{\omega_0{}^2 C_{p2}} \tag{2.27}$$

$$C_{s2} = \frac{C_{p2}}{\omega_0{}^2 C_{p2} L_2 - 1} = \frac{C_{p2}}{\frac{L_2}{L_{s2}} - 1} \tag{2.28}$$

Note that the value of I_t in (2.23) determines the value of the parallel capacitor. It means that depending of the amount of current desired on the transmitter track, the parallel capacitor can be sized.

From equations (2.14)-(2.18), important characteristics for this CT, such as the voltage ($A_{V_{lcc}}$), current (A_{I_lcc}) and power ($\eta_{\_lcc}$) gains, and output power (P_{2_lcc}) are derived and presented in equations (2.29)-(2.32).

$$A_{V\_lcc} = \frac{V_{2\_lcc}}{V_1} = -j\frac{k\sqrt{L_1 L_2}R_{eq}}{\omega_0 L_{s1} L_{s2}\left(1 + \frac{R_2 R_{eq} C_{p2}}{L_{s2}}\right)} \tag{2.29}$$

$$A_{I\_lcc} = \frac{I_2}{I_1} = -j\frac{\omega_0 k\sqrt{L_1 L_2}C_{p2}}{C_{p1}\left[R_1\left(1 + \frac{R_2 R_{eq} C_{p2}}{L_{s2}}\right) + \frac{k^2 L_1 L_2 R_{eq}}{L_{s2}^2}\right]} \tag{2.30}$$

$$\eta_{\_lcc} = A_{P\_lcc} = \frac{P_{2\_lcc}}{P_{1\_lcc}} = \frac{V_{2\_lcc}\bar{I}_{2\_lcc}}{V_{1\_lcc}\bar{I}_{1\_lcc}} = A_{V\_lcc}\bar{A}_{I\_lcc}$$

$$= \frac{k^2 L_1 L_2 R_{eq}}{L_{s2}^2 \left(1 + \frac{R_2 R_{eq} C_{p2}}{L_{s2}}\right) \left[R_1 \left(1 + \frac{R_2 R_{eq} C_{p2}}{L_{s2}}\right) + \frac{k^2 L_1 L_2 R_{eq}}{L_{s2}^2}\right]} \tag{2.31}$$

$$P_{2\_lcc\_RMS} = \frac{k^2 L_1 L_2 R_{eq}}{\left(\omega_0 L_{s1} L_{s2} \left(1 + \frac{R_2 R_{eq} C_{p2}}{L_{s2}}\right)\right)^2} V_{1\_RMS}^2 \tag{2.32}$$

Another design approach is to consider the factor $1/L_{s1}L_{s2}$. This factor allows for setting the amount of power to transmit.

2.3.3. MPTE Calculation for Double-sided LCC and SS CTs

Efficiency equations (2.12) and (2.33) were introduced in last sections. The efficiency of both systems depends on the element values chosen in the design stage, coupling coefficient and load. The coupling coefficient variation is constrained by the magnetic design and the geometry of the coils. Moreover, it varies depending on the alignment of the receiver and transmitter coils. However, magnetic shaping will not be addressed in this project. On the other hand, the misalignment of coils can be measured in horizontal and vertical directions. The horizontal misalignment is similarly known as lateral misalignment and it is not considered. The vertical misalignment, which corresponds to the moving direction of the vehicle, will be described in the next chapter. However, this is not a controllable variable as it varies according to the unpredictable driver's actions. Thus, load is the variable that can be controlled and is assumed to be pure resistive. To maximise the efficiency of the system, the impedance for maximum efficiency condition is calculated. This can be derived by determining the maximum value of the efficiency function with respect to the impedance, R_{eq}. It is realised as follows

$$\frac{\partial \eta(t)}{\partial R_{eq}} = 0 \tag{2.33}$$

For a SS compensated system, resistance for MPTE is calculated by applying equation (2.33) in equation (2.12).

$$R_{eq\_ss\_\eta MAX} = \sqrt{R_2\left(\frac{\left(\omega_0 k\sqrt{L_1 L_2}\right)^2}{R_1} + R_2\right)} \qquad (2.34)$$

Resistance for reaching maximum efficiency of the system, $R_{eq\_ss\_\eta MAX}$, was found in equation (2.34). As previously mentioned, SS and double-sided compensated systems are constant current sources. Hence, variable resistance produces variable voltage while the current magnitude remains the same. Based on this property, maximum efficiency is stated in terms of output voltage. By substituting equation (2.34) into equation (2.10), the output voltage of the system that meets the requirement of maximum efficiency condition can be found.

$$V_{2\_ss\_\eta MAX\_RMS} = \sqrt{\frac{R_2}{R_1}} \frac{\omega_0 k\sqrt{L_1 L_2}}{\sqrt{R_1 R_2 + \left(\omega_0 k\sqrt{L_1 L_2}\right)^2} + \sqrt{R_1 R_2}} V_{1\_RMS} \qquad (2.35)$$

Following the same procedure for double-sided LCC compensation, MPET conditions are as follows

$$R_{eq\_lcc\_\eta MAX} = \frac{\sqrt{C_{p2} L_{s2}^3 R_1 R_2\left(k^2 L_1 L_2 + C_{p2} L_{s2} R_1 R_2\right)}}{L_{s2} R_1 C_{p2}^2 R_2^2 + C_{p2} k^2 L_1 L_2 R_2} \qquad (2.36)$$

$$V_{2\_lcc\_\eta MAX\_RMS} = \frac{k\sqrt{L_1 L_2} R_{eq\_lcc\_\eta MAX}}{\omega_0 L_{s1} L_{s2}\left(\frac{R_2 R_{eq\_lcc\_\eta MAX} C_{p2}}{L_{s2}} + 1\right)} V_{1\_RMS} \qquad (2.37)$$

2.3.4. Characteristics Comparison of Double-sided LCC and series-series CTs

A relevant characteristic of both series-series and double-sided LCC wireless chargers is that these systems behave as constant current sources. That is to say that transmitter and receiver currents of the systems remain the same regardless load variations. To prove this characteristic, circuits from Figure 8 and Figure 9, are simulated in SIMULINK using the parameters of the systems from TABLE 4. Additionally, equations to calculate the output current of the systems are derived to compare the function approach with the measurements. By substituting (2.10) in (2.13), considering that $P_{2\_ss\_RMS} = V_{2\_ss\_RMS} I_{2\_ss\_RMS}$, and solving for $I_{2\_ss\_RMS}$, it yields

$$I_{2\_ss\_RMS} = \frac{\omega_0 k \sqrt{L_1 L_2}}{R_1 (R_2 + R_{eq}) + \left(\omega_0 k \sqrt{L_1 L_2}\right)^2} V_{1\_RMS} \qquad (2.38)$$

For the double-sided compensated system, equation (2.29) is substituted in (2.32) to obtain

$$I_{2\_lcc\_RMS} = \frac{k \sqrt{L_1 L_2}}{\omega_0 L_{s1} L_{s2} \left(1 + \frac{R_2 R_{eq} C_{p2}}{L_{s2}}\right)} V_{1\_RMS} \qquad (2.39)$$

Output currents of both systems are measured from the circuit model and compared with the equations (2.38) and (2.39) in Figure 10. Moreover, the maximum efficiency points $(R_{eq\_ss\_\eta MAX}, I_{2\_ss\_\eta MAX})$ and $(R_{eq\_lcc\_\eta MAX}, I_{2\_lcc\_\eta MAX})$ are calculated from equations (2.34) and (2.36) and similarly plotted on the same figure.
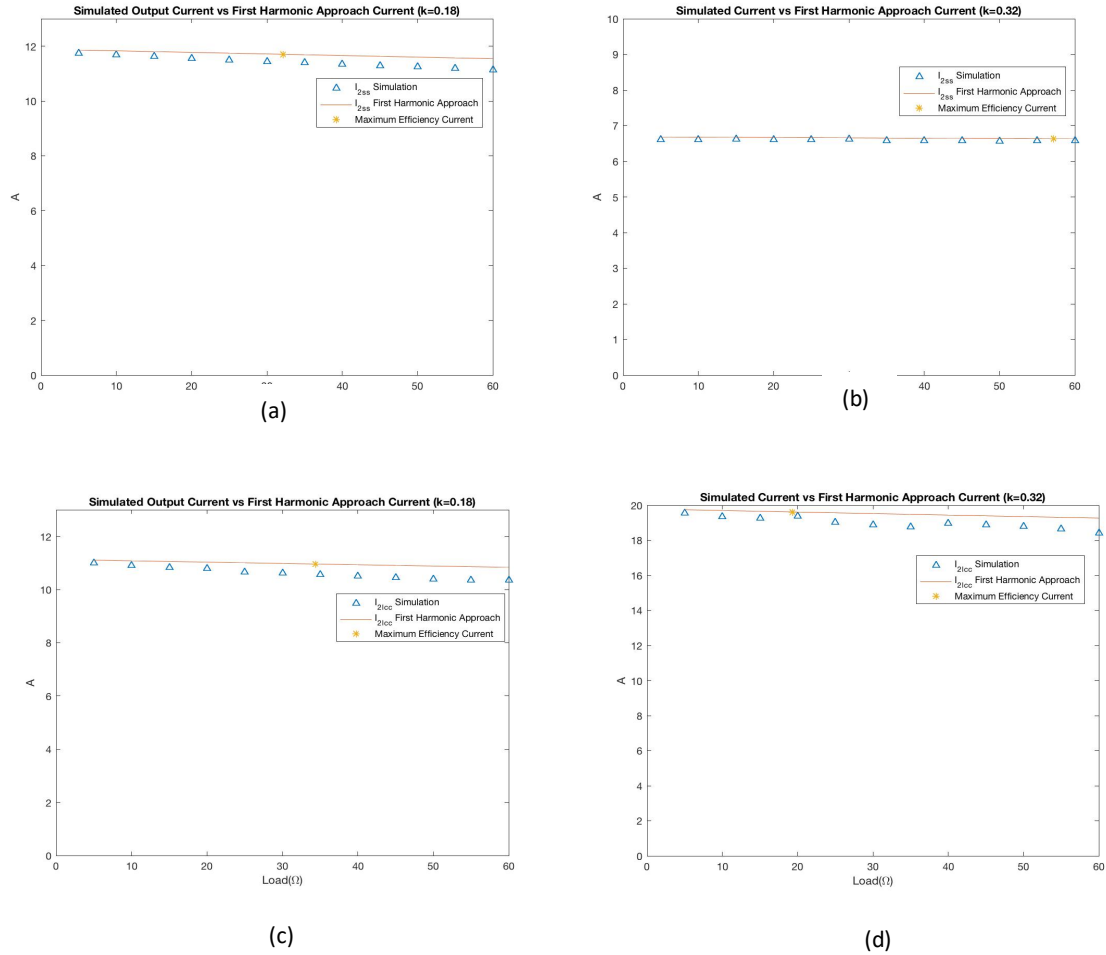

Figure 10. Comparison of calculated and simulated values of: a) Output current of the SS system at k=0.18 b) Output current of the SS system at k=0.32 c) Output current of the double-sided LCC system at k=0.18 d) Output current of the double-sided LCC system k=0.32

27

As can be seen from Figure 10, the variation of the current is small for a wide range of resistance in the x-axis for different values of k. Thus, these systems are considered as constant current sources. Additionally, it is noted that the proposed mathematical model of the double-sided LCC system and the model of the series-series system are consistent with the simulations results regarding output current.

From the same circuits, output voltage and AC-AC efficiency are likewise analysed. Output voltage and AC-AC efficiency are measured from the circuit and compared with the equations (2.12), (2.31), (2.10) and (2.29) that state η_{ss}, η_{lcc}, $V_{2\_ss\_RMS}$ and $V_{2\_lcc\_RMS}$, respectively, to validate the proposed approach in Figures 11 and 12. AC-AC efficiency refers to the efficiency from the input of the compensation network of the transmitter to the output of the compensation network on the receiver. Moreover, the maximum efficiency points $(R_{eq\_ss\_\eta MAX}, V_{2\_ss\_\eta MAX\_RMS})$ and $(R_{eq\_lcc\_\eta MAX}, V_{2\_lcc\_\eta MAX\_RMS})$ are calculated from equations from (2.34) to (2.37) and similarly plotted on the same figures. The equivalent resistance, R_{eq}, is on the x-axis and ranges from 0 to 60 ohms. It is because the maximum efficiency point is within this interval for values of k from 0.18 to 0.32, which is the range of the coupling coefficient for the chosen DWPTS.

First, from Figure 11 and Figure 12, it is noted that the proposed mathematical model of the double-sided LCC system and the model of the series-series system of the output voltage are consistent with the simulations results. Regarding the efficiency of the system, the series-series model, similarly matches with the simulation. However, the proposed efficiency model for the double-sided LCC system results do not correspond to the simulations. Despite this fact, the resistance for maximum efficiency matches for simulations and calculations as it can be seen in Figure 12 (b) and (d). Thus, it can be used to find the maximum efficiency voltage in the proposed output voltage model of the double-sided LCC system.

Then, in Figure 11 (a) and Figure 11 (c), one can observe that for the same load in a series-series compensated system, output voltage increases when the coupling coefficient decreases. Conversely, output voltage increases when the coupling coefficient decreases in double-sided compensated systems as shown in Figure 12 (a) and Figure 12 (c). Regarding this last observation, an great advantage can be found for the double-sided LCC systems. It was previously stated that segmented tracks strategy is adopted on this work. And, it was similarly assumed that a transmitter is turned on only when the vehicle is above it and then turned off.

The advantage of the double-sided LCC compensated systems against series-series systems lies on the switching losses. As stated at the beginning of the paragraph, a low k at switching the system off, i.e., near zero, means that the switching is done at large current and voltage for the SS compensated system while these parameters are relatively small for the double-sided LCC one.

Figure 11. Comparison of calculated and simulated values of the chosen SS system. a) Output voltage at k=0.18 b) AC_AC Efficiency at k=0.18 c) Output voltage at k=0.32 d) AC_AC Efficiency at k=0.32

For example, from the simulation models in SIMULINK of the circuits from Figure 8 and Figure 9, considering a coupling coefficient equals zero, the double-sided primary current is 1.6 A while for the series-series system is 378.5 A for a load of 30 ohms. It means that when the coils are switched off due to a low coupling coefficient, the double-sided compensation topology presents softer switching and lower losses compared to a series-series one.

Another characteristic to compare is the magnetic coupling sensitivity. On the one hand, series-series currents are sensitive to coupling coefficient variations. On the other hand, transmitter and receiver currents of a system under a double-sided LCC compensation topology are insensitive to coupling variations [57], which represents a great advantage for control purposes. Input voltage is usually varied to adjust the change of coupling coefficient to control the transmission power. If the system is insensitive to these variations, the control stage on the transmitter side can be omitted by setting a constant input voltage reducing the control system to only the receiver side. Furthermore, an LCC network decreases voltage and current stresses in the components of the system [48] because it has more components and the voltage is distributed among them. Another advantage from both topologies is that if the networks are symmetric, it helps to simplify the design process and to operate at the same fixed operating frequency on both sides.
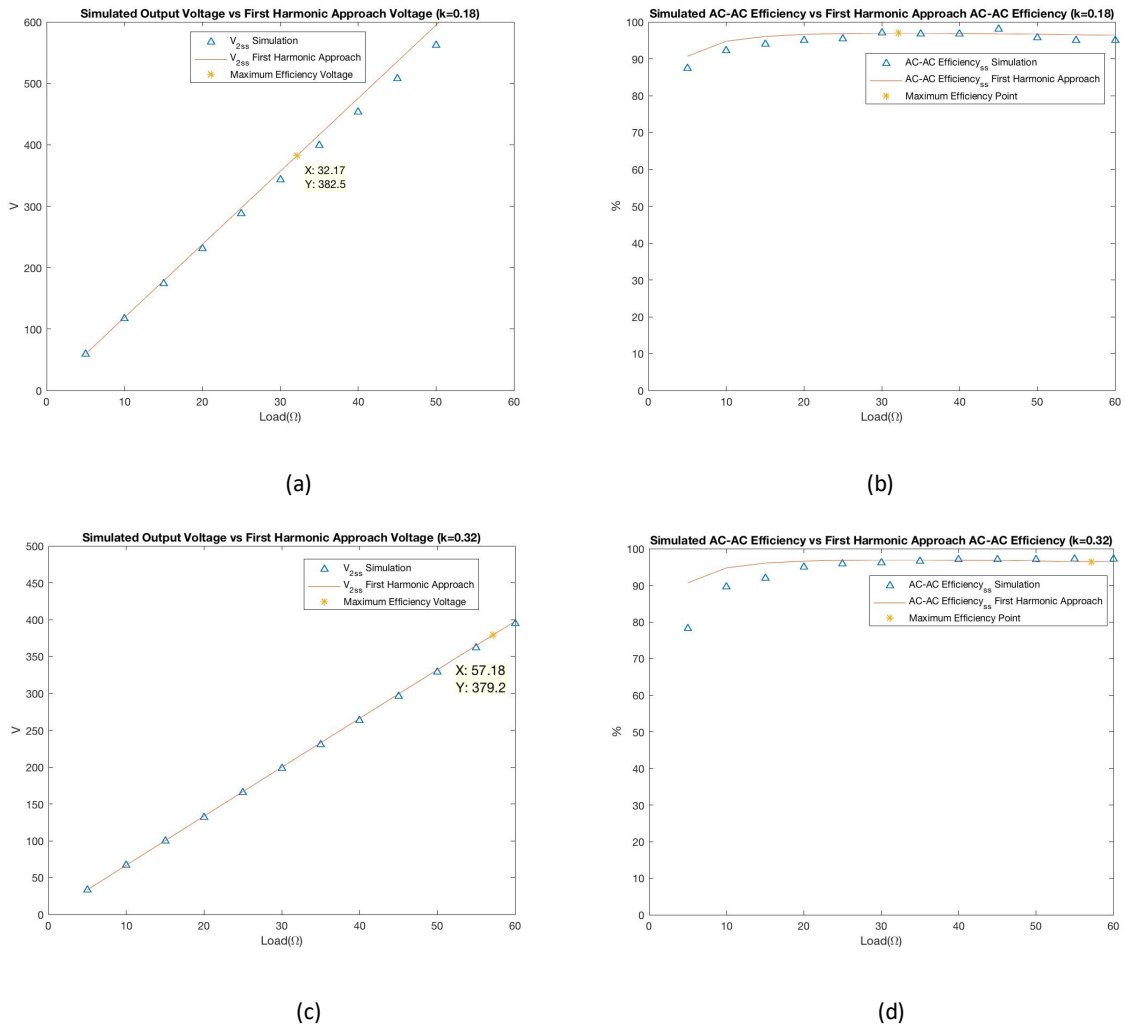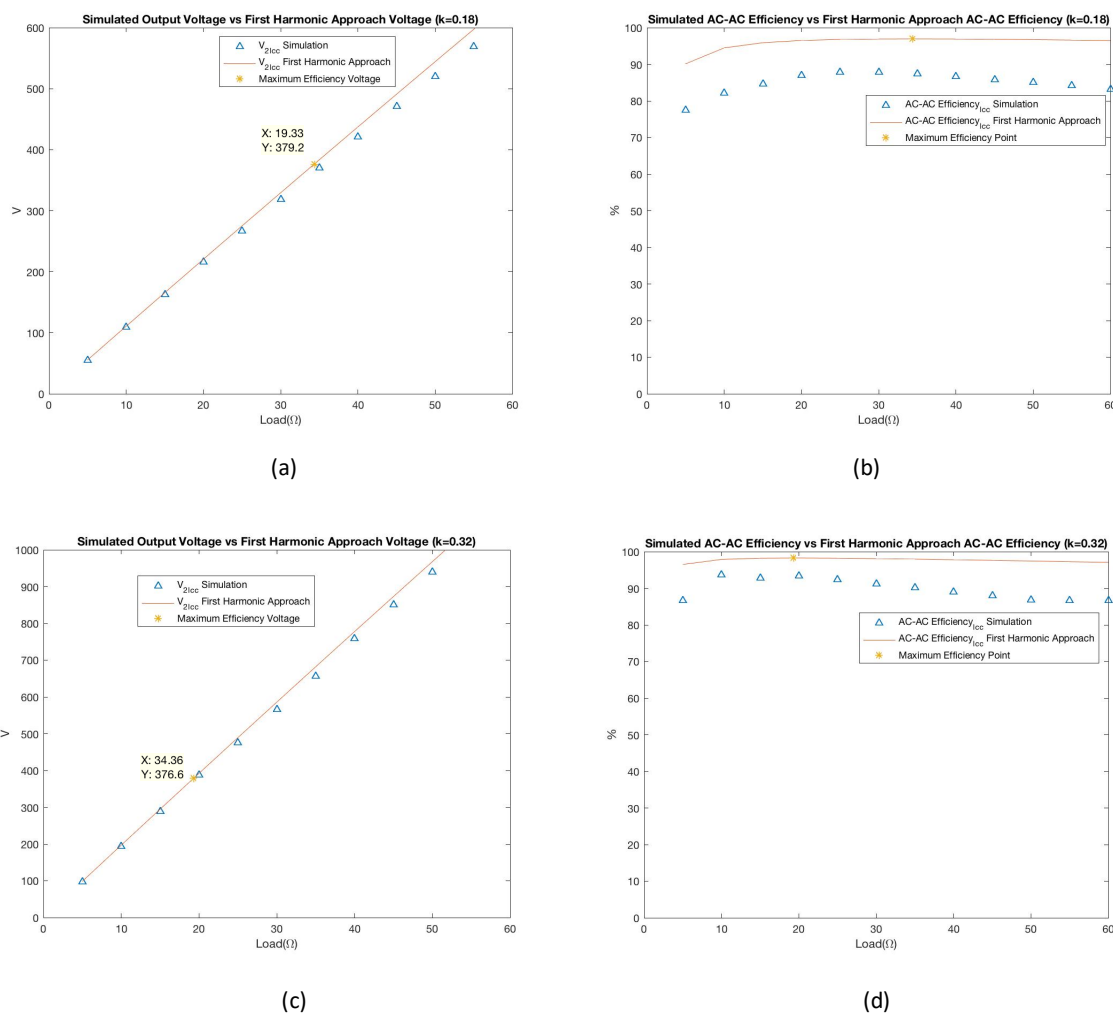

(a)

(b)

(c)

(d)

Figure 12. Comparison of calculated and simulated values of the chosen double-sided LCC system. a) Output voltage at k=0.18 b) AC_AC Efficiency at k=0.18 c) Output voltage at k=0.32 d) AC_AC Efficiency at k=0.32

In regards to the design of the system at fixed input voltage and operating frequency. For the series-series system, the transmitting power can be only adjusted by modifying the magnetic coupling or the load. On the other hand, apart from the modification of the load and coupling coefficient, the parallel capacitor (C_{p1}) fixes the magnitude of the current in the transmitter track in the double-sided LCC compensation system as shown in equation (2.23) by selecting the desired transmitter current, as mentioned in section 2.3.2. This is advantageous because power delivery can be additionally manipulated by varying the value of the parallel capacitor in comparison with the SS compensated system. Nevertheless, this value should be chosen carefully because efficiency similarly depends on it. This project will focus on maximum efficiency tracking rather than maximum power delivery. For this reason, the same values of elements of the double-sided system chosen from literature review, which was shown in Figure 4, are kept and series-series system elements values are calculated according to equations in section 2.3.1. These values are presented in TABLE 4.

TABLE 4. PARAMETERS OF THE SS AND DOUBLE SIDED LCC SYSTEMS

PARAMETER	SS CT	DOUBLE-SIDED LCC CT
V_{in} (*V*)	425	425
f_0 (*kHz*)	79	79
k	0.18-0.32	0.18-0.32
L_1 (*μH*)	360	360
L_2 (*μH*)	360	360
R_1 (*mΩ*)	500	500
R_2 (*mΩ*)	500	500
C_1 (*nF*)	11.274	-
C_2 (*nF*)	11.274	-
C_{p1} (*nF*)	-	60.6
L_{s1} (*μH*)	-	66.975
C_{s1} (*nF*)	-	13.851
C_{p2} (*nF*)	-	60.6
L_{s2} (*μH*)	-	66.975
C_{s2} (*nF*)	-	13.851

Chapter 3

3. Control

A DWPTS will suffer from degradation of power transfer efficiency (PTE) and stability, in a real case scenario for a dynamic system with varying parameters, including coupling coefficient, misalignment and transfer distance, and load [58]. Moreover, while moving forward, power is transferred by pulses from each transmitter causing an output power ripple [59]. In addition, efficiency for a system of this kind is highly dependent to the speed of the vehicle. Thus, as previously discussed, some control measures should be considered.

3.1. Control Considerations

Regardless the controller type, the work of the controller for the DWPTS should be to mitigate high voltage and current peaks, as well as to adequately regulate the power to achieve high efficiency and/or certain power target in a period of time. Hence, one can divide the control considerations in: time and overshoot percentage, efficiency and high power.

3.1.1. Time and overshoot

In order to know the required response time of the controller, the time that the EV spends on each transmitter, T_t, is determined by

$$T_t = \frac{l_t}{v_{EV}} \tag{3.1}$$

Where, l_t is the length of the track and v_{EV} is the speed of the electric vehicle. Considering an EV moving at 110 km/h across the chosen transmitter of 800 mm length, the vehicle will stay on the transmitter only 0.0262 seconds. Thus, the charging power signal should be smooth and quicker than this period.

3.1.2. Output power pulsations

Output pulsations of power are directly related to the speed of the car. The coupling coefficient varies according to the pose of the receiver with respect to the transmitter embedded on the roadway. If lateral misalignment is neglected, one can analyse the variation of the coupling coefficient of each transmitter on the moving direction. Moreover, the coupling coefficient between a transmitter with respect to another transmitter nearby is called self-coupling

coefficient. The direction of the magnetic flux linkage coil to coil gives the sign of the coupling coefficient [60]. Due to the fact that there is not overlapped area between adjacent transmitters, self-coupling coefficients are negatives. Thus, these coefficients reduced the coupling coefficient of each transmitter and the receiver. For short tracks, which are the transmitter pads studied on this research, self-coupling between transmitters can be neglected if these are placed at a certain distance from each other. However, the output power pulsations increase by increasing the splitting distance. For example, at a distance of 30% of the transmitter length, output power pulsations amplitude reach 50% of the peak value according to [5]. Decreasing the distance between transmitters leads to reduce output power pulsations because the receiver interacts more frequently with a new transmitter while moving, which does not let the power to drop. Nevertheless, self-coupling from the nearby transmitters must be considered if the distance between transmitters is reduced. In this project, no distance between transmitter pads is chosen to reduce output pulsations and the variation pattern for same-size pads introduced by Lu et. al., which is shown in Figure 13, is assumed.

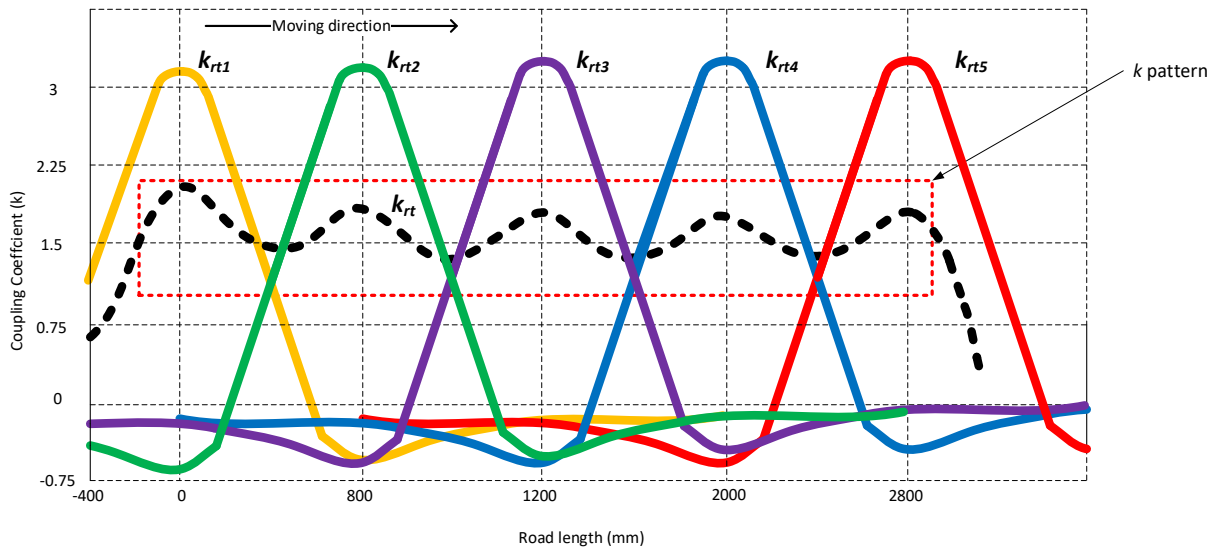Figure 13. Variation pattern of coupling coefficient for a transmitter and receiver of same size [5]

The pattern variation of coupling coefficient for each transmitter was calculated using FEA by Lu et. al., in the moving direction. The total coupling coefficient is equal to the summation of contributions of the coupling coefficient of each transmitter with the receiver placed on the bottom of the vehicle, $k_{rt\,i}$.

33

$$k_{rt} = \sum_{i=1}^{N} k_{rt\ i} \tag{3.2}$$

Where, N is the number of the transmitters embedded on the road. The contribution of each transmitter decreases the further it is from the receiver. During simulation, this pattern is achieved using a pulse block following the sequence as indicated in Figure 14.
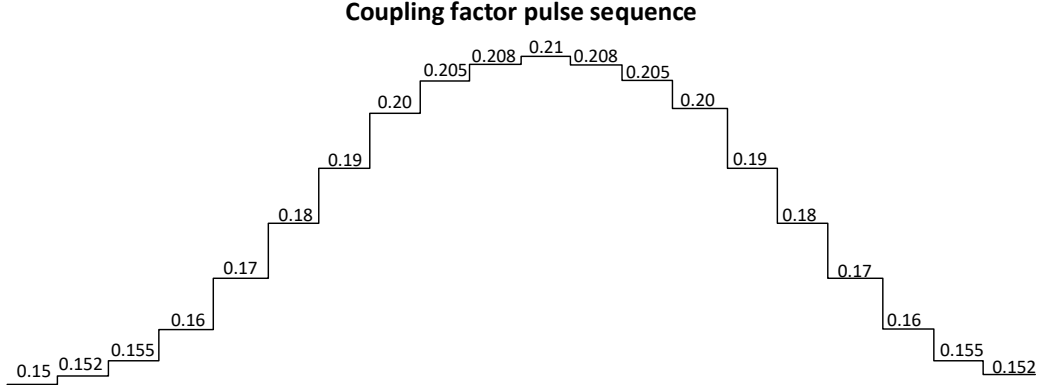

Figure 14. Proposed pulse sequence for coupling factor simulation

T_p represents the pulse's period and it is equal to the time that the vehicle spends on the transmitter track, T_t (equation (3.1)). This is used to represent a moving vehicle across the roadway in the control system simulation.

$$T_p = T_t \tag{3.3}$$

3.1.3. Efficiency

WPT systems are power supplies; as such these are required to provide constant output power with the highest efficiency possible. According to [4], overall power efficiency from the AC power supply, i.e., the grid, to the DC output power of the battery in the vehicle, should be higher than 50%, which includes grid loss and fuel cost, to compete with conventional internal combustion vehicles.

High efficiency in the system can be regarded as less power dissipated. This means that there are not only less loses, but also a simpler cooling system. Consequently, this will lead to a decrease in cost and dimensions due to the reduction of elements.

It can be inferred from equations (2.12) and (2.31) that the efficiency of a system depends on load impedance and coupling coefficient, which are both variables of the system. In a dynamic

34

scenario, the coupling coefficient would be continually changing as a result of existing vertical and horizontal misalignment of the vehicle and the roadway due to driving patterns. Furthermore, battery load changes smoothly during the charge-discharge process [61]. Controllers should be able to adjust the reference value to optimise conditions at all times.

3.1.4. High Power

High switching frequencies and large inductances result in high voltage stress in components. Voltage should not overwhelm the insulation levels of wires, capacitors and electronic devices. The use of a capacitor bank, an array of series capacitors, has been proposed in reference [42] to split voltage stress. The LCC compensation topology also reduces voltage stress in system components.

3.2. Control Strategies

A great advantage of doubled-sided LCC and SS CT is that a DWPTS with these topologies performs as a constant current source. Therefore, output voltage is the main variable requiring control. To control output voltage, several methodologies may be applied. Four closed loop control strategies are reported in reference [62]. These are lower side frequency control (LFC), higher side frequency control (HFC), pre-regulation and post-regulation.

The first two schemes are frequency control strategies. By analysing the frequency response for a system, there are two maximum values of voltage. While lower side frequency control increases the voltage by changing the frequency in the range of zero to the frequency that results in the first peak voltage value, higher side frequency control decreases the voltage by changing the frequency from the frequency that results in the first peak voltage value to a higher frequency. Both strategies consists in regulating the output voltage to the desired value by tuning the frequency. Examples of frequency control are shown in several systems in the literature review. An adaptive frequency and power-level tracking system was designed in reference [58] for a 88 W WPTS and the achieved efficiency was more than 75% at 0.6 meters. Moreover, it monitored the output by wireless communication and adjusted the operating frequency. This approach has been employed by the ORNL research group due to the adoption of series-parallel CT in their designs [59]. Regarding maximum power efficiency tracking, variable frequency control strategies are used in compensation topologies where resonance frequency changes with load and coupling coefficient variations such as parallel compensation to track optimal conditions.

The third and fourth schemes works at fixed operating frequency. Pre-regulation is made on the primary side. This entails modifying the voltage to a suitable level on the transmitter to achieve the desired output voltage. This can be accomplished by either using phase-shift control at the inverter switches or by adding an extra DC-DC converter. A primary side dual-loop controller has been previously proposed for a 25 kW DWPTS for an electric bus [63]. The inner loop follows the current reference while the outer loop limits the power delivery. The controller modifies the switching function by changing the phase-shift angle of the inverter. This causes a variation of width of the square pulses controlling the output of the inverter. Transfer functions are modelled based on generalised state space averaging (GSSA). This results in an accurate analytical modelling of the system. Moreover, this method offers a stable and fast response from off to on state. The disadvantages include the large number of components as a result of several transmitters being placed along the road and the need of receiver–transmitter communication to get output data. A primary side only controller has previously been suggested [64]. This consists of a DC-DC converter, placed before the inversion stage, which uses a pulse width modulation (PWM) method to keep either the voltage or the current in the load constant. A proportional-integral (PI) controller is added for smoothing the response. No communication systems are required owing to the estimation of voltage and current of the secondary side with primary side parameters.

Alternatively, post-regulation may be applied on the secondary side. This controls the reflected load to the system and provides the desired output voltage by changing the duty cycle of a DC-DC converter. A secondary side only controller has been previously designed for a low power SS system [65]. The controller calculates the MPTE conditions and adjusts the voltage on the secondary side. No communication transmitter-receiver is required because of the estimation of parameters from the primary side. However, the overall efficiency of the Hori *et. al.* system is 70%, which is low compared with other methodologies.

3.3. Proposed Strategy

The strategy adopted in this project is based on the post-regulation scheme as presented in Figure 15. The control of the system will focus on reaching MPTE while controlling only the receiver's reference values on-board the vehicle. The secondary control scheme fixes parameters in the transmitter track and modifies the system response via regulation of the secondary voltage. It is noted from section 2.3.3 that the MPTE conditions depend on the fixed primary voltage, known element values of the system and the variable coupling coefficient.

Generally, this last variable is calculated based on the measurement of current and voltage from the primary and secondary pads. In addition, a communication system for transmitting data is required. An alternative approach is to estimate the coupling coefficient using only data from either transmitter or receiver. The estimation of coupling coefficient through secondary parameters is used in this project. This was done to avoid complicating the system and reduce cost by reducing elements.

3.3.1. Estimation of coupling coefficient, k

The estimation of k in the SS system can be calculated as per reference [65]. This is given as

$$k_{est\_ss}(t) = \frac{V_1 + \sqrt{V_1^2 - 4R_1 i_{2\_ss}(t)\left(v_{2\_ss}(t) + R_2 i_{2\_ss}(t)\right)}}{\left(2\omega_0\sqrt{L_1 L_2}\right) i_{2\_ss}(t)} \tag{3.4}$$

In this thesis, the estimation of the coupling coefficient in a double-sided LCC system is introduced. It is derived from equations (2.18) and (2.29) considering the input voltage to be constant, V_1, and the variables $v_{2_{lcc}}$, $i_{2_{lcc}}$ and k as functions of time. This is given as

$$v_{2_{lcc}}(t) = R_{eq} i_{2_{lcc}}(t) \tag{3.5}$$

$$\frac{v_{2_{lcc}}(t)}{V_1} = \frac{k(t)\sqrt{L_1 L_2} R_{eq}}{\omega_0 L_{s1} L_{s2} \left(\frac{R_2 R_{eq} C_{p2}}{L_{s2}} + 1\right)} \tag{3.6}$$

Then, equation (3.5) is solved for R_{eq} and substituted in (3.6) as follows

$$\frac{v_{2_{lcc}}(t)}{V_1} = \frac{\frac{k(t)\sqrt{L_1 L_2} v_{2_{lcc}}(t)}{i_{2_{lcc}}(t)}}{\omega_0 L_{s1} L_{s2} \left(\frac{R_2 C_{p2} v_{2\_lcc}(t)}{L_{s2} i_{2_{lcc}}(t)} + 1\right)} \tag{3.7}$$

Finally, the equation to estimate the coupling coeficient of a double-sided compensated system, k_{est_lcc}, is derived by solving equation (3.7) for $k(t)$.

$$k_{est\_lcc} = \frac{\omega_0 L_{s1} L_{s2} i_{2\_lcc}(t)\left(\frac{R_2 C_{p2} v_{2\_lcc}(t)}{L_{s2} i_{2\_lcc}(t)} + 1\right)}{V_1 \sqrt{L_1 L_2}} \tag{3.8}$$

It is important to note that k_{est_lcc} in equation (3.8) is determined by the real-time measurements of the receiver output voltage and current, $v_{2\_lcc}(t)$ and $i_{2\_lcc}(t)$ and constant values selected on the design stage of the system. A low-pass filter will be added at the output of the estimation block for removing unwanted high-frequency noise in the measured data. A cut-off frequency of 2 kHz has been selected.

3.3.2. Controller Circuit

The circuitry of the secondary controller is composed of an AC-DC converter and a DC-DC converter on the receiver side following the compensation network in power flow direction, as indicated in Figure 15 (a). The AC-DC converter is a single-phase full wave rectifier represented by diodes D_1-D_4.
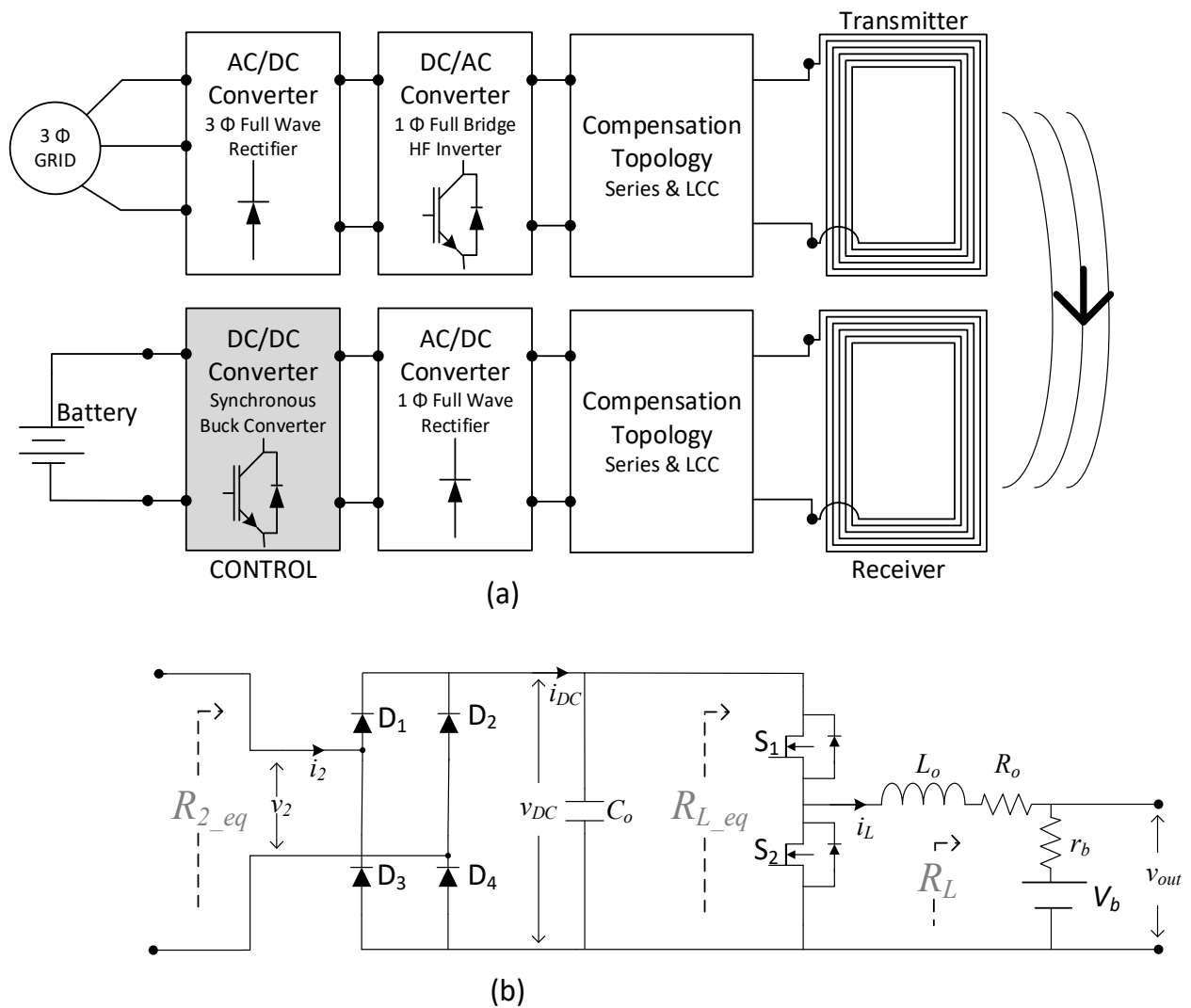

(a)

(b)

Figure 15. (a) System configuration for proposed strategy (b) AC-DC converter& DC-DC converter circuit

The rectification and regulation circuits are illustrated in Figure 15 (b). As can be seen from this figure, the load is a battery. The battery model adopted in this work is the internal resistance model because of its simplicity. It consists in a resistance and a constant DC voltage source. The internal resistance of the battery, r_b, is connected in series with a DC voltage source, V_b. It is likewise noted that the output of the DWPTS is the input of the rectifier. Then, the output of the rectifier is the input of the DC-DC converter. Finally, the DC-DC converter is connected to the load. This is called cascade configuration.

A model that describes the changes of current and voltage from the previous cascade configuration is needed in order to complete the model of the system. According to [51], equation (3.9) describes the relation between the resistance of the DWPTS and the full bridge rectifier.

$$R_{2\_eq} = \frac{8}{\pi^2} R_{L\_eq} \tag{3.9}$$

Where R_{2_eq} is the equivalent load on the DWPTS for a resistance load, $R_{L_{eq}}$, on the rectifier. Then, to reduce the ripple voltage, a capacitor, C_0, is added in the output of the rectifier. Hence, by assuming that $V_{DC} \approx V_{2\_RMS}$ and applying the Ohm's law, I_{DC} is given by

$$I_{DC} = \frac{\pi^2}{8} I_{2\_RMS} \tag{3.10}$$

In these equation, subscript DC refers to the DC components of the output signals of the rectifier. V_{DC} denotes the output voltage while I_{DC} is the output current. The DC component is similarly known as the average value of a signal. The variables V_{2_RMS} and I_{2_RMS} are the root square mean values of the output voltage and current of the compensation network of the receiver in the DWPTS.

The next stage in the cascade configuration is the regulation stage. A DC-DC converter varies the voltage or current to desired levels. Then, the question is "Which DC-DC converter is more appropriate to use in the system?". The DC-DC converter selected for the DWPTS developed in this master project is the synchronous buck converter. This has been chosen for two reasons. First, the battery to be charged is a 330 V battery as shown in TABLE 3. MPTE conditions, shown in Figure 11 (a) and (c), and Figure 12 (a) and (c), indicate that the optimal secondary voltage of the DWPTS is higher than the battery's voltage for the range of k from 0.18 to 3.2. Hence, a buck converter is necessary to step down the voltage. Second, a synchronous buck

converter in the presence of a large current generates lower losses that the asynchronous buck converter because of the replacement of diode by a MOSFET or IGBT.

3.3.2.1.   Synchronous Buck Converter Control

The synchronous buck converter (Figure 16) is a step-down converter that synchronously turns on and off its upper switch, S_1, and lower switch, S_2. In other words, S_1 is in the on state when S_2 is in the off-state. A protection circuit should be implemented to guarantee that S_1 and S_2 do not switch on at the same time.
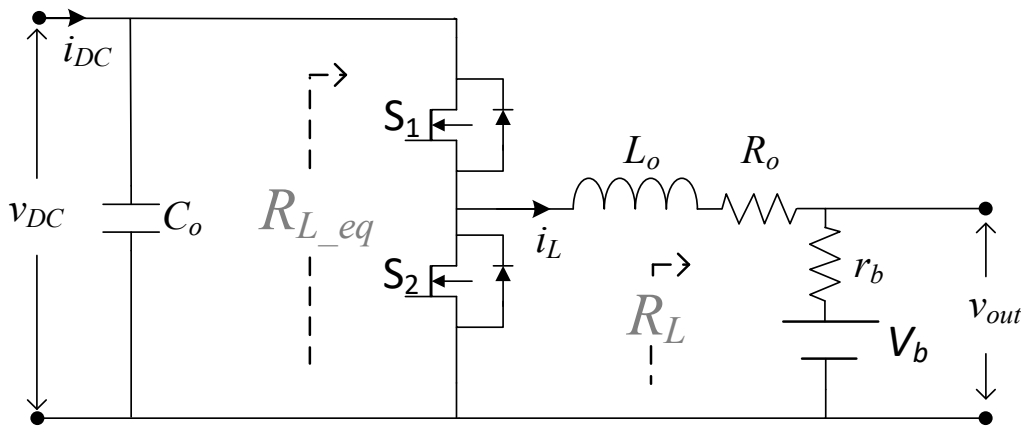

Figure 16. Circuit of a synchronous buck converter

In Figure 16, C_0 is a DC link capacitor. It is where the output the rectification stage and de DC-DC converter get connected. The voltage of this capacitor, $v_{DC}(t)$, is the input voltage of the synchronous buck converter. The current that flows across the load is denoted by $i_L(t)$. R_o is the AC resistance of the inductor L_0 and it was selected to be 200 ohms.

Based on [66], buck converter inductor and capacitor values are calculated as follows

$$L_0 = \frac{V_{oc}(V_{ic} - V_{oc})}{\Delta I_{oc} f_c V_{ic}} \tag{3.11}$$

$$C_0 = \frac{\Delta I_{oc}}{8 f_c \Delta V_{oc}} \tag{3.12}$$

Where,

V_{ci} = Input voltage of the buck converter

V_{co} = Output voltage of the buck converter

f_c = Switching frequency of the buck converter

ΔI_{co} = Output current ripple

ΔV_{DC} = DC link voltage ripple

TABLE 5 shows the selected parameters to calculate the value of the elements of the buck converter. From Figure 11 and Figure 12, V_{ci} is set to 375 V because the optimal output voltage oscillates from 370 to 380 V. V_{co} equals the voltage of the battery. A small variation of 1.2 V is selected as ΔV_{co} because the optimal efficiency depends on the accuracy of the DC link voltage. ΔI_{co} is arbitrarily chosen to be 4.5 A. Finally, f_c is selected to be fourfold lower than f_0.

TABLE 5. PARAMETERS FOR BUCK CONVERTER ELEMENTS VALUES CALCULATION

Parameter	Value
V_{ci} (**V**)	375
V_{co} (**V**)	330
ΔI_{co} (**A**)	4.5
ΔV_{co} (**V**)	1.2
f_c (**kHz**)	20

Evaluating equation (3.11) and (3.12) with values on TABLE 5, this gives

$$L_0 = \frac{330(375 - 330)}{(4.5)(20000)(375)} = 351 \mu H \tag{3.13}$$

$$C_0 = \frac{3}{(8)(20000)(1.2)} = 15 \mu F \tag{3.14}$$

TABLE 6. VALUES OF ELEMENTS OF THE SYNCHRONOUS BUCK CONVERTER

Parameter	Value
C_0 (**μF**)	15
L_0 (**μH**)	360
R_0 (**$m\Omega$**)	200

The values of the passive elements of the buck converter are listed in TABLE 6. Pulse width modulation (PWM) method is used to control the converter output voltage, V_{out}. Hence, the equations that define a synchronous buck converter [66] are as follows

$$V_{out} = D V_{DC} \tag{3.15}$$

$$I_L = \frac{I_{DC}}{D} \tag{3.16}$$

Where D refers to the duty cycle of the upper switch of the synchronous buck converter, S_1. This represents the ratio of the active time period of the converter and the total working period. Its range is from 0 (inactive during the working period) to 1 (active during the whole working period). V_{out} equals the DC source voltage plus the voltage drop in the internal resistance of the battery as shown in

$$V_{out} = V_b + r_b I_L \qquad (3.17)$$

Substituting equations (3.15) and (3.16) into (3.17) and solving for V_{DC}, this gives

$$V_{DC} = \frac{DV_b + r_b I_{DC}}{D^2} \qquad (3.18)$$

Equation (3.19) is used for simplification and represents the output resistance.

$$R_{out} = R_o + r_b \qquad (3.19)$$

The synchronous buck converter has two working states that are called modes. These modes refers to the current state of the switches. When S_1 is on and S_2 is off., the converter is in mode 1 as in Figure 17. When S_1 is off and S_2 is on, the converter is in mode 2 as in Figure 18.
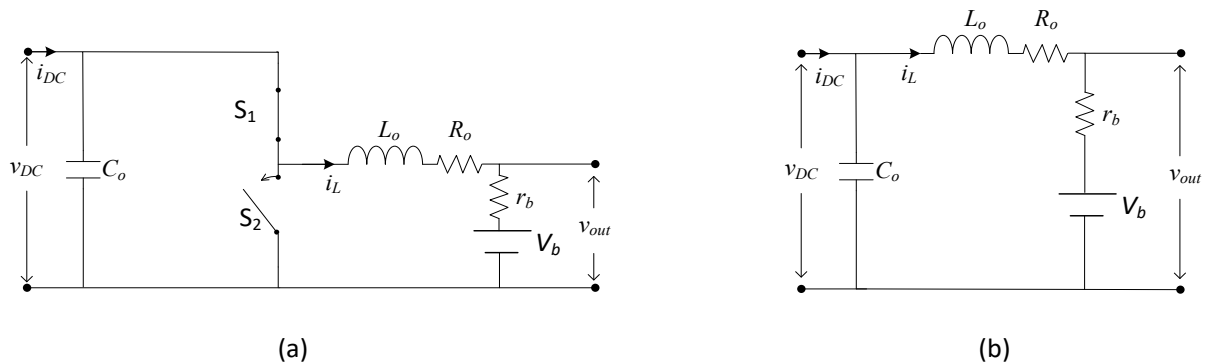

Figure 17. (a) Mode 1 of synchronous buck converter. S_1 is on and S_2 is off (b) Equivalent circuit of Mode 1
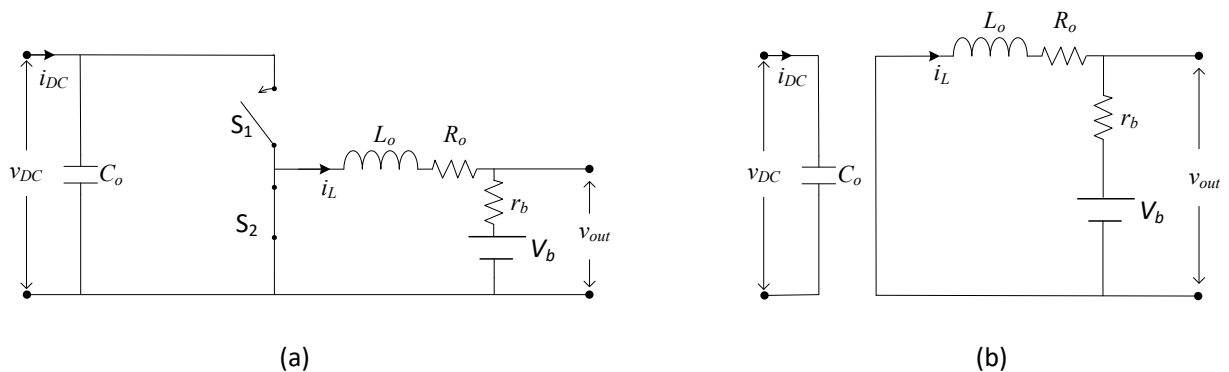

Figure 18. (a) Mode 2 of synchronous buck converter. S_1 is off and S_2 is on (b) Equivalent circuit of Mode 2

There is an equivalent circuit for each mode as shown in Figure 17 (b) and Figure 18 (b). Thus, a model of the synchronous buck converter can be derived from these circuits.

Applying Kirchhoff's law to equivalent circuit of mode 1, the voltage and current equations of this mode are derived as

$$L_0 \frac{di_{L1}(t)}{dt} = (v_{DC}(t) - V_b - R_{out}i_L(t))d(t) \tag{3.20}$$

$$C_0 \frac{dv_{DC1}(t)}{dt} = (i_{DC}(t) - i_L(t))d(t) \tag{3.21}$$

The factor $d(t)$ refers to the function of the duty cycle in terms of time. It multiplies the terms in equations (3.20) and (3.21) to denote that they are only valid when the switch is on.

Applying the same methodology to mode 2 (Figure 18(b)) presents with

$$L_0 \frac{di_{L2}(t)}{dt} = (-V_b - R_{out}i_L(t))\big(1 - d(t)\big) \tag{3.22}$$

$$C_0 \frac{dv_{DC2}(t)}{dt} = i_{DC}(t)\big(1 - d(t)\big) \tag{3.23}$$

Now, the factor $\big(1 - d(t)\big)$ is the complement of the duty cycle and refers to the inactive time of the switch described in mode 2.

Superposition of the equations for each mode provides the model that describes the behaviour of the converter. By adding (3.20) and (3.22) as well as (3.21) and (3.23), this gives

$$L_0 \frac{di_L(t)}{dt} = v_{DC}(t)d(t) - V_b - R_{out}i_L(t) \tag{3.24}$$

$$C_0 \frac{dv_{DC}(t)}{dt} = i_{DC}(t) - i_L(t)d(t) \tag{3.25}$$

Equations (3.24) and (3.25) reveal that the system is nonlinear. This is because of the multiplication of time-varying quantities such as $v_{DC}(t)d(t)$ and $i_L(t)d(t)$. Consequently, Laplace transform cannot be used for calculating the transfer function to model the control system.

To linearise the DC-DC converter for control purposes, averaged AC modelling will be used. This allows for the modelling of low frequency variations of the system while neglecting high

order switching harmonics. The output voltage of a DC-DC converter is a nonlinear function of the duty cycle. Construction of a small signal model allows for calculation of the resulting variations of output voltage from the small variations in the duty cycle at a specific point. This point is named the quiescent point and denotes the steady state of the signal. It is achieved by finding the slope of the curve at the steady-state point and then, calculating its gain. In other words, due to the removal of nonlinear components of the model, it is possible to obtain the transfer functions of the system. To apply averaging, it is important to explain its notation. The average value of a function is denoted as

$$\langle f(t) \rangle_{T_s} = \frac{1}{T_a} \int_{t-\frac{T_a}{2}}^{t+\frac{T_a}{2}} f(\tau)d\tau \tag{3.26}$$

Where, T_a represents the period of the function and t is the time of averaging. Even for derivatives, averaged equations can be applied. Let $g(t)$ be the derivative of the function $f(t)$.

$$\frac{df(t)}{dt} = g(t) \tag{3.27}$$

The derivate of the $f(t)$ applying averaging as in equation (3.26) results in

$$\frac{d\langle f(t) \rangle_{T_a}}{dt} = \frac{d}{dt}\left(\frac{1}{T_a} \int_{t-\frac{T_a}{2}}^{t+\frac{T_a}{2}} f(\tau)d\tau \right) \tag{3.28}$$

It is possible to interchange the order of integration and differentiation if the function is continuous and its derivative has finite number of discontinuities. Thus, equation (3.28) can be represented as

$$\frac{d\langle f(t) \rangle_{T_a}}{dt} = \frac{1}{T_s} \int_{t-\frac{T_a}{2}}^{t+\frac{T_a}{2}} \frac{df(\tau)}{d\tau}d\tau \tag{3.29}$$

By substituting (3.27) in (3.29), the resulting equation is

$$\frac{d\langle f(t) \rangle_{T_a}}{dt} = \frac{1}{T_s} \int_{t-\frac{T_a}{2}}^{t+\frac{T_a}{2}} g(\tau)d\tau \tag{3.30}$$

The right-hand side of the equation (3.30) represents the average value of $g(t)$. Thus

$$\frac{d\langle f(t)\rangle_{T_a}}{dt} = \langle g(t)\rangle_{T_a} \tag{3.31}$$

Equation (3.31) proves that averaging may be used for first order differential equations under the stated conditions. Analysing the synchronous buck converter model, both equations fulfil these conditions. The inductor current, $i_L(t)$, and its derivative are continuous functions. In a similar way, capacitor voltage, $v_{DC}(t)$, and its derivative meet these conditions. Thus, the average model for the synchronous buck converter results in

$$L_0 \frac{d\langle i_L(t)\rangle_{T_a}}{dt} = \langle v_{DC}(t)\rangle_{T_a} d(t) - V_b - R_{out}\langle i_L(t)\rangle_{T_a} \tag{3.32}$$

$$C_0 \frac{d\langle v_{DC}(t)\rangle_{T_s}}{dt} = \langle i_{DC}(t)\rangle_{T_s} - \langle i_L(t)\rangle_{T_s} d(t) \tag{3.33}$$

If the converter works at a particular operating point, it can be assumed that the average value of the variables equals a DC constant plus a small variation, given as

$$\langle f(t)\rangle_{T_s} = F + \hat{f}(t) \tag{3.34}$$

The components of a small signal model are represented below. For the DC constant component, or steady state value, each variable is denoted with an uppercase letter. Additionally, the small AC variation is denoted by a lowercase letter and hat as in equation (3.34). Applying this assumption to the variables of the model gives

$$\langle v_{DC}(t)\rangle_{T_s} = V_{DC} + \hat{v}_{DC}(t) \tag{3.35}$$

$$d(t) = D + \hat{d}(t) \tag{3.36}$$

$$\langle i_L(t)\rangle_{T_s} = I_L + \hat{i}_L(t) \tag{3.37}$$

$$\langle i_{DC}(t)\rangle_{T_s} = I_{DC} + \hat{i}_{DC}(t) \tag{3.38}$$

The next assumption introduces is that the DC component is much larger than the perturbations. This is known as small signal assumption and can be presented as shown in equations (3.39) to (3.42).

$$|V_{DC}| >> |\hat{v}_{DC}(t)| \tag{3.39}$$

$$|D| >> |\hat{d}(t)| \tag{3.40}$$

$$|I_L| \gg |\hat{\imath}_L(t)| \tag{3.41}$$

$$|I_{DC}| \gg |\hat{\imath}_{DC}(t)| \tag{3.42}$$

Applying the assumptions discussed beforehand to equations (3.32) and (3.33), a small signal model can be obtained as

$$L_0 \frac{d\big(I_L + \hat{\imath}_L(t)\big)}{dt} = \big(V_{DC} + \hat{v}_{DC}(t)\big)\big(D + \hat{d}(t)\big) - V_b$$
$$-R_{out}(I_L + \hat{\imath}_L(t)) \tag{3.43}$$

$$C_0 \frac{d\big(V_{DC} + \hat{v}_{DC}(t)\big)}{dt} = (I_{DC} + \hat{\imath}_{DC}(t)) - (I_L + \hat{\imath}_L(t))\big(D + \hat{d}(t)\big) \tag{3.44}$$

According to the constant rule. For any constant c, if $f(t) = c$, then $\frac{d(c)}{dt} = 0$. Simplifying equation (3.43), differentiation of the constant I_L is zero and it results in

$$\underbrace{0}_{DC} + \underbrace{L_0 \frac{d(\hat{\imath}_L(t))}{dt}}_{\substack{Average \\ 1^{st}\ order}} = \underbrace{(V_{DC}D - R_{out}I_L - V_b)}_{DC} + \underbrace{\Big(V_{DC}\hat{d}(t) + D\hat{v}_{DC}(t) - R_{out}\hat{\imath}_L(t)\Big)}_{Average\ 1^{st}\ order}$$
$$\underbrace{+\hat{v}_{DC}(t)\hat{d}(t)}_{Average\ 2^{nd}\ order} \tag{3.45}$$

Equating DC and average terms on both sides of equation (3.45) as shown in (3.46), first, DC components equals 0 zero due to the absence of zero DC terms on the left-hand side. Then, average first order term on the left-hand side equals the average first order and second order terms on the right-hand side. Due to the small signal assumption, second order terms can be neglected. This is because the product of two small signals is smaller than one. Additionally, the first order terms are much greater than the second order values.

$$0 = (V_{DC}D - R_{out}I_L - V_b)$$

$$L_0 \frac{d\big(\hat{\imath}_L(t)\big)}{dt} = V_{DC}\hat{d}(t) + D\hat{v}_{DC}(t) - R_{out}\hat{\imath}_L(t) + \hat{v}_{DC}(t)\hat{d}(t) \tag{3.46}$$

Thus, only first order terms are retained. This gives

$$L_0 \frac{d\big(\hat{\imath}_L(t)\big)}{dt} = V_{DC}\hat{d}(t) + D\hat{v}_{DC}(t) - R_{out}\hat{\imath}_L(t) \tag{3.47}$$

46

Applying the same procedure to equation (3.44), the differentiation of the constant V_{DC} is zero. Thus, the small signal model is simplified as in

$$\underbrace{0}_{DC} + \underbrace{C_0 \frac{d(\hat{v}_{DC}(t))}{dt}}_{\substack{Average \\ 1^{st}\ order}} = \underbrace{(I_{DC} - I_L D)}_{DC} + \underbrace{\left(\hat{\imath}_{DC}(t) - I_L \hat{d}(t) - D\hat{\imath}_L(t)\right)}_{1^{st}\ order}$$
$$+ \underbrace{\hat{\imath}_L(t)\hat{d}(t)}_{2^{nd}\ order} \tag{3.48}$$

Equating DC and average terms on both sides of equation (3.48) as shown in (3.49), same criteria is applied as in (3.47).

$$0 = (I_{DC} - I_L D)$$

$$C_0 \frac{d(\hat{v}_{DC}(t))}{dt} = \hat{\imath}_{DC}(t) - I_L \hat{d}(t) - D\hat{\imath}_L(t) + \hat{\imath}_L(t)\hat{d}(t) \tag{3.49}$$

Again, only first order terms are retained. Such that the averaged AC signal model for the converter is described in equations (3.47) and (3.50).

$$C_0 \frac{d(\hat{v}_{DC}(t))}{dt} = \hat{\imath}_{DC}(t) - I_L \hat{d}(t) - D\hat{\imath}_L(t) \tag{3.50}$$

The averaged AC signal model can be represented in state space. The state variables are the smallest set of variables that describe a system's dynamics. The number of state variables is given by the order of the system. From the previous model with two first order differential equations, the number of state variables as defined is two. The chosen variables for this representation are the current through the battery, $\hat{\imath}_L(t)$, and the voltage of the capacitor, $\hat{v}_{DC}(t)$. This is because the converter model describes the dynamics. Thus, the state-space representation results are as follows

$$K \frac{d}{dt}\hat{x}(t) = \hat{A}\hat{x}(t) + \hat{B}\hat{u}(t) \tag{3.51}$$

$$\hat{y}(t) = \hat{C}\hat{x}(t) \tag{3.52}$$

Where vector $\hat{x}(t)$ contains the state variables of the system. Our input vector, $\hat{u}(t)$, is defined by two variables. The first variable is the variation of duty cycle, $\hat{d}(t)$, and the second is the

variation of DWPTS's average output current, $\hat{\imath}_{DC}(t)$. Matrix $\hat{A}$, $\hat{B}$ and $\hat{C}$ are the state matrix, input matrix and output matrix, which can be represented from equations (3.47) and (3.50) as

$$K = \begin{bmatrix} L_0 & 0 \\ 0 & C_0 \end{bmatrix} \tag{3.53}$$

$$\hat{x}(t) = \begin{bmatrix} \hat{\imath}_L(t) \\ \hat{v}_{DC}(t) \end{bmatrix} \tag{3.54}$$

$$\hat{u}(t) = \begin{bmatrix} \hat{d}(t) \\ \hat{\imath}_{DC}(t) \end{bmatrix} \tag{3.55}$$

$$\hat{y} = \hat{v}_{DC}(t) \tag{3.56}$$

$$\hat{A} = \begin{bmatrix} -R_{out} & D \\ -D & 0 \end{bmatrix} \quad \hat{B} = \begin{bmatrix} V_{DC} & 0 \\ -I_L & 1 \end{bmatrix} \tag{3.57}$$

$$\hat{C} = \begin{bmatrix} 0 & 1 \end{bmatrix}$$

The behaviour of $\hat{\imath}_{DC}(t)$ relies on the dynamics of the DWPTS. Thus, it will vary with the topology of each system. Furthermore, to simplify our control system complexity, $\hat{\imath}_{DC}(t)$ can be expressed in terms of $\hat{v}_{DC}(t)$, further reducing the number of input variables in the system. The transfer function for each compensation topology is derived in the next section.
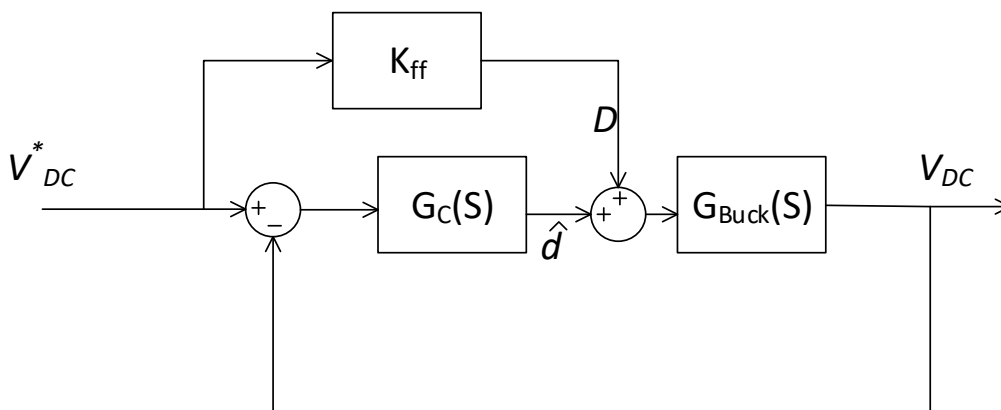

Figure 19. Proposed closed-loop for voltage control

The closed-loop control system is shown in Figure 19. This architecture is chosen due to the fact that the controller must follow a reference that lead to optimal conditions. This is accomplished by calculating the error through the feedback and adding a proportion of it to the desired duty cycle to compensate the error and modify the transient response. K_{ff} is the feed-forward

48

gain that sets the required duty cycle that is estimated depending on the desired DC voltage. In other words, K_{ff} represents the relation between the two parameters of the quiescent point (V_{DC}^*, D). This is given by the constant duty cycle equation of the system that will be derived in sections 3.3.3 and 3.3.4. $G_C(s)$ and $G_{Buck}(s)$ represent the controller and plant of the system, which are similarly further detailed in later sections.

3.3.3. Series-series system control

To finish the model of the series-series system, it is required the calculation of the dynamics of $\hat{\imath}_{DC}(t)$ with respect to $\hat{v}_{DC}(t)$. First, the variables v_{2_ss} and i_{2_ss} are considered as functions of time. Then, by solving (2.7) for R_{eq} and substituting the result in (2.10), this gives solved for $i_{2\_ss}(t)$ as follows

$$i_{2\_ss}(t) = \frac{\omega_0 k\sqrt{L_1 L_2}v_1(t) - R_1 v_{2\_ss}(t)}{R_1 R_2 + \left(\omega_0 k\sqrt{L_1 L_2}\right)^2} \tag{3.58}$$

The partial derivative of $i_{2\_ss}(t)$ with respect to $v_{2\_ss}(t)$ is then calculated.

$$\frac{\partial i_{2\_ss}(t)}{\partial v_{2\_ss}(t)} = -\frac{R_1}{R_1 R_2 + \left(\omega_0 k\sqrt{L_1 L_2}\right)^2} \tag{3.59}$$

Solving for $\partial i_{2\_ss}(t)$, this gives

$$\partial i_{2\_ss}(t) = -\frac{R_1}{R_1 R_2 + \left(\omega_0 k\sqrt{L_1 L_2}\right)^2} \partial v_{2\_ss}(t) \tag{3.60}$$

Then, it is assumed that $v_{DC\_ss} \approx v_{2\_ss\_RMS}$. Then, substituting (3.10) into (3.60), and solving for $\partial i_{DC\_ss}(t)$, average values can be calculated as

$$\partial i_{DC\_ss}(t) = -\frac{8}{\pi^2}\frac{R_1}{R_1 R_2 + \left(\omega_0 k\sqrt{L_1 L_2}\right)^2} \partial v_{DC\_ss}(t) \tag{3.61}$$

Applying small change approximation, $\partial i_{DC\_ss}(t)$, which describes a small variation of $i_{DC\_ss}(t)$, can be set equal to $\hat{\imath}_{DC\_ss}(t)$. The same approach is applied to $\partial v_{DC\_ss}(t)$.

$$\hat{\imath}_{DC\_ss}(t) = -\frac{8}{\pi^2}\frac{R_1}{R_1 R_2 + \left(\omega_0 k\sqrt{L_1 L_2}\right)^2} \hat{v}_{DC\_ss}(t) \tag{3.62}$$

The state space representation of an SS control systems can be determined by substituting equation (3.62) into equation (3.50), which results in

$$K_{ss} = \begin{bmatrix} L_0 & 0 \\ 0 & C_0 \end{bmatrix} \tag{3.63}$$

$$\hat{x}_{ss}(t) = \begin{bmatrix} \hat{i}_{L\_ss}(t) \\ \hat{v}_{DC\_ss}(t) \end{bmatrix} \tag{3.64}$$

$$\hat{u}_{ss}(t) = \hat{d}_{ss}(t) \tag{3.65}$$

$$\hat{y}_{ss}(t) = \hat{v}_{DC\_ss}(t) \tag{3.66}$$

$$\hat{A}_{SS} = \begin{bmatrix} -R_{out} & D_{ss} \\ -D_{ss} & -\dfrac{8}{\pi^2} \dfrac{R_1}{R_1 R_2 + (\omega_0 M)^2} \end{bmatrix} \quad \hat{B}_{SS} = \begin{bmatrix} V_{DC\_ss} \\ -I_{L\_ss} \end{bmatrix} \tag{3.67}$$

$$\hat{C}_{SS} = \begin{bmatrix} 0 & 1 \end{bmatrix}$$

Once the state space has been described, it can be noted that matrices $\hat{A}_{SS}$ and $\hat{B}_{SS}$ depend only on constant parameters of the system and the quiescent point (V_{DC_ss}, D_{ss}).

For the quiescent point calculation, V_{DC_ss} is set to be the reference value of the system. Depending on its maximum efficiency conditions, which have been defined in the previous chapter, the desired constant voltage output is selected.

$$V_{DC\_ss}^* = V_{2\_ss\_\eta MAX\_RMS} \tag{3.68}$$

$$V_{DC\_ss} = V_{DC\_ss}^* \tag{3.69}$$

The duty cycle can be derived from equation (3.18) by substituting (3.69) and solving for D as

$$D_{ss} = \frac{V_b + \sqrt{V_b^2 + 4r_b V_{DC\_ss}^* I_{DC\_ss}}}{2V_{DC\_ss}^*} \tag{3.70}$$

By assuming that $v_{DC\_ss} \approx v_{2\_ss\_RMS}$ and substituting (3.10) and (3.69) into equation (3.58), I_{DC_ss} is obtained as

$$I_{DC\_ss} = \frac{8}{\pi^2} \frac{\omega_0 M V_{1\_RMS} - R_1 V_{DC\_ss}^*}{R_1 R_2 + (\omega_0 M)^2} \tag{3.71}$$

50

And I_{L_ss} has been previously described in equation (3.16).

$$I_{L\_ss} = \frac{I_{DC\_ss}}{D_{ss}} \tag{3.72}$$

3.3.4. Double-sided LCC system control

Derivation of $\hat{\imath}_{DC\_lcc}(t)$ is done in this section for the double-sided LCC system. By solving (3.5) for R_{eq} and substituting the result in (2.29), this gives solved for $i_{2\_lcc}(t)$ as follows

$$i_{2\_lcc}(t) = -\frac{k\sqrt{L_1 L_2} v_1(t)\left(\frac{\omega_0 C_{p2} L_{s1} R_2 v_{2\_lcc}(t)}{k\sqrt{L_1 L_2} v_1(t)} - 1\right)}{\omega_0 L_{s1} L_{s2}} \tag{3.73}$$

The partial derivative of $i_{2\_lcc}(t)$ is derived with respect to $v_{2\_lcc}(t)$. This gives

$$\frac{\partial i_{2\_lcc}(t)}{\partial v_{2\_lcc}(t)} = -\frac{C_{p2} R_2}{L_{s2}} \tag{3.74}$$

Solving (3.74) for $\partial i_{2\_lcc}(t)$ and substituting equations (3.10), $\partial i_{DC\_lcc}(t)$ is found. Then, it is assumed that $v_{DC\_lcc} \approx v_{2\_lcc\_RMS}$. Applying small change approximation, $\partial i_{DC\_lcc}(t)$ and $\partial v_{DC\_lcc}(t)$, which describes a small variation of $i_{DC\_lcc}(t)$ and $v_{DC\_lcc}(t)$, can be set equal to $\hat{\imath}_{DC\_lcc}(t)$ and $\hat{v}_{DC\_lcc}(t)$ as

$$\hat{\imath}_{DC\_lcc}(t) = -\frac{8}{\pi^2}\frac{C_{p2} R_2}{L_{s2}}\hat{v}_{DC\_lcc}(t) \tag{3.75}$$

The space state representation for double-sided compensated systems can be obtained by substituting equation (3.75) in to equation (3.50). This gives

$$K_{lcc} = \begin{bmatrix} L_0 & 0 \\ 0 & C_0 \end{bmatrix} \tag{3.76}$$

$$\hat{x}_{lcc}(t) = \begin{bmatrix} \hat{\imath}_{L\_lcc}(t) \\ \hat{v}_{dc\_lcc}(t) \end{bmatrix} \tag{3.77}$$

$$\hat{u}_{lcc}(t) = \hat{d}_{lcc}(t) \tag{3.78}$$

$$\hat{y}_{lcc}(t) = \hat{v}_{DC\_lcc}(t) \tag{3.79}$$

$$\hat{A}_{lcc} = \begin{bmatrix} -R_{out} & D_{lcc} \\ -D_{lcc} & -\dfrac{8}{\pi^2}\dfrac{C_{p2}R_2}{L_{s2}} \end{bmatrix} \quad \hat{B}_{lcc} = \begin{bmatrix} V_{DC\_lcc} \\ -I_{L\_lcc} \end{bmatrix} \tag{3.80}$$

$$\hat{C}_{lcc} = \begin{bmatrix} 0 & 1 \end{bmatrix}$$

The calculation of quiescent point (V_{DC_lcc}, D_{lcc}) is similar to that for SS CT system.

$$V^*_{DC\_lcc} = V_{2\_lcc\_\eta MAX\_RMS} \tag{3.81}$$

$$V_{DC\_lcc} = V^*_{DC\_lcc} \tag{3.82}$$

In addition, the duty cycle can be derived from equation (3.18) by substituting (3.82) and solving for D as

$$D_{lcc} = \frac{V_b + \sqrt{V_b^2 + 4r_b V^*_{DC\_lcc} I_{DC\_lcc}}}{2V^*_{DC\_lcc}} \tag{3.83}$$

Then, it is assumed again that $v_{DC\_lcc} \approx v_{2\_lcc\_RMS}$. I_{DC_lcc} is obtained by substituting equations (3.10) and (3.81) into equation (3.73), and considering RMS value of the input voltage. This gives

$$I_{DC\_lcc} = -\frac{8}{\pi^2}\frac{MV_{1\_RMS}\left(\dfrac{\omega_0 C_{p2}L_{s1}R_2 V^*_{DC\_lcc}}{MV_{1\_RMS}} - 1\right)}{\omega_0 L_{s1}L_{s2}} \tag{3.84}$$

And I_{L_lcc} is calculated as in equation (3.16).

$$I_{L\_lcc} = \frac{I_{DC\_lcc}}{D_{lcc}} \tag{3.85}$$

3.3.5. Transfer Functions and PID controllers

The relation of input, $\hat{d}(t)$, to output $\hat{v}_{DC}(t)$ is now required. This is determined by calling the transfer function matrix, which converts the state space representation into a transfer function.

$$G(s) = \frac{Y(s)}{U(s)} = C(sI - K^{-1}A)^{-1}K^{-1}B + D \tag{3.86}$$

Derivation of the transfer functions for both systems are be carried out using equation (3.86), where $s = \sigma + j\omega$, the complex variable. The SS compensated system transfer function calculation is given by

$$\frac{\hat{v}_{DC\_ss}(s)}{\hat{d}_{ss}(s)} = \begin{bmatrix} 0 & 1 \end{bmatrix} \begin{bmatrix} s - \left(-\dfrac{R_{out}}{L_0}\right) & -\dfrac{D_{ss}}{L_0} \\ \dfrac{D_{ss}}{C_0} & s - \left(-\dfrac{8}{C_0\pi^2}\dfrac{R_1}{R_1R_2 + (\omega_0 M)^2}\right) \end{bmatrix}^{-1} \begin{bmatrix} \dfrac{V_{DC\_ss}}{L_0} \\ -\dfrac{I_{L\_ss}}{C_0} \end{bmatrix}$$

Thus, the relation $\hat{v}_{DC\_ss}(s)/\hat{d}_{ss}(s)$ is

$$G_{Buck_{ss}}(s) = \frac{\hat{v}_{DC\_ss}(s)}{\hat{d}_{ss}(s)} = \frac{b_{1\_ss}s + b_{0\_ss}}{s^2 + a_{1\_ss}s + a_{0\_ss}} \tag{3.88}$$

Where,

$$b_{0\_ss} = \frac{R_{out}I_{L\_ss} + D_{ss}V_{DC\_ss}}{L_0}$$

$$b_{1\_ss} = -\frac{I_{L\_ss}}{C_0}$$

$$a_{0\_ss} = \frac{D_{ss}^2 + \dfrac{8R_{out}R_1}{\pi^2 R_1 R_2 + (\omega_0 M)^2}}{L_0 C_0}$$

$$a_{1\_ss} = -\frac{R_{out}}{L_0} + \frac{8}{C_0\pi^2}\frac{R_1}{R_1 R_2 + (\omega_0 M)^2}$$

By substituting equations (3.70), (3.71) and (3.72) into the transfer function in equation (3.88) and then, evaluating parameters from TABLE 4 and TABLE 6 results in

$$G_{Buck_{ss}}(s) = \frac{\hat{v}_{DC\_ss}(s)}{\hat{d}_{ss}(s)} = \frac{-7.334x10^5 s - 2.18x10^{10}}{s^2 + 407.7s + 4.852x10^7} \tag{3.89}$$

The same methodology is be used for a double-sided compensated system. Thus,

$$\frac{\hat{v}_{DC\_lcc}(s)}{\hat{d}_{lcc}(s)} = \begin{bmatrix} 0 & 1 \end{bmatrix} \begin{bmatrix} s - \left(-\dfrac{R_{out}}{L_0}\right) & -\dfrac{D_{lcc}}{L_0} \\ \dfrac{D_{lcc}}{C_0} & s - \left(-\dfrac{8}{C_0\pi^2}\dfrac{C_{p2}R_2}{L_{s2}}\right) \end{bmatrix}^{-1} \begin{bmatrix} \dfrac{V_{DC\_lcc}}{L_0} \\ -\dfrac{I_{L\_lcc}}{C_0} \end{bmatrix}$$

$$G_{Buck_{lcc}}(s) = \frac{\hat{v}_{DC\_lcc}(s)}{\hat{d}_{lcc}(s)} = \frac{b_{1\_lcc}s + b_{0\_lcc}}{s^2 + a_{1\_lcc}s + a_{0\_lcc}} \tag{3.90}$$

Where,

$$b_{0\_lcc} = \frac{R_{out}I_{L\_lcc} + D_{lcc}V_{DC\_lcc}}{L_0}$$

$$b_{1\_lcc} = -\frac{I_{L\_lcc}}{C_0}$$

$$a_{0\_lcc} = \frac{D_{lcc}^2 + \frac{8R_{out}C_{p2}R_2}{\pi^2 L_{s2}}}{L_0 C_0}$$

$$a_{1\_lcc} = -\frac{R_{out}}{L_0} + \frac{8}{C_0\pi^2}\frac{C_{p2}R_2}{L_{s2}}$$

By substituting equations (3.83), (3.84) and (3.85) into the transfer function in equation (3.90) and then, evaluating parameters from TABLE 4 and TABLE 6 results in

$$G_{Buck_{lcc}}(s) = \frac{\hat{v}_{DC\_lcc}(s)}{\hat{d}_{lcc}(s)} = \frac{-6.769x10^5 s - 2.176x10^{10}}{s^2 + 406.1s + 4.996x10^7} \tag{3.91}$$

The transfer functions of both systems are shown in equations (3.89) and (3.91). These are second order systems. For the series-series compensated system, two open-loop poles, which are the roots of the denominator of the transfer function, are located at -203.9 + j6962.6 and -203.9 – j6962.6 and one zero, which is the root of the numerator, is found at -2.9723x10⁴. On the other hand, the poles of the double-sided LCC compensated system are located at -203.1 + j7065.4 and -203.1 + j7065.4, while the zero is at -3.2142 x10⁴.

In control systems, the poles play an important role because they determine the stability of the system and the form of the response. By analysing these two characteristics, an appropriate controller can be selected. First, the stability of the system must be determined and it is done in this project by pole location. A linear system is stable if all of its poles lie within the left-half of the s-plane. It is because of the associated time response to the negative poles. The solution to the differential equation can be obtained by multiplying the transfer function, $G(s)$, and the Laplace transform of the input, $R(s)$. Then, it is calculated the inverse Laplace transform of the function.

$$c(t) = \mathcal{L}^{-1}\{R(s)G(s)\} \tag{3.92}$$

Due to the fact that the goal of the controller is to follow a reference of maximum efficiency, the unit step, $R(s) = 1/s$, is taken as test input.

54

$$c_{ss}(t) = 449.3e^{-203.85t}(\cos 6962.6t - 0.01(\sin 6962.6t)) - 449.3 \qquad (3.93)$$

$$c_{lcc}(t) = 435.5e^{-196.9t}(\cos 22343t - 0.2(\sin 22343t)) - 435.5 \qquad (3.94)$$

The sign of the real part of the poles guarantees the stability of the open-loop system because the corresponding time response for a unit step results in an exponential function base e with negative power times an addition of sines and cosines, where the number e refers to the irrational constant which value is 2.71828.

In addition, the time response of a system is the summation of its natural response and force response (3.95).

$$c(t) = c_{natural}(t) + c_{forced}(t) \qquad (3.95)$$

The natural response is determined by the dynamics of the system expressed by the transfer function and the forced response is generated by the input. It means that the natural response of the system has a decay rate determined by the real part of the poles and it will eventually be zero. Then, the forced response of the system is the only kept on the steady sate. Hence, the negative poles guarantee a bounded output if the input is similarly bounded.

Once the stability of the system is proved, open-loop settling time, overshoot percentage and steady state error characteristics are analysed from the transfer function for a unit step input by using the following equations [67].

$$T_s = \frac{4}{\zeta \omega_n} \qquad (3.96)$$

$$OS\% = 100e^{-\left(\frac{\zeta \pi}{\sqrt{1-\zeta^2}}\right)} \qquad (3.97)$$

$$e(\infty) = \lim_{s \to 0} sR(s)[1 - G(s)] \qquad (3.98)$$

Where ω_n denotes the natural frequency of the system which is the oscillation frequency without damping. The damping ratio, ζ, is the ratio between the exponential decay frequency and the natural frequency. The natural frequency and damping ratio of a second order system state the form of the transient response. These quantities are calculated from the characteristic polynomial of the system which is the denominator of its transfer function. Thus, the denominator can be transformed to display ζ and ω_n as follows

$$s^2 + a_1 s + a_0 = s^2 + 2\zeta\omega_n s + \omega_n^2 \tag{3.99}$$

From equation (3.99), ω_n and ζ are derived as

$$\zeta = \frac{a_1}{2\omega_n} \tag{3.100}$$

$$\omega_n = \sqrt{a_0} \tag{3.101}$$

By substituting coefficient values of the denominators of the transfer functions $G_{Buck_{ss}}(s)$ and $G_{Buck_{lcc}}(s)$ in (3.100) and (3.101), settling time and overshoot percentage can be now calculated by (3.96) and (3.97), respectively.

$$T_{s_{ss}} = \frac{4}{(0.0293)(6970)} = 0.0196 \tag{3.102}$$

$$OS\%_{ss} = 100e^{-\left(\frac{0.0293\pi}{\sqrt{1-0.0293^2}}\right)} = 91.02\% \tag{3.103}$$

$$T_{s_{lcc}} = \frac{4}{(0.0279)(7070)} = 0.02\ seconds \tag{3.104}$$

$$OS\%_{lcc} = 100e^{-\left(\frac{0.0279\pi}{\sqrt{1-0.0279^2}}\right)} = 91.6\% \tag{3.105}$$

One can notice from equation (3.102) to (3.105) that both systems have a similar settling time around 0.02 seconds and an overshoot percentage around 91%. Regarding overshoot percentage, it has to be reduced. A 91% overshoot means that the oscillations amplitude almost double the final value. The first design requirement for the project is that overshoot percentage must be at most 10% to avoid high peaks and losses. On the other hand, the requirement for the settling time is set by analysing the moving car and the transmitters. As previously described in section 3.1, an EV moving across the road where several short tracks are buried, will only stay on the chosen track for 0.026 seconds. Thus, the settling time of the controller must be shorter than this period, in order to achieve power delivery. The settling time used was selected to be less than 0.008 seconds.

Another characteristic to be analyse is the steady state error, which is the difference between the desired value and the final value. The steady state errors for the series-series compensated system, $e_{ss}(\infty)$, and double-sided LCC compensated system, $e_{lcc}(\infty)$, are obtained by

evaluating equation (3.98) for $G_{Buck_{ss}}(s)$ and $G_{Buck_{lcc}}(s)$ and considering $R(s) = 1/s$ as follows

$$e_{ss}(\infty) = 1 - \lim_{s\to0} \frac{-7.334x10^5 s - 2.18x10^{10}}{s^2 + 407.7s + 4.852x10^7} = -448.3 \qquad (3.106)$$

$$e_{lcc}(\infty) = 1 - \lim_{s\to0} \frac{-6.769x10^5 s - 2.18x10^{10}}{s^2 + 393.8s + 4.996x10^7} = -436.3 \qquad (3.107)$$

One can establish from $e_{ss}(\infty)$ and $e_{lcc}(\infty)$ that the controller must eliminate the large errors of the systems in order to follow the reference.

In Figure 20, command step from MATLAB is used to illustrate the unit step response to each system. It can be observed that the open-loop system is stable as was inferred above. Similarly, systems have a settling time around 0.019 seconds and an overshoot percentage of 93.4%, which match with the calculations.

Once the control requirements have been set, a controller should be used to adjust the small variations of duty cycle around the quiescent point to meet the desired conditions. A proportional integral controller (PI) eliminates the steady state error by adding a pole at the origin and a zero very close to this pole increasing the order of the system. A proportional differential controller (PD) changes the transient response of the system by adding an extra zero. A proportional integral differential controller (PID) combines the two controllers before mentioned. A PID controller is selected to meet the following design conditions

- $OS\% < 10\%$
- $T_s < 0.008$
- No steady state error

$$G_C(s) = K_P + \frac{K_I}{s} + K_D s \qquad (3.108)$$

Through the design environment SISOTOOL MATLAB, a PID controller is designed for the architecture shown in Figure 19 for each system. By using the command sisotool (*'transfer function'*), it opens an interface where you can select the architecture of the control system and introduce the design requirements. It returns the gains of the desired controller. The gains of the PID controller of the series-series and double-sided system are shown in TABLE 7 and TABLE 8. The resulting step response to the close-loop of the series-series system with a PID controller, which gains are deployed in TABLE 7, is shown in Figure 21.

57

TABLE 7. PID GAINS FOR SS SYSTEM CONTROLLER

Controller Gains	C_{PID_ss}
K_P_ss	-0.00156
K_I_ss	-1.84
K_D_ss	-0.001
τ_D_ss	10

Stability of the system can be inferred from the Figure 21 due to the bounded response. The settling time is 0.00756 seconds and there is no overshoot. Thus the design requirements have been met. Furthermore, there is no steady-state error, which means that the converter is following the reference. Applying the same methodology to the double-sided system, the step response to the close-loop system is shown in Figure 22 using controller gains from TABLE 8.

(a)

(b)
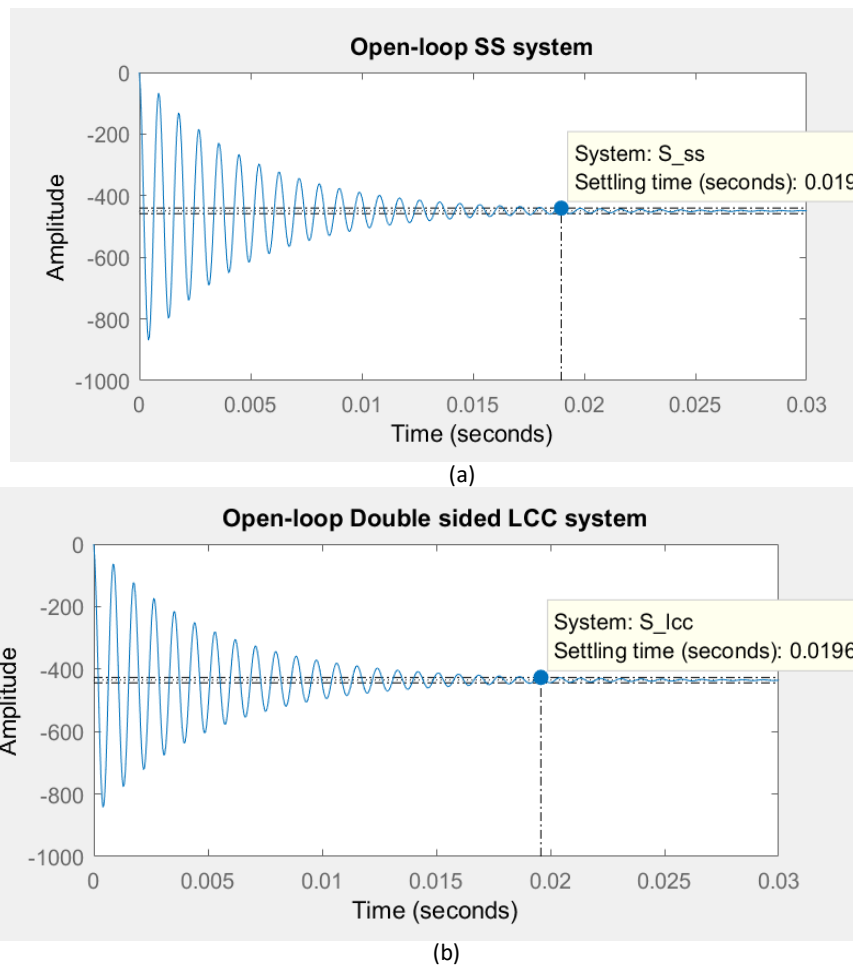
Figure 20. Open-loop response to step input. a) SS CT system b) LCC CT system

TABLE 8. PID GAINS FOR DOUBLE-SIDED LCC SYSTEM CONTROLLER

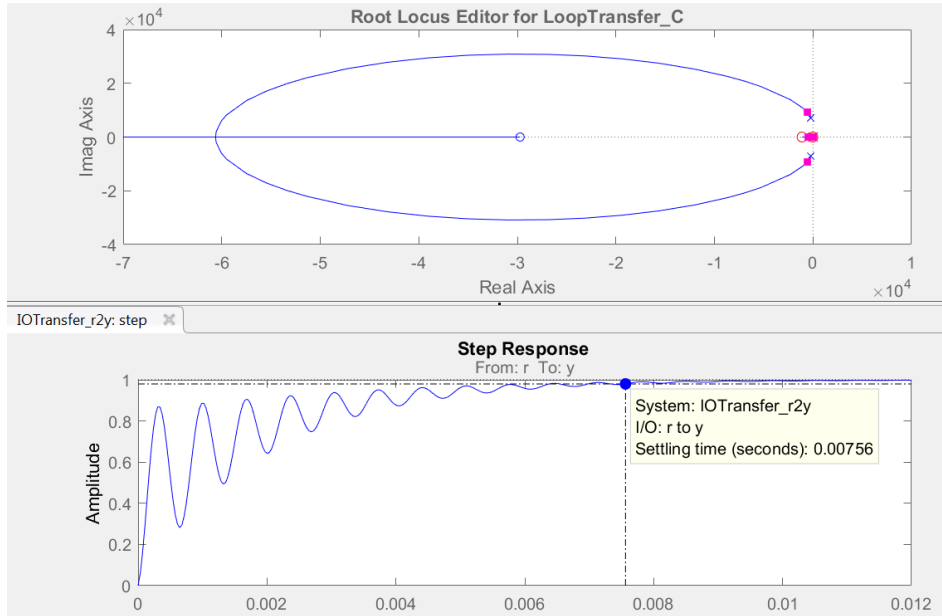| Controller Gains	C_{PID_lcc}
K_{P_lcc}	-0.00132
K_{I_lcc}	-1.85
K_{D_lcc}	-0.001
τ_{D_lcc}	10

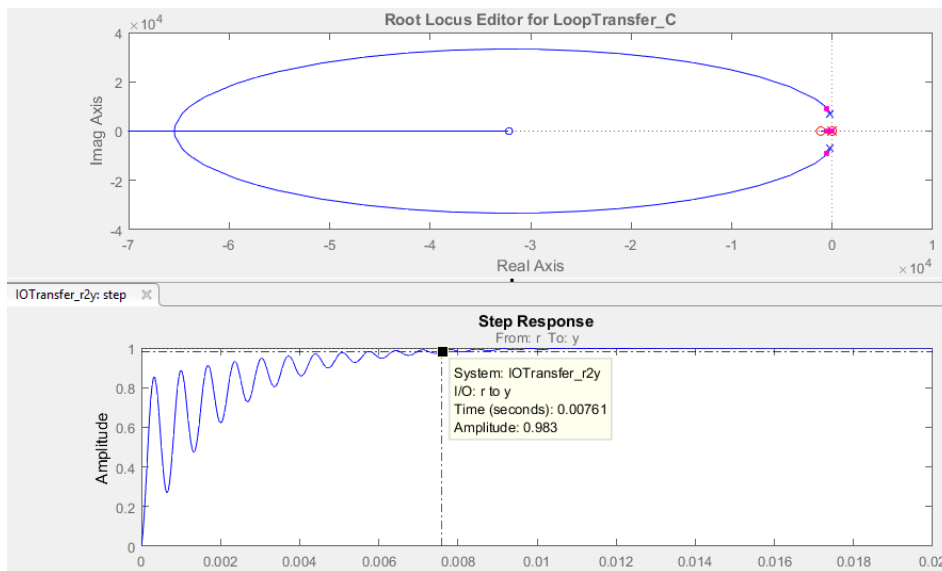Figure 21. Root locus and step response to closed-loop SS system with PID controller

Figure 22. Root locus and step response to closed-loop double-sided LCC system with PID controller

Similarly, this controller meets the requirements. It is an stable response that has a settling time of 0.00761 seconds and there is no overshoot.

4. Results

The DWPTS has been simulated in MATLAB/Simulink with the model shown in Figure 23. RMS blocks are used in simulation models to eliminate noise from measurements. Switches of the inverter are simulated with an IGBT block, which includes a losses model.
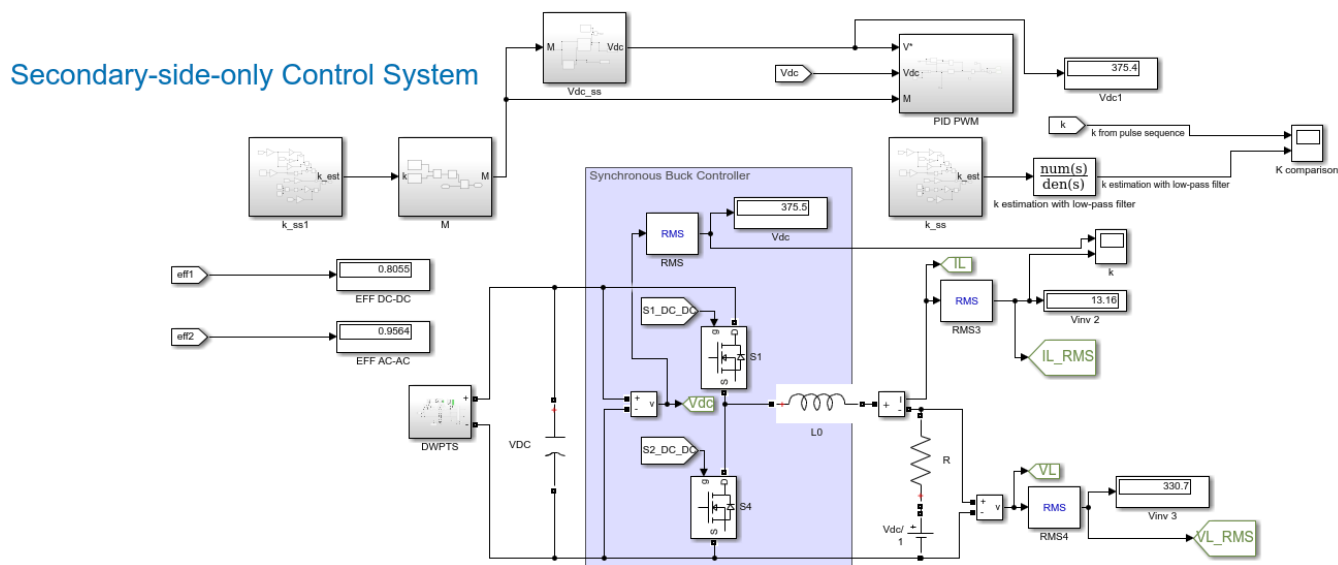

Figure 23. Secondary-side-only control system model Simulink

Figure 24 shows models of DWPTS adopting both compensation topologies as studied in this project. A dependent voltage source block has been used instead of a mutual inductance block. This was done to vary the coupling coefficient during simulation according to the assumed pattern. The settling time of the simulated systems, both SS and double-sided LCC, is 0.002s. The SS compensated system response is overshot by 10%. Similarly, the double-sided LCC compensated system is also overshot, however this is smaller, 5%.

The response of the systems to the proposed dynamic scenario is shown in Figure 25. Both controllers followed the reference for optimal efficiency while the coupling coefficient is changing. Note that in Figure 25 (a), the SS system performs at an overall AC-AC efficiency of 96.77%, which is measured from the output of the inverter to the input of the rectifier. The difference between these two efficiencies is the power losses of the DC- AC conversion and AC-DC conversion stages. There are 7.77% power losses in the inverter, rectifier and buck converter. In addition, its overall DC-DC Efficiency, measured from the DC source to the battery, is 89%. The SS system delivers an average DC power of 3.8 kW. One can observe that the DC link voltage is following the reference with a small ripple of 2 V amplitude.
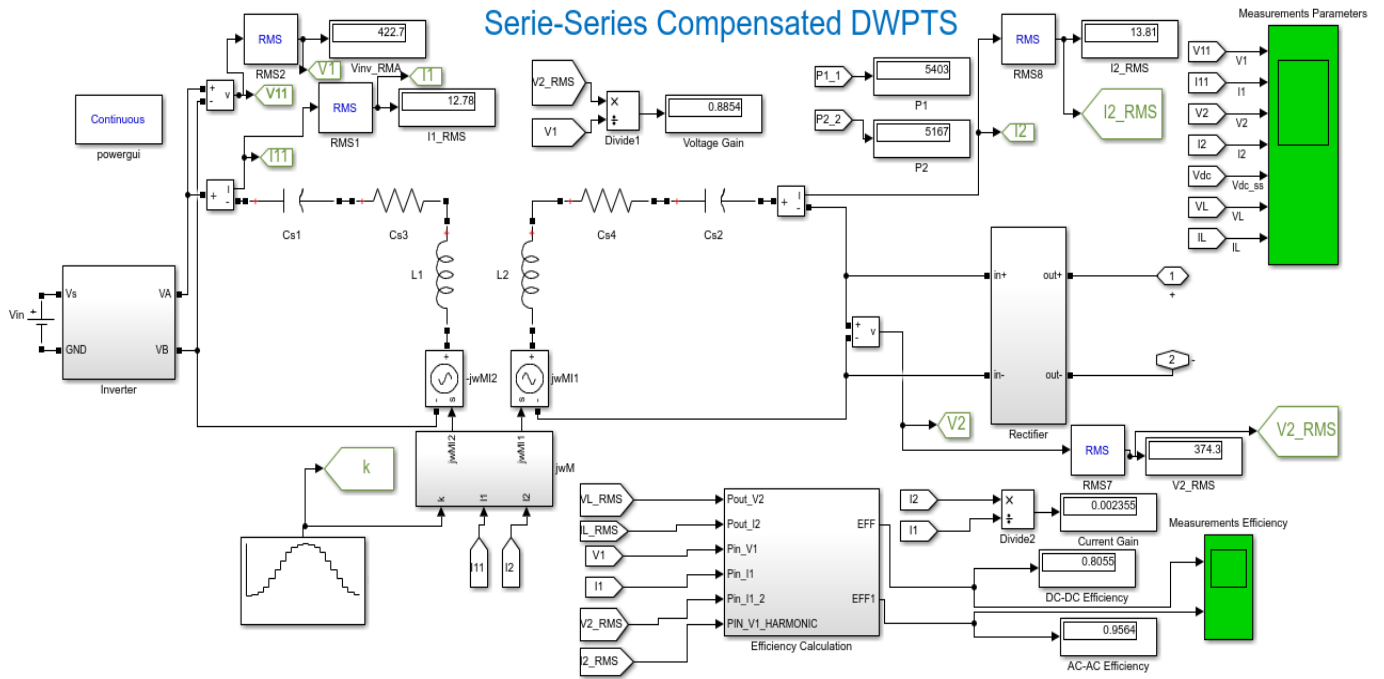
(a)
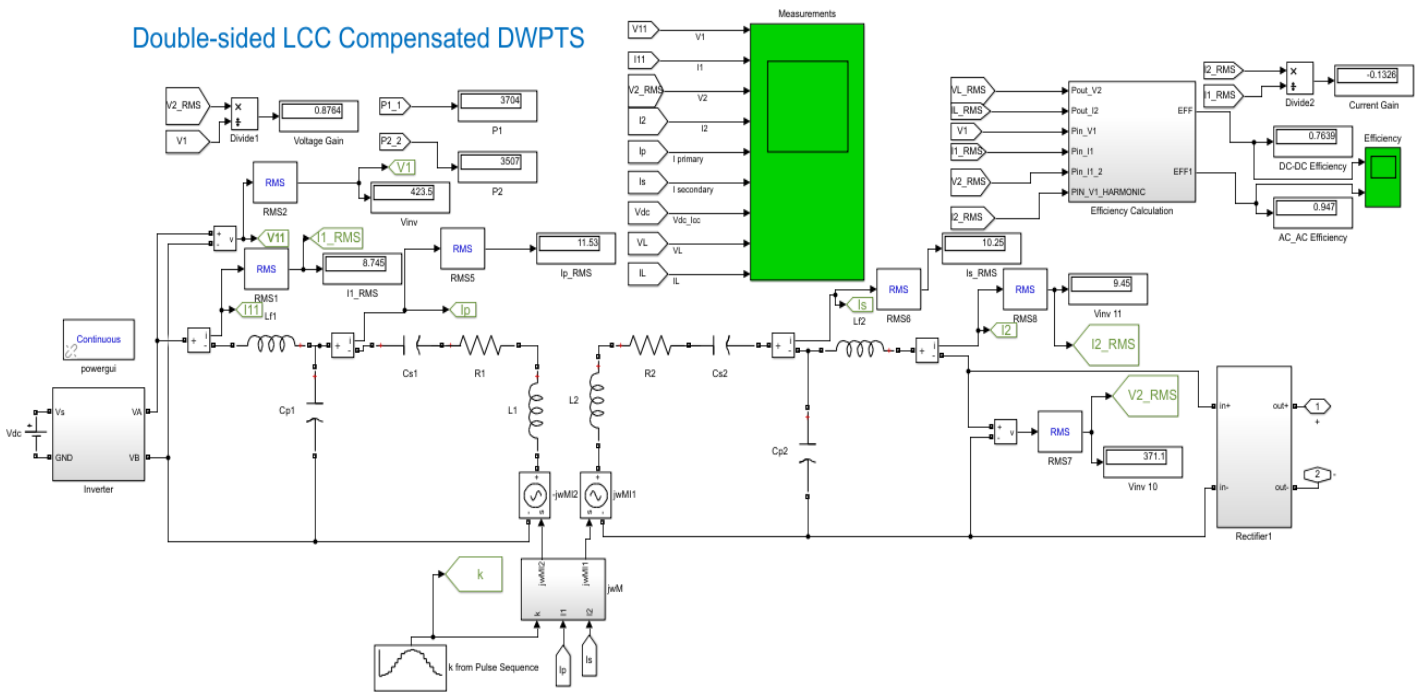
(b)

Figure 24. (a) Series-Series compensated model for DWPTS subsystem (b) Doubled-sided LCC compensated model for DWPTS subsystem

On the other hand in Figure 25 (b), overall AC-AC efficiency in the double-sided LCC system is 95.41% while its DC-DC efficiency is 85.72 % delivering 3.35 kW. It means that the percentage of power losses is 9.69% in the inverter, rectifier and buck converter. Likewise, the DC link voltage tracks the reference with a ripple of 1.8 V amplitude. It is similar to the series-series system. In Figure 26, the estimation of the coupling coefficient is illustrated for different EV's speed. Figure 26 (a) and (b) show k estimated and k real for an EV passing across the transmitter track at a speed of 28.8 km/h and 115 km/h for a series-series system.
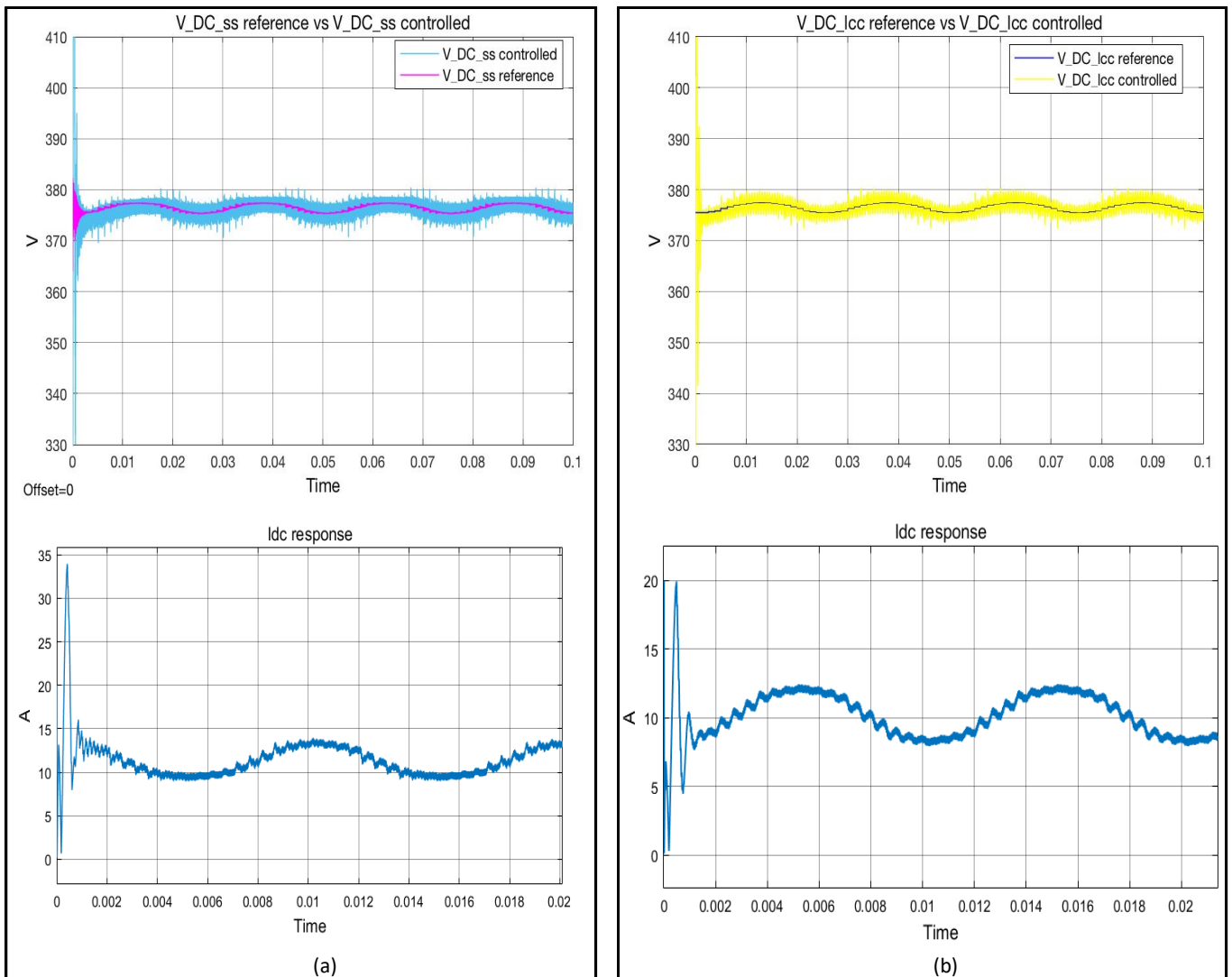

Figure 25. (a) DC voltage response compared with the voltage reference and current response to dynamic coupling coefficient pattern of SS control system at Tp=0.025 seconds (b) DC voltage response compared with the voltage reference and current response to dynamic coupling coefficient pattern of double-sided LCC system Tp=0.025 seconds
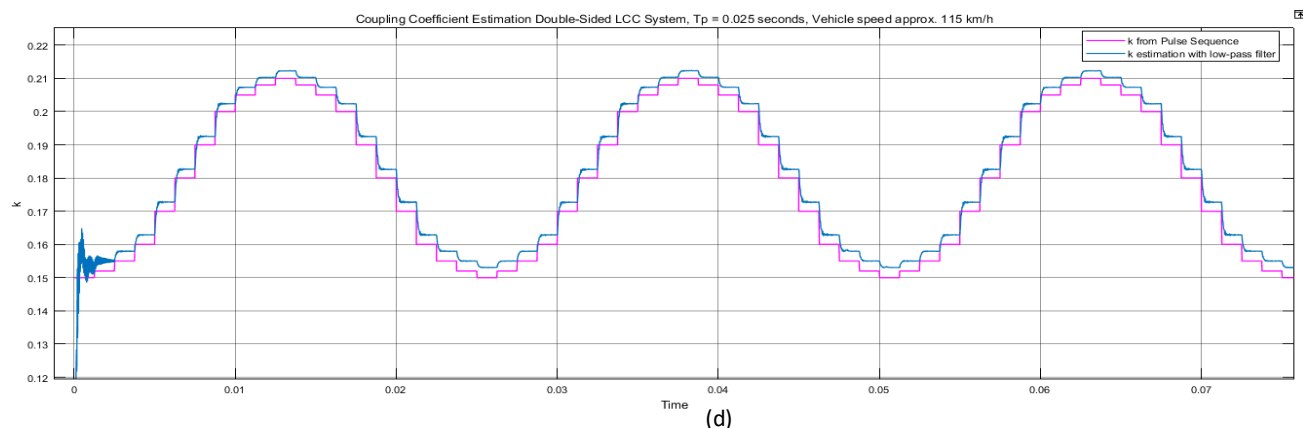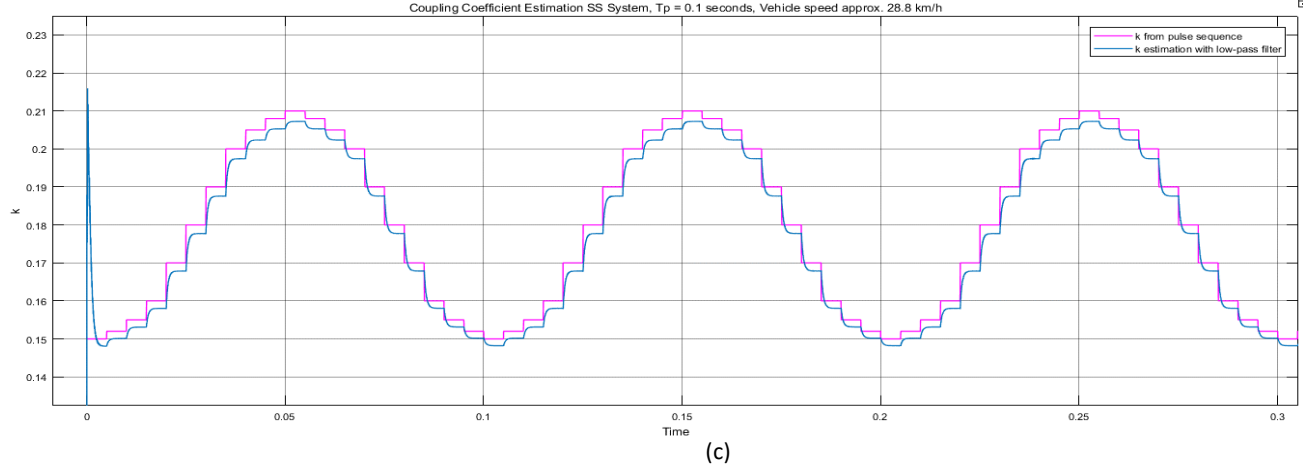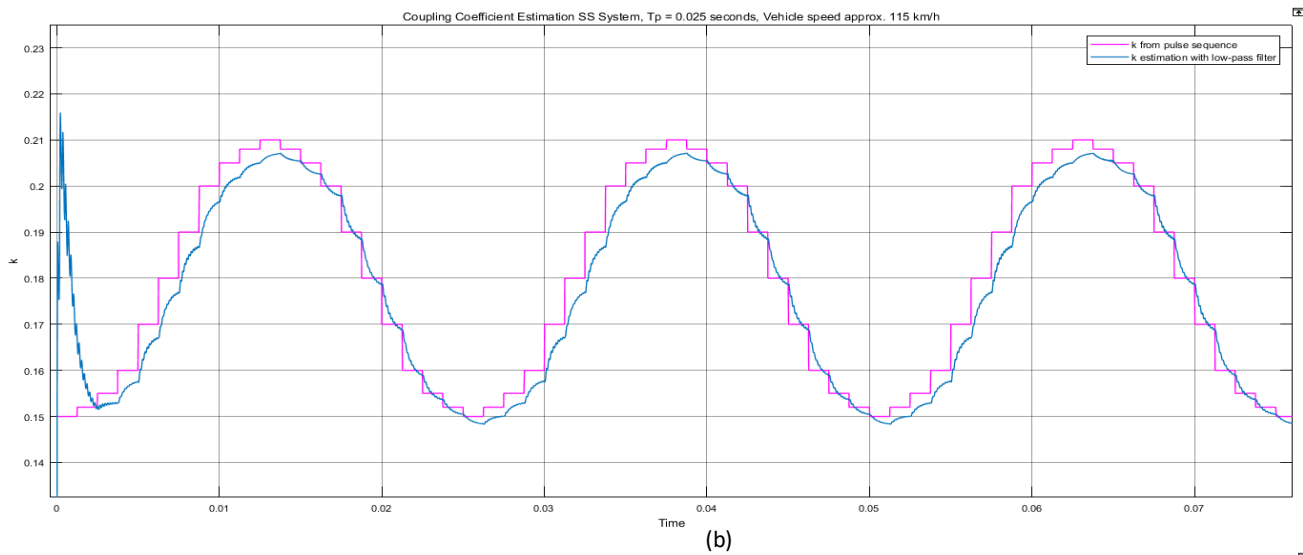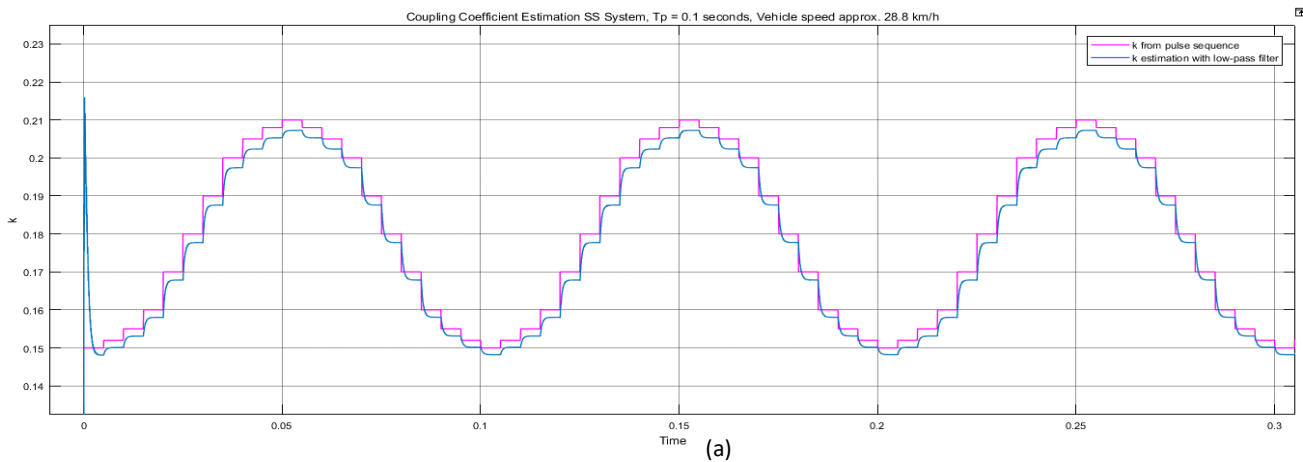
Figure 26. Coupling coefficient estimations (a) SS system at Tp = 0.1 seconds (b) SS system at Tp = 0.025 seconds (c) Double-sided LCC system at Tp= 0 seconds (d) Double-sided LCC system at Tp = 0.025 seconds

63

Moreover, this matching is illustrated for a double-sided system under the same conditions in Figure 26 (c) and (d). Root-mean-square deviation (RMSD) is used to compare the estimation and the real value of coupling coefficient.

$$RMSD = \sqrt{\frac{\sum_{i=1}^{n}\left(k_{est_i} - k_i\right)^2}{n}} \tag{4.01}$$

The RMSD values of the relation described by equation (4.01) for data from Figure 26 (a)-(d) are 0.0028, 0.0039, 0.003 and 0.0031, respectively. In terms of RMSD, one can state that the estimation methods presented in equations (3.4) and (3.8) are accurate due to the small deviation of k estimated, compared to its real value.

In Figure 27, voltage stress of the circuit components in both compensations topologies is shown for the assumed coupling coefficient variation pattern. It can be observed that voltage stress of the coils in double-sided LCC CT is lower than the SS CT. Primary coil and secondary coil peak voltages reduce from 3.74 kV and 3.95 kV to 3 kV and 2.65 kV, respectively. In a similar way, compensation elements have lower voltage stress in the double-sided LCC compensated system than the SS compensated system. Primary series capacitor peak voltage drops from 3.32 kV to 2.4 kV while secondary series capacitor peak voltage decreases from 3.58 kV to 2.15 kV. Additional elements such as series inductor and parallel capacitor have a voltage stress less than one kilovolt at both transmitter and receiver sides. The higher voltage at the beginning of the simulation is due to the simulation model. Remember that the dependent voltage source blocks have been selected to simulated the mutual inductance voltage for the varying coupling coefficient. This voltage dependent source on the transmitter depends on the current of the receiver. In the same way, the voltage dependent source on the receiver depends on the transmitter current. Hence, when the simulations stars, there is an error during the initialization of the sources that disappears when the measurements of the respective currents is accurate. Moreover, a series-series system has the disadvantage that the transmission voltage varies with the coupling coefficient. Low coupling coefficients results in high voltage stress. Thus, the secondary-side control does not guaranty safe performance conditions and the control of the transmitter. Furthermore, from Figure 27 (b), one can notice how voltage stress remains constant in the transmitter and receiver coil elements of the double-sided LCC system. L_1, L_2, C_{s1} and C_{s2} voltages keep constant regardless coupling variations which is the advantage of the

double-sided LCC CT in terms of controllability of the transmitter. Desired voltage of transmission can be selected since the design stage adding simplicity to the control system.
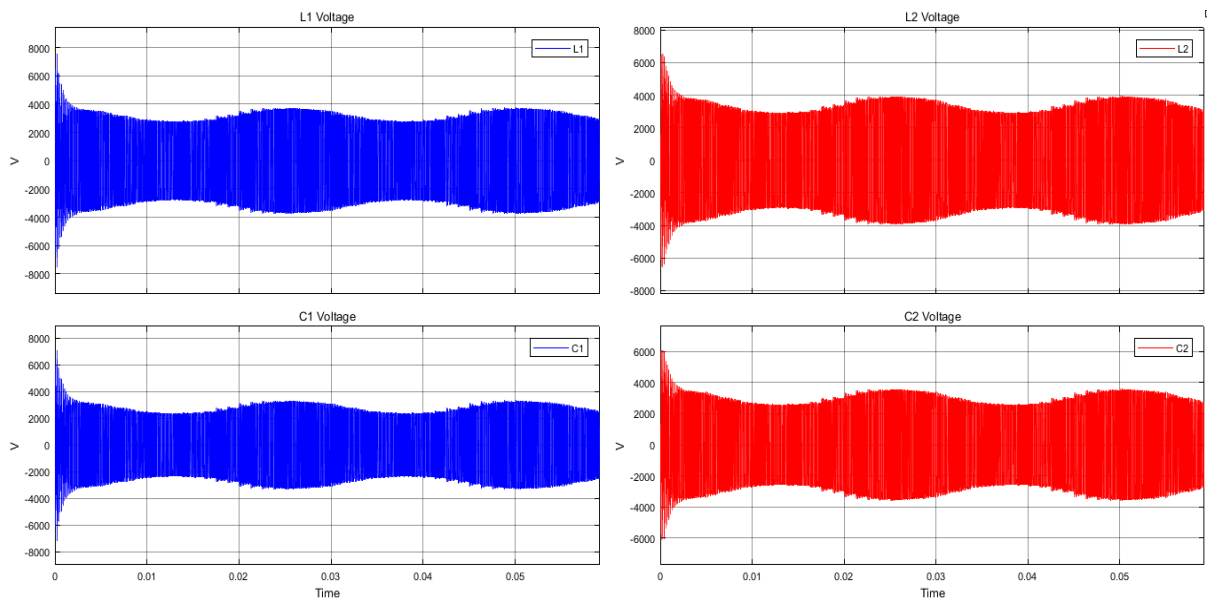
(a)
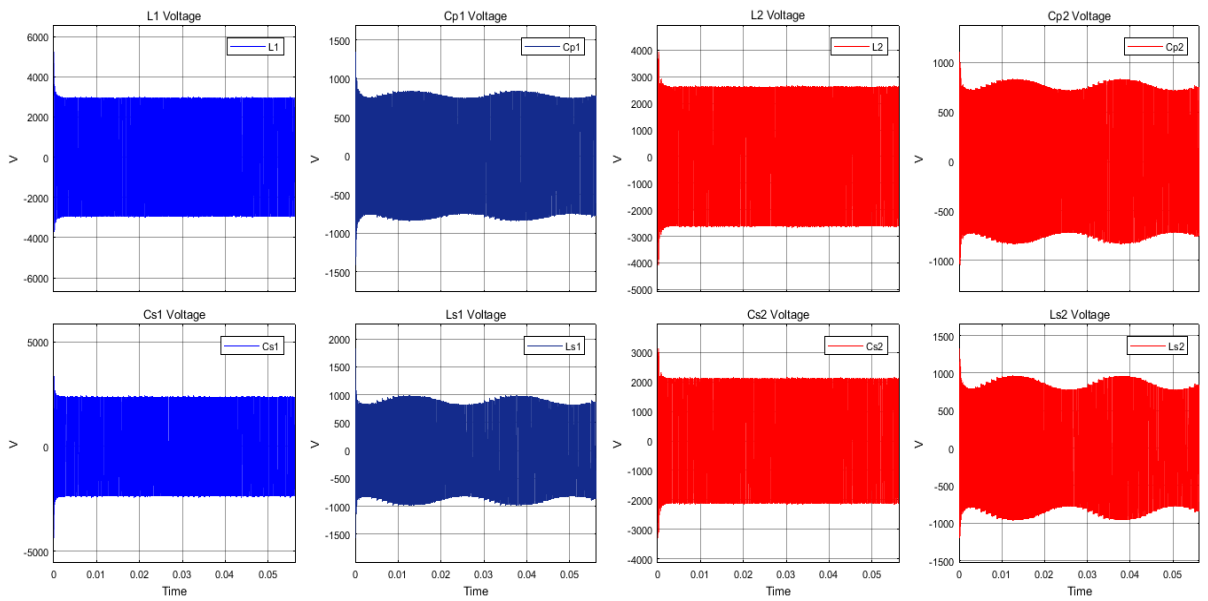
(b)

Figure 27.Voltage stress in circuit elements (a) Series-series CT elements (b) Double-sided LCC CT elements

5. Conclusion and Future Work

5.1. Conclusion

A comparison study of series-series and double-sided LCC compensation topology for a dynamic wireless power transfer system has been carried out in this thesis. A secondary-side-only control method was selected among those discussed in the literature review. The target in this control scheme was to control the reflected load from the inverter by modifying the duty cycle of the controller and regulating the DC link voltage. Moreover, no communication system was required due to the estimation of coupling coefficient with parameters from the receiver side. This methodology has been chosen because it reduces the cost by reducing the elements of the system, simplifying the transmitter side. An equation for the estimation of coupling coefficient and a controller model for the double-sided LCC compensated dynamic wireless system have been proposed in this report. It was assumed that a coupling coefficient variation pattern of same size pads and no switching losses occurs when the transmitter tracks were turned on and off. Double-sided LCC CT shows a better performance regarding elements voltage stress. In addition, transmitter and receiver currents keeps constant regardless coupling coefficient variation, which represents a great advantage for control purposes. Simulation results indicate an accurate estimation of coupling coefficient for both topologies. Moreover, results indicate that the design requirements have been successfully achieved. The output voltage followed the reference with no steady state error and rise time of 0.002s. Overall DC-DC efficiency of the SS system was 89% while the double-sided LCC compensated system was 87%, and the averaged power delivered was 3.8 kW and 3.5 kW, respectively. The target of this study was to accomplish MPTE conditions rather than maximum power transference. In conclusion, the control strategy is validated for both systems due to the fact that efficiency targets were achieved. However, double-sided LCC compensation topology adoption showed a better performance in terms of voltage stress and transmitter controllability.

5.2. Future Work

Future work based on this project is to design and implement a prototype. The first step is to design a transmitter and receiver pads. Second, to simulate the double-sided LCC compensated system with commercial elements for later implementation. This will not only take the battery into consideration, but also the electric vehicle with all its components as the load. In addition, a proper analysis of costs of deployment of the system per kilometre is needed to examine

feasibility. Finally, the building of a prototype implemented with a secondary-side-only controller is planned.

6. References

[1]   (2013). *Cars and Carbon Dioxide*. Available: http://www.dft.gov.uk/vca/fcb/cars-and-carbon-dioxide.asp

[2]   (2015). *Informe de la Situacion del Medio Ambiente en Mexico*. Available: https://www.gob.mx/cms/uploads/attachment/file/161446/Cap_CC_completo.pdf

[3]   K. B. Naceur and J. F. Gagne, "Global EV Outlook 2017," International Energy Agency.

[4]   S. Y. Choi, B. W. Gu, S. Y. Jeong and C. T. Rim, "Advances in Wireless Power Transfer Systems for Roadway-Powered Electric Vehicles", *IEEE Journal of Emerging and Selected Topics in Power Electronics,* vol. 3, no. 1, pp. 18-36, 2015.

[5]   F. Lu, H. Zhang, H. Hofmann, and C. C. Mi, "A Dynamic Charging System With Reduced Output Power Pulsation for Electric Vehicles", *IEEE Transactions on Industrial Electronics,* vol. 63, no. 10, pp. 6580-6590, 2016.

[6]   R. Bosshard and J. W. Kolar, "Inductive power transfer for electric vehicle charging: Technical challenges and tradeoffs", *IEEE Power Electronics Magazine,* vol. 3, no. 3, pp. 22-30, 2016.

[7]   Z. Bi, T. Kan, C. C. Mi, Y. Zhang, Z. Zhao, and G. A. Keoleian, "A review of wireless power transfer for electric vehicles: Prospects to enhance sustainable mobility", *Applied Energy,* vol. 179, pp. 413-425, 2016.

[8]   J. I. Agbinya, *Wireless Power Transfer* (River Publishers Series in Communications). The Netherlands: River Publishers, p. 708, 2016.

[9]   N. Tesla, "System of Electric Lighting", United States of America, 1891.

[10]   M. Cheney, *Tesla: Master of Lightning*. MetroBooks, 2001.

[11]   M. H. Leblanc, M., "Transformer System for Electric Railways", United States of America, 1894.

[12]   G. A. Covic and J. T. Boys, "Inductive Power Transfer", *Proceedings of the IEEE,* vol. 101, no. 6, pp. 1276-1289, 2013.

[13]   S. Li and C. C. Mi, "Wireless Power Transfer for Electric Vehicle Applications", *IEEE Journal of Emerging and Selected Topics in Power Electronics,* vol. 3, no. 1, pp. 4-17, 2015.

[14]   J. Huh, S. W. Lee, W. Y. Lee, G. H. Cho and C. T. Rim, "Narrow-Width Inductive Power Transfer System for Online Electrical Vehicles", *IEEE Transactions on Power Electronics,* vol. 26, no. 12, pp. 3666-3679, 2011.

[15]   J. T. Boys, C. Y. Huang and G. A. Covic, "Single-phase unity power-factor inductive power transfer system", *IEEE Power Electronics Specialists Conference*, pp. 3701-3706, 2008.

[16]   M. Budhia, G. A. Covic, and J. T. Boys, "Design and Optimization of Circular Magnetic Structures for Lumped Inductive Power Transfer Systems", *IEEE Transactions on Power Electronics,* vol. 26, no. 11, pp. 3096-3108, 2011.

[17]   L. Chen, G. R. Nagendra, J. T. Boys and G. A. Covic, "Double-Coupled Systems for IPT Roadway Applications", *IEEE Journal of Emerging and Selected Topics in Power Electronics,* vol. 3, no. 1, pp. 37-49, 2015.

[18] W. Chwei-Sen, O. H. Stielau and G. A. Covic, "Design considerations for a contactless electric vehicle battery charger", *IEEE Transactions on Industrial Electronics,* vol. 52, no. 5, pp. 1308-1314, 2005.

[19] G. A. Covic, J. T. Boys, M. L. G. Kissin and H. G. Lu, "A Three-Phase Inductive Power Transfer System for Roadway-Powered Vehicles", *IEEE Transactions on Industrial Electronics,* vol. 54, no. 6, pp. 3370-3378, 2007.

[20] A. Kamineni, G. A. Covic and J. T. Boys, "Analysis of Coplanar Intermediate Coil Structures in Inductive Power Transfer Systems", *IEEE Transactions on Power Electronics,* vol. 30, no. 11, pp. 6141-6154, 2015.

[21] N. A. Keeling, G. A. Covic and J. T. Boys, "A Unity-Power-Factor IPT Pickup for High-Power Applications", *IEEE Transactions on Industrial Electronics,* vol. 57, no. 2, pp. 744-751, 2010.

[22] M. Budhia, J. T. Boys, G. A. Covic and C. Y. Huang, "Development of a Single-Sided Flux Magnetic Coupler for Electric Vehicle IPT Charging Systems", *IEEE Transactions on Industrial Electronics,* vol. 60, no. 1, pp. 318-328, 2013.

[23] G. A. Covic, J. T. Boys, A. M. W. Tam and J. C. H. Peng, "Self tuning pick-ups for inductive power transfer", *IEEE Power Electronics Specialists Conference*, pp. 3489-3494, 2008.

[24] C. Y. Huang, J. T. Boys, G. A. Covic and M. Budhia, "Practical considerations for designing IPT system for EV battery charging", *IEEE Vehicle Power and Propulsion Conference*, pp. 402-407, 2009.

[25] J. T. Boys, G. A. Covic and A. W. Green, "Stability and control of inductively coupled power transfer systems", *IEEE Proceedings - Electric Power Applications,* vol. 147, no. 1, pp. 37-43, 2000.

[26] A. Zaheer, M. Neath, H. Z. Z. Beh and G. A. Covic, "A Dynamic EV Charging System for Slow Moving Traffic Applications", *IEEE Transactions on Transportation Electrification,* vol. 3, no. 2, p. 354-369, 2017.

[27] I. S. Suh and J. Kim, "Electric vehicle on-road dynamic charging system with wireless power transfer technology", *International Electric Machines & Drives Conference*, pp. 234-240, 2013.

[28] C. C. Mi, G. Buja, S. Y. Choi and C. T. Rim, "Modern Advances in Wireless Power Transfer Systems for Roadway Powered Electric Vehicles", *IEEE Transactions on Industrial Electronics,* vol. 63, no. 10, pp. 6533-6545, 2016.

[29] *SAET TIR J2954.*

[30] L. Summerer and O. Purcell, "Concepts for wireless energy transmission via laser", *Europeans Space Agency-Advanced Concepts Team,* 2009.

[31] P. Ning, J. M. Miller, O. C. Onar and C. P. White, "A compact wireless charging system for electric vehicles", *IEEE Energy Conversion Congress and Exposition*, pp. 3629-3634, 2013.

[32] H. H. Wu, A. Gilchrist, K. D. Sealy and D. Bronson, "A High Efficiency 5 kW Inductive Charger for EVs Using Dual Side Control", *IEEE Transactions on Industrial Informatics,* vol. 8, no. 3, pp. 585-595, 2012.

[33] F. Lu, H. Zhang, H. Hofmann and C. Mi, "A high efficiency 3.3 kW loosely-coupled wireless power transfer system without magnetic material", *IEEE Energy Conversion Congress and Exposition*, pp. 2282-2286, 2015.

[34] W. Li, H. Zhao, S. Li, J. Deng, T. Kan and C. C. Mi, "Integrated LCC Compensation Topology for Wireless Charger in Electric and Plug-in Electric Vehicles", *IEEE Transactions on Industrial Electronics,* vol. 62, no. 7, pp. 4215-4225, 2015.

[35] T. D. Nguyen, S. Li, W. Li and C. C. Mi, "Feasibility study on bipolar pads for efficient wireless power chargers", *IEEE Applied Power Electronics Conference and Exposition*, pp. 1676-1682, 2014.

[36] R. Bosshard, J. W. Kolar, J. Mühlethaler, I. Stevanović, B. Wunsch and F. Canales, "Modeling and n-alpha-Pareto Optimization of Inductive Power Transfer Coils for Electric Vehicles", *IEEE Journal of Emerging and Selected Topics in Power Electronics,* vol. 3, no. 1, pp. 50-64, 2015.

[37] K. Throngnumchai, T. Kai, and Y. Minagawa, "A study on receiver circuit topology of a cordless battery charger for electric vehicles", *IEEE Energy Conversion Congress and Exposition*, pp. 843-850, 2011.

[38] K. Throngnumchai, A. Hanamura, Y. Naruse and K. Takeda, "Design and evaluation of a wireless power transfer system with road embedded transmitter coils for dynamic charging of electric vehicles", *World Electric Vehicle Symposium and Exhibition*, pp. 1-10, 2013.

[39] J. A. Russer, M. Dionigi, M. Mongiardo, F. Mastri, A. Costanzo and P. Russer, "A system for dynamic inductive power supply of electric vehicles on the road", *IEEE Wireless Power Transfer Conference*, pp. 1-4, 2014.

[40] J. Shin, S. Shin, Y. Kim, S. Ahn, S. Lee, G. Jung, S. Jeon and D. Cho, "Design and Implementation of Shaped Magnetic-Resonance-Based Wireless Power Transfer System for Roadway-Powered Moving Electric Vehicles", *IEEE Transactions on Industrial Electronics,* vol. 61, no. 3, pp. 1179-1192, 2014.

[41] V. X. Thai, S. Y. Choi, B. H. Choi, J. H. Kim and C. T. Rim, "Coreless power supply rails compatible with both stationary and dynamic charging of electric vehicles", *IEEE 2nd International Future Energy Electronics Conference*, pp. 1-5, 2015.

[42] S.-H. Lee, J.-H. Kim and J.-H. Lee, "Development of a 60 kHz, 180 kW, Over 85% Efficiency Inductive Power Transfer System for a Tram," *Energies,* vol. 9, no. 12, p. 1075, 2016.

[43] O. C. Onar, J. M. Miller, S. L. Campbell, C. Coomer, C. P. White and L. E. Seiber, "A novel wireless power transfer for in-motion EV/PHEV charging", *IEEE Applied Power Electronics Conference and Exposition*, pp. 3073-3080, 2013.

[44] K. Lee, Z. Pantic and S. M. Lukic, "Reflexive Field Containment in Dynamic Inductive Power Transfer Systems," *IEEE Transactions on Power Electronics,* vol. 29, no. 9, pp. 4592-4602, 2014.

[45] U. D. o. Energy, "Mitsubishi i-MiEV Advanced Vehicle Testing – Baseline Testing Results", in "Vehicle Technologies Program", Energy Efficiency & Renewable Energy, 2012.

[46] H. Sakamoto, K. Harada, S. Washimiya, K. Takehara, Y. Matsuo and F. Nakao, "Large air-gap coupler for inductive charger [for electric vehicles]", *IEEE Transactions on Magnetics,* vol. 35, no. 5, pp. 3526-3528, 1999.

[47] T. V. Theodoropoulos, I. G. Damousis and A. J. Amditis, "Demand-Side Management ICT for Dynamic Wireless EV Charging", *IEEE Transactions on Industrial Electronics,* vol. 63, no. 10, pp. 6623-6630, 2016.

[48] J. Deng, L. Fei, S. Li, T. D. Nguyen and C. Mi, "Development of a high efficiency primary side controlled 7kW wireless power charger", *IEEE International Electric Vehicle Conference*, pp. 1-6, 2014.

[49] *Guidelines for Limiting Exposure to Time-Varying Electric, Magnetic, and Electromagnetic Fields,* I. C. o. N.-I. R. P. (ICNIRP), 1998.

[50] S. Li, W. Li, J. Deng, T. D. Nguyen and C. C. Mi, "A Double-Sided LCC Compensation Network and Its Tuning Method for Wireless Power Transfer", *IEEE Transactions on Vehicular Technology,* vol. 64, no. 6, pp. 2261-2273, 2015.

[51] M. H. Rashid, N. Kumar, and A. R. Kul*karni, Power electronics: devices, circuits, and applications. Boston: Pearson, 2014.*

[52] K. Yamaguchi, T. Hirata and I. Hodaka, "Using Square Wave Input for Wireless Power Transfer", *International Journal of Electrical and Computer Engineering,* vol. 6, no. 1, pp. 431-438, 2016.

[53] S. Y. Choi, S. Y. Jeong, B. W. Gu, G. C. Lim and C. T. Rim, "Ultraslim S-Type Power Supply Rails for Roadway-Powered Electric Vehicles", *IEEE Transactions on Power Electronics,* vol. 30, no. 11, pp. 6456-6468, 2015.

[54] Z. Li, C. Zhu, J. Jiang, K. Song and G. Wei, "A 3-kW Wireless Power Transfer System for Sightseeing Car Supercapacitor Charge", *IEEE Transactions on Power Electronics,* vol. 32, no. 5, pp. 3301-3316, 2017.

[55] W. Zhang, S. C. Wong, C. K. Tse and Q. Chen, "Analysis and comparison of secondary series- and parallel-compensated IPT systems", *IEEE Energy Conversion Congress and Exposition*, pp. 2898-2903, 2013.

[56] K. Hata, T. Imura and Y. Hori, "Dynamic wireless power transfer system for electric vehicles to simplify ground facilities - power control and efficiency maximization on the secondary side", *IEEE Applied Power Electronics Conference and Exposition*, pp. 1731-1736, 2016.

[57] L. Peng, L. Xiao-kun, G. R. Zhu, M. Xie and X. S. L. a, "Characteristics Research on Double LCC Compensation Converter in the Inductive Energy Transfer System", *International Conference on Industrial Informatics - Computing Technology, Intelligent Technology, Industrial Information Integration*, pp. 243-246, 2015.

[58] N. Y. Kim, K. Y. Kim, J. Choi and C. W. Kim, "Adaptive frequency with power-level tracking system for efficient magnetic resonance wireless power transfer", *Electronics Letters,* vol. 48, no. 8, pp. 452-454, 2012.

[59] J. M. Miller, O. C. Onar and M. Chinthavali, "Primary-Side Power Flow Control of Wireless Power Transfer for Electric Vehicle Charging", *IEEE Journal of Emerging and Selected Topics in Power Electronics,* vol. 3, no. 1, pp. 147-162, 2015.

[60] Z. Popovic and B. D. Popovic, *Introductory Electromagnetics, Practice Problems and Labs.* Englewood Cliffs, NJ, USA: Prentice-Hall, 2000

[61] J. P. K. Sampath, D. M. Vilathgamuwa and A. Alphones, "Efficiency Enhancement for Dynamic Wireless Power Transfer System With Segmented Transmitter Array", *IEEE Transactions on Transportation Electrification,* vol. 2, no. 1, pp. 76-85, 2016.

[62] H. Li, J. Li, W. Chen and X. Yang, "A Maximum Energy Efficiency Tracking Control Scheme for Wireless Power Transfer Systems Using Magnetic Resonant Coupling", *IEEE Transactions on Power Electronics,* vol. 30, no. 7, pp. 3998-4008, 2015.

[63] R. Tavakoli, A. Jovicic, N. Chandrappa, R. Bohm and Z. Pantic, "Design of a dual-loop controller for in-motion wireless charging of an electric bus", *IEEE Energy Conversion Congress and Exposition*, pp. 1-8, 2016.

[64] A. Triviño-Cabrera, M. Ochoa, D. Fernández and J. A. Aguado, "Independent primary-side controller applied to wireless chargers for electric vehicles", *IEEE International Electric Vehicle Conference*, pp. 1-5, 2014.

[65] D. Kobayashi, T. Imura and Y. Hori, "Real-time coupling coefficient estimation and maximum efficiency control on dynamic wireless power transfer for electric vehicles", *IEEE PELS Workshop on Emerging Technologies: Wireless Power*, pp. 1-6, 2015.

[66] D. Patil et al., "Maximum Efficiency Tracking in Wireless Power Transfer for Battery Charger: Phase Shift and Frequency Control", 2016.

[67] N. S. Nise, *Control Systems Engineering*. Hoboken: Wiley, 2011.